



**Scuola Internazionale Superiore  
di Studi Avanzati**

# Bridging Spinal networks: Novel 3D substrates as neural implantable interfaces

Thesis submitted for the degree of "*Doctor of Philosophy*"

*Candidate:*

Sadaf Usmani

*Supervisor:*

Prof. Laura Ballerini

SISSA – Via Bonomea, 265 – 34136 Trieste (Italy)

# Contents

---

<b>Aims.....</b>	<b>1</b>
<b>Introduction.....</b>	<b>2</b>
<b>1. Tissue engineering and role of nanotechnology in central nervous system (CNS) injury.....</b>	<b>2</b>
1.1 Tissue engineering and challenges: CNS injury	
1.2 Novel Strategies for CNS injury repair	
1.3 Where tissue engineering meets nanotechnology	
<b>2. Biomaterials: Design and strategies .....</b>	<b>10</b>
2.1 Biodegradation of the material	
2.2 Electrically active materials	
2.3 Mechanical cues	
2.4 Cell adhesion	
2.5 Internal matrices	
2.6 Three-dimensionality of biomaterials	
<b>3. Use of carbon nanotubes (CNTs) as scaffolds for neural regrowth.....</b>	<b>16</b>
3.1 3D pure CNT sponges	
3.2 PDMS and its functionalization with CNTs	
<b>4. Functional neurological impairment following spinal cord injury.....</b>	<b>28</b>
<b>5. Mechanisms of spontaneous recovery.....</b>	<b>33</b>
<b>6. Organotypic spinal cultures in material screening .....</b>	<b>34</b>
6 .1 Mouse embryonic spinal cord slice development	
<b>7. Tools for assessing spinal cord injury and repair.....</b>	<b>37</b>

**Material and Methods**

**Results.....**

Paper 1. 3D meshes of carbon nanotubes guide functional reconnection of segregated spinal explants

Paper 2. Nanostructures to Engineer 3D Neural-Interfaces: Directing Axonal Navigation towards Successful Bridging of Spinal Segments

Paper 3. 3D meshes of carbon nanotubes mediate functional recovery in spinal cord injured rats (*MS in preparation*)

**Discussion.....96**

**References.....105**

# Aims of the study

---

The main aim of my thesis was to test the ability of three-dimensional carbon based materials in directing re-growing axons towards a functional electrical reconnection between segregated spinal explants *in vitro*. Our goal was also to investigate biocompatibility of these materials *in vivo* and to understand the extent of functional recovery attributed to the implanted material into CNS milieu.

Hence the primary focus of the thesis was to interface 3D carbon based materials to organotypic spinal explants *in vitro* and

1. To investigate neurite web morphology and regrowth of fibers exiting from spinal cord explants
2. Electrophysiological characterization of motor outputs by performing simultaneous local field potential recordings from the ventral horns
3. To compare the effect of pure 3D freestanding multiwalled carbon nanotubes (3D CNF) with 2D carbon nanotubes, and 3D porous PDMS substrates with and without carbon nanotubes.
4. Tissue reaction and gliotic scar quantification upon implantation into adult rat brain cortex *in vivo*
5. To address if the implant represents a neuron-permissive environment

We also explored tissue reaction and functional sensory-motor recovery in spinal cord injury model; L1-hemisection-lesioned animals were implanted with 3D CNF *in vivo*. Our goals were:

1. To look for functional locomotor changes in behavior post-implantation
2. Tissue reaction and gliotic scar quantification
3. Whether the implanted material is creating neuron-permissive environment.

# Introduction

---

## 1. **Tissue engineering and role of nanotechnology in Central Nervous System (CNS) injury**

### *1.1. Tissue engineering and challenges: CNS injury*

Tissue engineering and regenerative medicine are emerging fields that share merging bioengineering with medicine. Both areas are based on integrative approaches that make use of genetic engineering, nanotechnologies and material science to carve ways to overcome limitations in tissue self-repair after damage, especially in case of Central Nervous System (CNS) injuries (Laube T et al, 2003). CNS injuries result in devastating and permanent losses of neurological functions due to its limited regenerative capacities that compromises spontaneous complete functional recovery. CNS lesions remain the leading cause of morbidity and mortality among the young population throughout the world and yet there are no effective therapies for treatment. Limited CNS self-repair is due to the inhibitory tissue environment which poses non permissible conditions for the regenerative axon re-growth (Wang M et al., 2011). In 1911, Tello, *et al.*, demonstrated that recovery and regrowth of CNS neurons can take place, if provided with a permissive environment. By serving a suitable environmental condition for rehabilitation of growth, functional recovery post CNS injuries can be facilitated, guided or promoted (David S and Aguayo AJ, 1981, Langer and Vacanti 1993).

The major challenge in engineering a suitable environment is addressing the severity and complexity of the central nervous system milieu after injury. Following a CNS trauma, a series of pathophysiological events occur like edema, ischemia, excitotoxicity and inflammation that can adversely affect the integrity of spared neurons and result in tissue damage even beyond the initial site of trauma (Brennan et el., 2012). Secondary damages followed by primary injury in CNS are a cascade of deleterious events that result in continued dysfunction and prolonged degeneration (Shoichet et al, book chapter, 2008).

CNS lacks the potential to readily regenerate unlike peripheral nervous system (PNS). PNS can upregulate Regeneration Associated Genes post injury and some of these genes have a direct role in neurite outgrowth and axon regeneration. Examples of such genes include c-Jun (Raivich et al. 2004), activating transcription factor-3 (ATF-3) (Seiffers et al. 2006), SRY-box containing gene 11 (Sox11), small proline-repeat protein 1A (SPRR1A) (Bonilla et al. 2002), growth-associated protein-43 (GAP-43) and CAP-23 (Bomze et al. 2001). In contrast to this, CNS do not upregulate RAGs to the same extent as the PNS. On top of that, numerous molecules were identified in CNS that limit regeneration. Myelin-associated inhibitors (MAIs) and the chondroitin sulfate proteoglycans (CSPGs) are the two major classes of CNS regeneration inhibitors that play a major role in limiting axon regeneration.

Pioneering work by Aguayo and colleagues demonstrated that some adult mammalian CNS neurons could retain the capacity to regenerate after injury, when provided with a permissive peripheral nerve graft (Aguayo, 1981). This confers that PNS environment is stimulatory while CNS environment is inhibitory. This study also demonstrates that adult mammalian neurons that do not regenerate normally are able to grow long distances into permissive environments and hence environment is a critical determinant of axon regeneration (Richardson et al. 1980, 1984; David and Aguayo, 1981; Benfey and Aguayo, 1982).

On the other hand, treatment strategies can fail due to inflammatory response of the tissue that follows the release of proinflammatory cytokines, migration of microglia and formation of a glial scar. Proinflammatory cytokines pose acutely harmful effects like Blood Brain Barrier (BBB) dysfunction, Blood Spinal Cord Barrier (BSCB) dysfunction and leukocyte infiltration, edema development and ultimately, promotion of neuronal death (Shoichet et al). Microglia, which are the first to respond (minutes to hours), proliferate, activate and migrate to the area of injury and along with astrocytes form a tight interpenetrating network known as reactive glial scar. Initially the glial response helps to buffer excitotoxicity and cytotoxicity, repair BBB or BSCB and isolate injury site, but if it persists at the injury site, it produces inhibitory factors that limit axonal regeneration and abort sprouting.

Thus, there is a dynamic interplay between events promoting repair and regeneration and those leading to damage and inhibition. Hence, to achieve a suitable approach towards CNS rehabilitation, it requires exploitation of multiple strategies to overcome or jump-start repair mechanisms of the CNS and get some level of functional recovery. By doing so, one can mimic native CNS conformation and provide most favorable environment for a functional neural repair (Langer and Vacanti 1993)

### *1.2. Novel Strategies for CNS injury repair*

Some basic developments towards understanding CNS injury and ways to stimulate repair can be achieved by delivering therapeutics to CNS, neuroregenerative approaches, or neuromodulation. This includes the use of neuroprotective agents, cell transplantation therapy, and/ or use of material scaffolds (conductive / non-conductive).

Neuroprotective agents or drugs, cell delivery and/or implantable biomaterials are some examples of possible efficacious cues to facilitate regain of function after damage (Tian et al., 2015). Neuroprotective agents work by controlling neuro-inflammation post trauma. Anti-inflammatory cytokines; interleukin-10, broadspectrum antibiotics like minocycline, sodium channel blockers such as riluzole, NMDA antagonists such as magnesium are such few examples. Pharmacological agents like corticosteroids (methylprednisolone in high doses), monosialotetrahexo-sylganglioside (GM-1; a naturally occurring compound in cell membranes of mammals and especially abundant in CNS membranes), thyrotropin-releasing hormone (TRH) and opiate antagonist (naloxone), have been clinically used or subjected to investigation for their neuroprotective roles. (Hawryluk et al. 2008, Gregorio et al., 2008, Hashimoto and Fukuda, 1991, Faden et al., 1981; Young et al., 1981).

Cell transplant approaches such as neural stem cells (NSCs), mesenchymal stem cells (MSCs), embryonic stem cells (ES), olfactory ensheathing cells (OECs), Schwann cells (SCs), activated macrophages and induced pluripotent stem cells (iPS) have succeeded in providing relevant pre-clinical data and are being extensively investigated due to their regenerative potential in CNS injuries. (Bottai et al., 2008, Hofstetter et al., 2005; Okada et al., 2005, Parr et al., 2008).

While use of neuroprotective agents and cell delivery are useful approaches for minimizing inhibitory environment and promoting growth, their use alone can be limited to

treating only a certain extent of damage. One way to improve the effect of such approaches and/ or to combine them is by the use of implantable materials as scaffolds (Figure1). In fact, the need of converging drugs and cellular therapy with material sciences is essential to observe strong beneficial outcomes in severe injury models (Silva et al., 2013). This can be achieved by incorporation of bioactive agents into the scaffold, cell seeding, delivering drugs etc. Not only does it facilitates bridging larger gaps at the site of injury but also provides localization of the therapeutic agent to site of the injury. Human bone marrow MSCs (hBM-MSCs) and endometrial stem cells (hEnSCs), when engineered on a suitable nanofiber scaffold were able to differentiate into motor neuron-like cells. (Shirian S et al., 2016).

Artificial scaffolds mimicking pro-regenerative extracellular matrix (ECM) might promote organization of neural processes resulting in a morphology that might favour neural regrowth. An exhaustive study on ECM engineering and its interactions with cells and various cues affecting cellular function are addressed in Dvir et al (Dvir et al, 2011). Functions of ECM include regulation of cellular functions like morphogenesis, proliferation, differentiation, migration, adhesion etc. Since the conformation of ECM is defined in nano-range; as nanocomposites, engineering ECM by means of nanotechnology and tissue engineering is an emerging field in controlling microenvironments served as cell supports. The importance of extracellular engineering of microenvironment can be better understood by involvement of ECM in regulating for instance topographical features, intracellular signalling cascades. It is believed that by mimicking dimensional scales of ECM, one can impart functional features of ECM to an engineered scaffold in order to enhance functional tissue organization. Nanostructures like gold nanowires, carbon nanotubes and nanofibers have shown to promote cell adhesion, tissue polarity, and adhesion and control growth factor deposition; which is yet another function of ECM. Reportedly, in recreation of ECM components, nanoscale tools, introduction of three-dimensionality in scaffolds and a correct choice of composition play essential roles (Dvir et al, 2011).



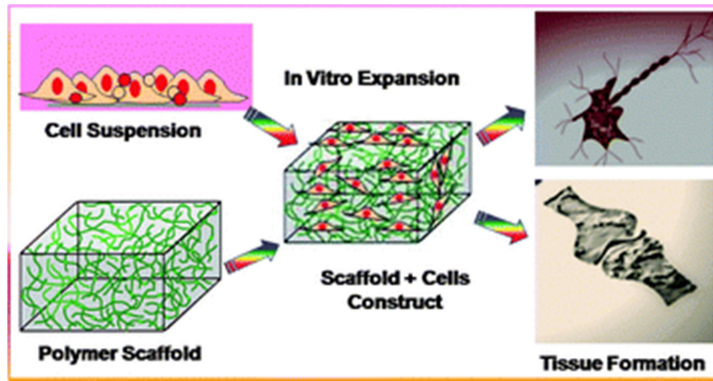


Figure1. Flow chart demonstrating scaffold use in seeding cells as an integrative approach for tissue construction. (Khan et al., 2015)

Additionally, a correct choice of scaffold (conductive materials) can be used for eliciting or recording electrical stimuli to CNS. Recording electrodes provide readouts of electrical activity to gain insight into the organization and functioning of the nervous system. By eliciting electrical stimulations, one can aid treatment of motor and sensory disabilities caused by neurological disorders (Patil AC and Thakor NV 2016).

Thus, a scaffold obtained by a controlled and yet sophisticated development with properties like conductivity, ease of tagging with cells and chemicals can prove to be a promising model to interface human nervous system and achieve higher levels of recovery.

### 1.3. *Where tissue engineering meets nanotechnology*

As discussed earlier, for a successful result, properties and characteristics of the biomaterial scaffold are crucial. Some of these properties include physical characteristics (e.g. porosity, geometry, dimension, mechanical strength), surface properties (e.g. chemical and topographical cues for cellular organization) and electrical conductance. These characteristics play a vital role in determining substrate's ability to adhere with cells, guide cell behavior (like migration, proliferation, differentiation, maintenance of phenotype and apoptosis), and, finally act as a mechanical support for tissue regeneration (Dietmar, 2000; Kneser et al., 2002; 1882 Silva et al., 2012c).

Tang QY and team in 2014 engineered micro or nanopatterns on the substrate surface and observed induced changes in directional persistence of cells. By doing so, one can actually control cell motility, migration and directionality (Tang QY et al., 2014).

On the other hand, topographical modifications of a substrate have also shown to improve adhesion, cellular invasion and signaling. Functionalization of the substrate with extracellular matrix components such as laminin has demonstrated increment of neurogenesis and astrogliosis decrement (Tavakol S. et al., 2016).

With time and better understanding of the nervous system, scientists have progressed from recognizing the organization of nervous system from centimeter range (keeping into account various lobes of the brain and spinal segments and their physiological functions) to even deeper understanding at the micrometer scale. Going further towards nanometer range, distinct sub-neuronal compartments and their interaction with surroundings at the molecular level can be investigated (Figure 2). By miniaturization of tools and prostheses, one can better probe and control extraordinary fidelity of biological systems and function at a fundamental level. (Alivisatos et al., 2013, Shreyas shah, 2016). Hence, by using devices and /or materials designed at a nanoscale, one can assure controlled integration of engineered material with the intact biological system. This is especially possible due to the extraordinary potential of nanoscale materials to be tailored precisely for a wide variety of applications (Rizzo LY et al, 2013). Nanomaterials can be tailored morphologically to closely resemble features of extracellular matrix components (ECM) in terms of porosity, biomechanical properties and biofunctionalities (Sarachino et al., 2013). Thus, by exploiting nano tool and technology revolutionary improvement in the quality of life after injury or disease can be made (Shreyas shah 2016).

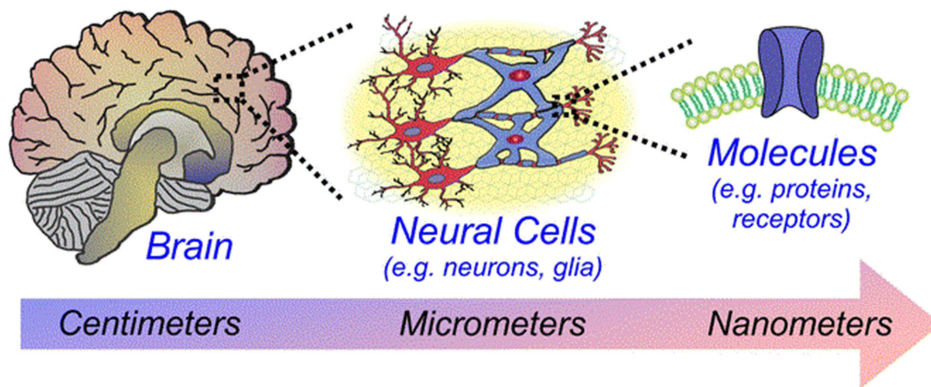


Figure 2: Anatomical organization of central nervous system at different size scales. (Shreyas Shah, 2016)

In addition to this, use of conductive materials like carbon nanotubes, microfabricated silicon and metal microwires can provide electrical properties to the scaffolds for electrical stimulation and/ or recording (Shreyas Shah 2016).

For instance, graphene oxide fabricated into grid patterns, have been able to control effective stem cell differentiation. Although the role of being electrically conductive is not clear, such grid pattern-arrays have been suggested to mimic interconnected/elongated neuronal networks (Kim TH, et al., 2015). Similarly 3D hydrogels self-assembled into nanofibrous morphology encapsulated with neural stem cells have demonstrated enhanced reconstruction of injured brain (Tzu-Yun Cheng, et al., 2013). Due to the ease of functionalization of nanomaterials, the tagging of the substrate with neurotrophic, neuroprotective or conductive substances is also widely under investigation. Various polymers for the purpose of creating such scaffold designing are put to test. One of such polymers is already used in clinic, the silicone based material-Polydimethylsiloxane (PDMS).

Silicon base materials offer wide application for use as implants, electrodes, cranial windows etc. However their dimensional and mechanical properties do not match perfectly the CNS tissue. This limitation needs to be overcome by use of nano/microfabrication techniques e.g. introduction of pores, patterns, grids or channels to implement sub cellular features (Chong Xei 2015). Introduction of nanopores or channels into silica based materials

by nanofabrication techniques can further enhance properties like cellular adhesion and tissue integration (Pennissi et al. 2010 Choi et al.,2009, Bosi et al., 2015).

Therefore, by miniaturizing the tools to target most fundamental levels of biological system, we can provide environments most acceptable to the biologic cells. To do so, careful designing and implementation of strategies is required before synthesizing a biomaterial with the aim of providing a regenerative neural interface.

## 2. Biomaterials: Designing and strategies

Biomaterial designing and optimization towards stable *in vivo* implants are challenging tasks. On one hand, biomaterials can possess unique properties that make them attractive candidates in addressing some of the previously mentioned challenges. But the choice and precise tailoring of critical parameters like surface and mechanical properties, cell adhesion, topography and biocompatibility is essential and challenging (Straley et al., 2010, Alfredsson et al., 1994, Chang et al.,). A key strategy in making a choice of the biomaterial is its fate.

### 2.1. Biodegradation of the material

Implantable biomaterials can be composed of degradable materials that slowly degrade into the tissue. These materials that are able to degrade in the biological milieu are usually composed of natural sources. Examples of such polymers include chitosan, collagen, poly( $\alpha$ -hydroxyacids) and poly( $\beta$ -hydroxybutyrate) (PHB).

Collagen, naturally found abundantly in connective tissue, was shown in *in vitro* settings to enhance growth and support fibre penetration (Gerardo-Nava J et al, 2014). Most recent studies done on collagen and fibrin hydrogel on post-natal rat pups have revealed motor axon substrate interaction. They observed motor axon growth limited to the surface in case of fibrin hydrogel block while collagen scaffold permitted growth through the microchannels (Gerardo-Nava J et al, 2014).

Chitosan, another naturally obtained polysachharide, exhibits capacities to tune properties like control degradation rate, strength and cell adhesivity of the bioscaffold (Freier et al., 2005b). Moreover, the cationic nature of chitosan polymer contributes to enhance neuronal adhesion and interaction with anionic growth factors and compounds in ECM. PHB has been introduced as longitudinal fibers to provide alignment and physical guidance to growing neurons and glial cells (Young et al., 2002). It demonstrates good tensile strength and elasticity, that prevents compression of growing neurons and has shown to bridge larger PNS injury gaps by promoting regeneration. A few drawbacks of chitosan being recently addressed are its low mechanical strength and insolubility in many solvents (Freier et al., 2005a; Yamaguchi et al., 2003b).

While these materials seem to integrate better with the biological milieu due to their natural derivation, uniformity between batches and controlled fabrication pose problems. Moreover, in terms of purification, various groups have reported difficulties in obtaining an acceptable level of purity. This is an important point because low purity can lead to enhanced activation of the immune response. Moreover, a need to understand the degradation products and their fate is of utmost importance. However, if the rate of degradation is not controlled, there can also be a risk of nerve compression (Park et al., 1995, Gautier et al., 1998; Oudega et al., 2001).

On the other hand, non-degradable materials, usually synthetic ones, require a less complex design and offer more uniform and controlled synthesis techniques. However, they are also at a higher risk of inflammation due to permanent implantation (Belkas et al., 2005; Mackinnon et al., 1984; Merle et al., 1989). Despite their inherent limitations, a simplified design or modification can result in overcoming of such limitations. Common examples of nondegradable materials include silicone, polyacrylonitrile/polyvinylchloride (PAN/PVC), poly(tetrafluoro-ethylene) (PTFE), and poly(2-hydroxyethyl methacrylate) (PHEMA). Most of the materials are not inherently cell adhesive and therefore a modification of surface properties by means of coating, nanotechnology and functionalization are employed to encourage cell adhesion. PHEMA on the other hand is currently very actively used due to its soft, tunable mechanical properties. It can easily be molded into shapes with controlled dimensions and morphology (Dalton et al., 2002). PHEMA incorporated with bioactive compound into the polymer scaffold has also been carried out (Tsai et al., 2004). In this study, poly(2-hydroxyethyl methacrylate-co-methyl methacrylate) (PHEMA-MMA) was implanted into T8 transected adult rat spinal cord. Despite of some positive results seen with PHEMA channels, a more demanding regenerative environment in the CNS have been needed. For example, making use of nanotopography and/ or imparting an electrically active environment (Shreyas shah 2016, Straley et al., 2010).

## 2.2. *Electrically active materials*

Another extraordinary design strategy is the use of electrically active materials. During the course of tissue development and regeneration, it is believed that electrically charged materials generate electric fields in ECM that act as signals to promote and control

growth, remodelling, and protein adsorption (Fine et al., 1991; Kotwal and Schmidt, 2001). Enhancement of neurite extension and controlled and enhanced outgrowth has been shown *in vitro* when cells and tissues were interfaced to electrically active materials (Patel and Poo, 1982, Fabbro et al, 2012 Cellot et al, 2009, 2011). Moreover, eliciting electrical stimulation *in vivo* promotes recovery of motor and CNS nerves (Borgens et al., 1981; Nix and Hopf, 1983). Some examples of widely investigated electrically active materials include poly(tetrafluoroethylene) (PTFE), polyvinylidene fluoride (PVDF), and polypyrrole (PP). While these electrically active polymers are non-cell adhesive, most recently a pure carbon nanotube derived substrates have been tested *in vitro* with cell and tissue interfaces (Kotov et al., 2009 and more details in section 3).

Other critical parameters for a successful biomaterial design are its mechanical properties, cell adhesivity and internal matrices or substrate architecture

### 2.3. *Mechanical cues*

Mechanical strength and properties of the material are of great importance in order to match properties with the biological anatomy and must retain integrity during the course of treatment (D.W. Hutmacher, et al., 2000). This is especially important in case of porous materials. Most implants that show promising mechanical properties *in vitro* fail *in vivo* due to insufficient capacity of vascularization. A balance between porous architecture and mechanical properties is important to allow cell infiltration and vascularization. Ideally the material should have mechanical properties consistent with the anatomical site (Fergal J., O'Brien 2011). This is true in terms of elasticity, stiffness, fatigue life etc. Several approaches like cross linking, tuning the material composition, coil reinforcement have been taken to control mechanical strength and properties of material composition (Itoh et al., 2002).

For reference, scientists have studied the mechanical properties of the spinal cord as well as brain. Human cervical spinal cord was found to have an elastic modulus of 40.12 kPa (Karimi et al., 2017). In another study conducted on rabbits, elasticity moduli between spinal gray and white matter was compared in various directions (axial, sagittal, frontal sections). A range of 2.8-3.4 kPa was found with no significant differences (Ozawa et al., 2001). Elasticity of live, dead, and fixed brain tissue resulted in an elastic modulus that varies

between  $1.0 \times 10^5$  and  $3.5 \times 10^3$  dyn/cm<sup>2</sup>; live being higher than the fixed (Metz et al., 1970) Elasticity of astrocytes range between 2 and 20 kPa (Yamane et al., 2000)

#### 2.4. Cell adhesion

The performance of the material and its biocompatibility is directly dependent on how cells interact with its surface. Cell attachment plays a key role in determining the success of the scaffold. Material designs that mimic natural environment *in vivo* can also provide contact mediated guidance for regeneration (Freier et al., 2005a).

Cell attachment onto materials can take place through two routes: (i) Non-specific adsorption and (ii) Specific adhesion, (Haipeng et al., 2000). Hydrophilicity and electrostatic interactions exhibit increased neuronal cell adhesion. E.g. chitosan and polylysine (Freier et al., 2005b; Haipeng et al., 2000).

Biomaterials modified with ECM derived proteins or peptides promote cell attachment by more closely mimicking CNS environment. Full length proteins inclusion (laminin, collagen, fibronectin) or linkage of shorter active peptide sequences to the surface of the material can be achieved for specific adhesion (Meiners and Mercado, 2003, Suzuki et al., 2003). Laminin coating and use of other ECM proteins have shown significant improvement in neural cell affinity and functional repair (Suzuki et al., 2003). Neuronal adhesion molecules (e.g. L1, expresses in growing axons and Schwann cells during development and regeneration) used as coatings have also shown positive outcomes in nerve regrowth (G. Xu et al., 2004). Due to difficulty of purification of functional proteins and the challenges in maintenance of their activity on the surfaces, use of active peptide sequences have demonstrated beneficial effects. These can mimic ECM protein function and are linked by using spacer groups or extended peptide sequences (introduced in detail further). E.g. YIGSR, RGD, and IKVAV amino-acid sequences in attributing specific functions of laminin (Meiners and Mercado, 2003, Shaw and Shoichet, 2003, Tong and Shoichet, 2001).

#### 2.5. Internal matrices

Architecture of the material in use is of great importance and can be modified by introducing internal matrices like pores, channels, ridges etc. Inclusion of internal matrices



might also increase the bioactivity and compatibility of the material *via* topographical modifications. providing an environment as close as possible to the CNS topology.

A variety of structures including channels, fibers, pores, pillars have been fabricated. These matrices also provide landscapes for cell supplementation and functionalization (Fouad et al., 2005; Nomura et al., 2008b, Novikova et al., 2008) or tagging with growth factor or neuroprotective agents. A drug delivery mechanism can also be encouraged by making use of these matrices (Bloch et al., 2001; Dodla and Bellamkonda, 2008; Tsai et al., 2006). Internal matrices contribute by providing increased surface area for neuronal attachment and invasion (Ao et al., 2006; Venugopal et al., 2008). In addition, it also provides room for adsorption of ECM components and neurotrophic factors released by regenerating cells. Channels and fibres with longitudinal orientation are believed to mimic endoneural tubules in nerves and also play role in spinal cord injury regeneration (Verdu et al., 2002). Presence of topographical cues can also serve as artificial ECM scaffolds providing contact guidance and biological cues to promote neural regeneration. Examples of such materials include use of hydrogels, carbon based substrates, collagen, matrigel, agarose and laminin (Chen et al., 2000b, Verdu et al., 2002, Wells et al., 1997, Dodla and Bellamkonda, 2008).

Collagen hydrogel blocks when introduced with microchannels permitted growth and penetration of motor axons emerging from spinal explants in-vitro. This effect was not seen when a non-porous block was used. (Gerardo-Nava J 2014)

## 2.6. *Three dimensionality of biomaterials*

Talking about architecture and design of the scaffold, we cannot neglect the dimensionality of the material. A three-dimensional (3D) environment is potentially more advantageous than two-dimension (2D), due to its similarity with native CNS topography (Bajaj et al., 2014). However, 3D bio-fabrication needs smart and accurate construction strategies and a high degree of control in fine tuning of geometry and mechanical properties. Development of 3D topologies, contribute in cell migration, spreading and proliferation (Annabi N, et al., 2010). Penetration of neuronal processes into the third dimension is expected to provide more interactive surfaces and realistic structures for ECM deposition and tissue formations. In addition, it offers physical and mechanical properties that encourage improved cell-cell

interaction and tissue like formation. This may contribute to providing microenvironments that can mimic *in vivo* situations, enhance cell attachment and facilitate function. In addition, 3D matrices may also provide room for functionalization and capturing of neuroprotective agents. Seeding of different kind of cells into 3D matrices is one of the advancing fields in neuroscience (Park, et al., 2010).

### 3. Use of Carbon nanotubes as scaffolds for neural growth

Much of current work in CNS injury repair is focussed on the development of electrically active nanomaterials and modification of these materials to provide a permissive and stimulating environment for neural rehabilitation (Fattahi et al.,2014). Carbon nanotubes (CNTs) are one of the few outstanding candidates to fulfil that purpose. This is largely due to their inherent mechanical and thermal properties, electrical conductivity and a complex nanodimensional structure that mimics biological environment (Mattson et al., 2000). Recent studies have suggested role of CNTs in several areas of CNS that demand neural regrowth and function (Ruxandra vidu et al, 2014). CNTs could either be single walled (SWNTs) or multiwalled (MWNTs) in the form of graphene sheets rolled as concentric tubes. Electrical and mechanical properties between different types of CNTs can vary a lot. Therefore, their most intriguing properties like shape, surface area, conductivity and size can be tuned as per the need (Gilmore, et al., 2008).

CNTs exhibit outstanding thermal stability and electric properties. They conduct electricity in a ballistic fashion, meaning electron transport in a medium having no electrical resistivity and no energy dissipation. They are usually chemically inert and weigh 1/6<sup>th</sup> time of steel while being twice as strong and highly conductive (with a conductivity of  $10^5$ - $10^7$  S/m) (Ruxandra vidu et al.,2014). Due to the unique properties of CNTs, various developments have been made in producing devices as probes, conductive composites, electrodes etc (Sharma and Ahuja 2008).

Functionalization of CNTs has been performed by different approaches, to modify their solubility and reduce their toxicity in order to fit biomedical applications (Bianco et al 2011). Moreover, nanotubes can be conjugated with multifunctional agents for therapeutic delivery or as vehicles (Kam et al 2005a). CNTs have shown to be readily internalized by cells while showing negligible cytotoxicity (Kam et al 2004, Kam et al 2005, Wu et al 2005). It is reported that biocompatibility of CNTs is strongly influenced by its geometry and surface chemistry (Bianco et al 2011), and therefore by understanding better the immune system and defining exposure standards, one can engineer a CNT geometry into a cyto-compatible architecture.

One of the key properties of CNTs is their ability to make intimate contacts with biological membranes. By using Scanning Electron Microscopy (SEM), information about the structure, interactions and composition of a sample can be obtained by means of electron beams swept across the specimen. Signals collected from such beams are converted into an image that has a remarkable three-dimensional quality because of the microscope's great depth of focus (Mark R. Gershenbaum and Fred J. Roisen 1981) (Figure 3, 4).

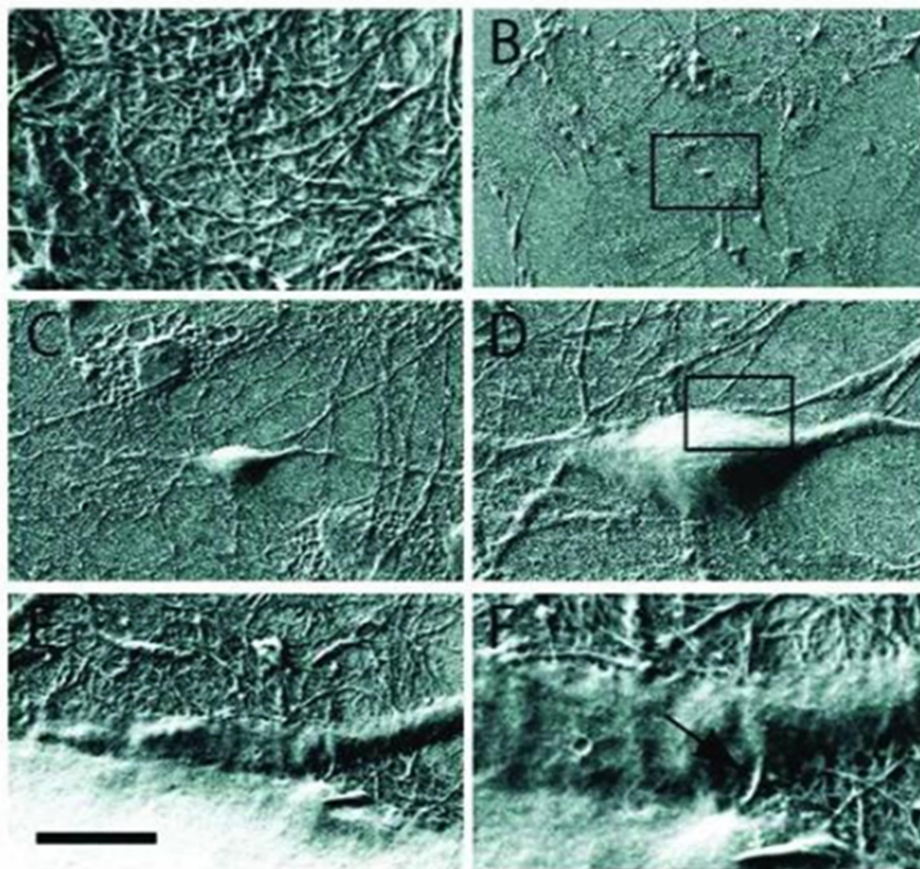


Figure 3. Scanning electron microscopy images showing close and intimate contacts between SWCNTs substrate and the neuronal membrane of cultured hippocampal neurons. Scale bar (in E): A, 1  $\mu\text{m}$ ; B, 200  $\mu\text{m}$ ; C, 25  $\mu\text{m}$ ; D, 10  $\mu\text{m}$ ; E, 2  $\mu\text{m}$ ; F, 450 nm (Mazzatenta et al., 2007).

Tight interactions between cell membranes and SWNTs were observed. This observation encourages a stable electrical interfacing between neuronal membranes and SWNTs. This study was done on hippocampal neuronal cultures (Mazzatenta et al., 2007) (Figure 3).

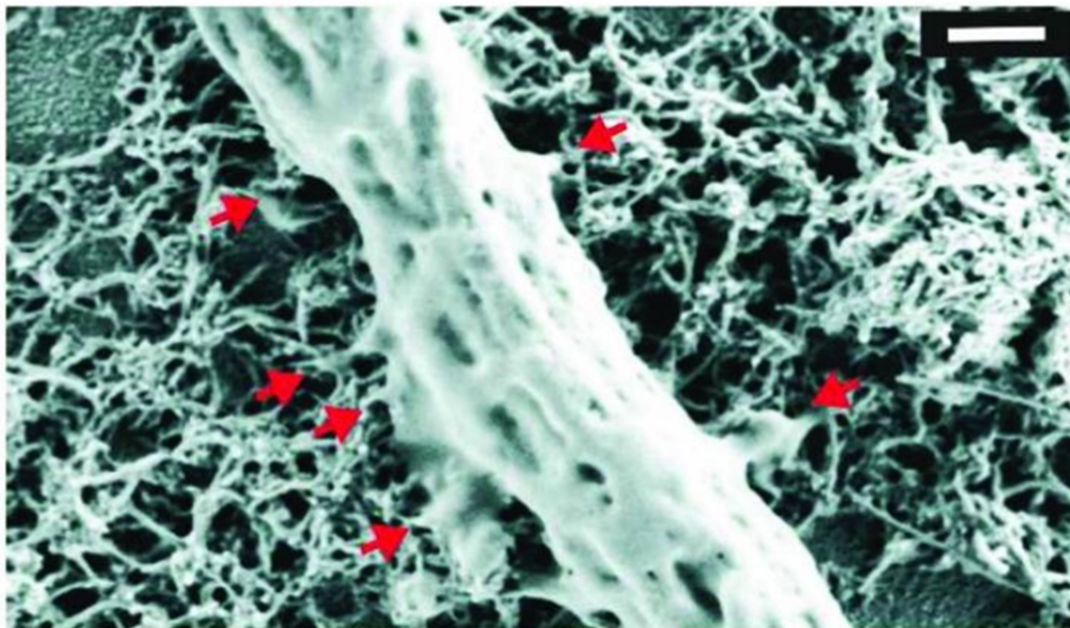


Figure 4. SEM image shows MWNTs tightly anchored to (red arrows demonstrate intimate contacts) peripheral neuronal fiber emerging from spinal cord explant (Fabbro et al., 2012) Scale bar 500nm

In more complex systems, like organotypic spinal tissue cultures, SEM displayed MWNTs forming tight contact with peripheral neuronal fibers emerging from spinal explants. Growing cultured spinal explant displayed similar tight junctions between membranes and MWNTs (Fabbro, et al., 2012) (Figure 4)

In addition to this, CNTs have been reported to have the ability to instruct growth leading to desirable organization of neural networks *in vitro* (Figure 5).

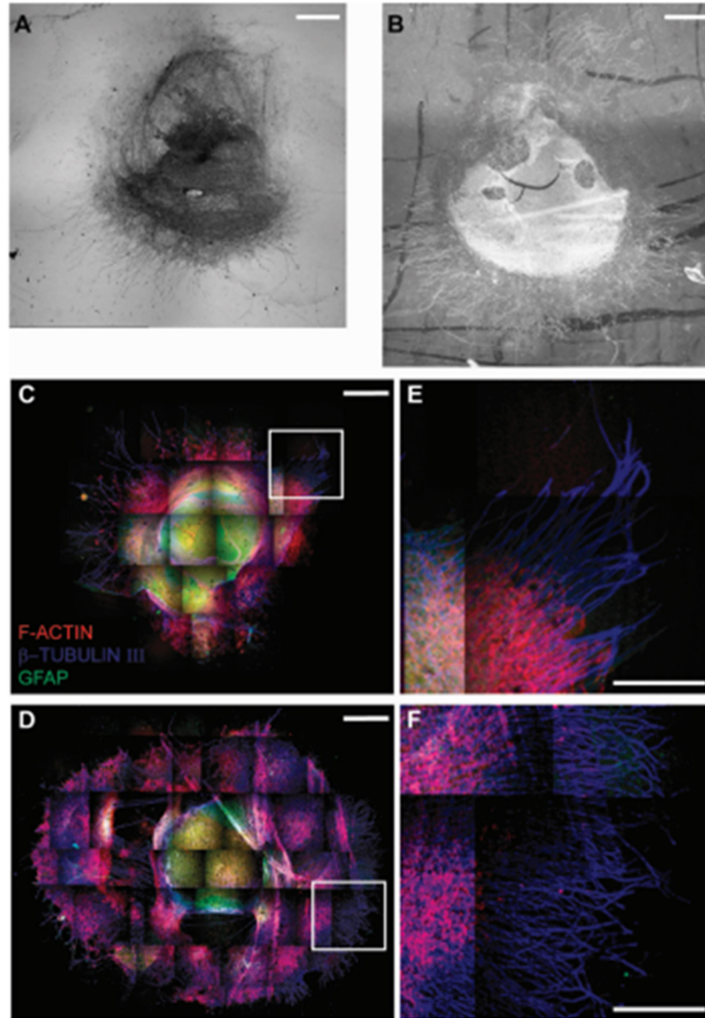


Figure 5. Impact of MWCNT interfaces on neurite outgrowth from organotypic spinal cultures. (A,B) Bright-field and phase contrast images taken of spinal explants in control and carbon nanotube substrates, respectively after 8 DIV of growth demonstrate larger outgrowth area of the spinal explant when interfaced to MWCNTs. (C,D) Confocal image reconstructions of spinal slice cultures at 8 DIV, under control and CNT growth conditions, respectively. Immuno-labelling of specific cytoskeletal components, (F-actin,  $\beta$ -tubulin III, and GFAP).  $\beta$ -tubulin III positive neuronal processes radially exiting the growth area in MWCNT interfaced explant are larger in number and travel longer distances. (E,F) High confocal magnifications of the framed areas highlighted in C and D, respectively, C-F: green, GFAP; red, F-actin; blue,  $\beta$ -tubulin III. In A-D: scale bar 1 mm. In E,F: scale bar 500  $\mu$ m.

In cultures of spinal cord slices grown on MWNTs, significant increase in number of outgrowing fibers has been reported. Not only that, the emerging fibers from spinal cord explants travelled longer distances from the edge of the outgrowing belt in radial fashion (Fabbro et al., 2012) (Figure 5). Neurites that were in contact with CNTs were noted to have altered elasto-mechanical properties. This study was done by the use of Atomic force microscopy; neurites interfaced to CNTs demonstrated flattening as well as lower stiffness than controls (Fabbro et al., 2012). In addition to this, exploiting different patterns of CNTs for e.g. vertically aligned patterns have shown to guide neural growth (Zhang X, et al., 2005, Nguyen-Vu, et al., 2007)

Remarkable improvements in the functional organization and synaptic frequency of events performance have been demonstrated in neurons interfaced to 2D MWCNTs (Cellot et al., 2009, 2011; Fabbro et al., 2012, 2013; Lovat et al., 2005; Mazzatenta et al., 2007). This improved neuronal signaling leading to an electrically favorable environment might have a role in aiding cell maturation and neuronal network formation. CNT improved spontaneous synaptic activity and firing of hippocampal neuronal cultures (Lovat et al., 2005) (Figure 6). In more complex multilayer tissue structures MWCNTs attributed to increased synaptic efficacy in neurons located as far as 5 cell layers from the substrate (Fabbro, et al., 2012). These findings done *in vitro* suggest that mechanically derived microenvironments can affect biochemical signaling that can play significant role in CNS reconstruction.

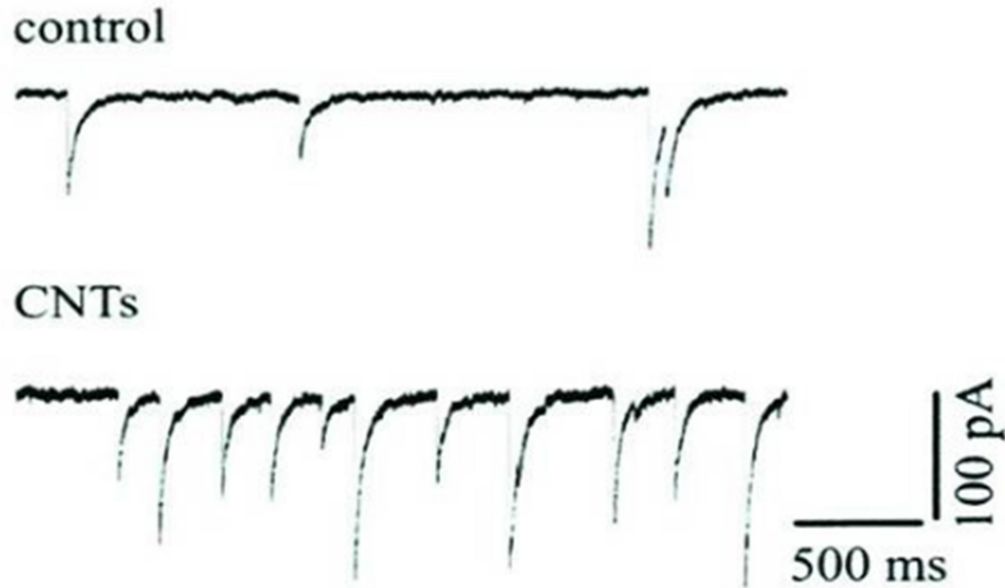


Figure 6. Representative voltage-clamp recordings of postsynaptic currents (PSCs) recorded from hippocampal neurons cultured on glass (control) or on CNT substrates demonstrate a significant increase in PSC frequency (Lovat et al., 2005)

### 3.1 Pure carbon nanotube 3D scaffolds

Much of the understanding of neural interfaces has been gained by studying 2D structures/devices, however more recently biologists have come to understand the dissimilarity between the flat surfaces and the 3D topographical complexes i.e. the extracellular environment in which cells routinely operate *in vivo* (Baker et al., 2012). Ghibaudo and team in 2009 reported differences in cellular interactions between 2D and 3D substrates. They assessed cellular adhesion and migration of fibroblasts in both conditions. Cells interfaced to 3D microenvironment showed more elongated and branched shapes. Thus, 3D offers more control on size and shape of the substrate and cellular morphology than traditional 2D substrates (Ghibaudo et al, 2009).

Carbon nanotubes fortunately present tunable properties that can lead to modification of their dimensions. Gui et al., have molded CNTs into a porous sponge of 3D with a very high porosity while retaining desired mechanical properties. The sponge structure obtained was very stable and in fact allowed excellent compressibility and ability to recover volume



by free expansion. 3D scaffold discussed in the literature maintained good contact and percolation and polymer infiltration. (Xuchun Gui et al., 2010).

Moreover, CNTs as implantable materials can also easily be tagged with biomolecules or polymers. Using a polymer incorporated with CNTs can serve desired mechanical and physical properties as well as offer favorable electrical environment elicited by CNTs. Due to their biological applications, and resistance to biodegradation, CNTs have proved to be one of the promising choices for brain or spinal implantable materials or devices e.g scaffold, electrodes, other neural interfaces. In order to further enhance neuronal performance or detect existing neuronal connections, optimized electrical stimulations can be delivered to CNTs or CNTs-entrapped-polymer. These strategies can be exploited all together to build scaffolds that can trigger improvements in neuronal network formations and functional tissues.

For our study, we have used pure three-dimensional carbon nanotube network synthesized by Professor Maurozio Crescenzi. These networks were self-assembled, freestanding 3D meshes of entangled MWCNTs (3D CNF or CNF) in the form of a random skeleton with interconnected pores. (Camilli et al, 2013) (Figure 7). MWCNTs were mm long and 0.4  $\mu\text{m}$  in diameter and were obtained by chemical vapor deposition . Briefly nitrogen was inserted into air free hot-wall quartz furnace using ferrocene as a catalyst and thiocene as a sulfur precursor. Argon and acetylene were used as gas carrier and as the carbon precursor. The temperature was maintained at 150°C to allow fast vaporization of injected liquids (Camilli et al 2014).

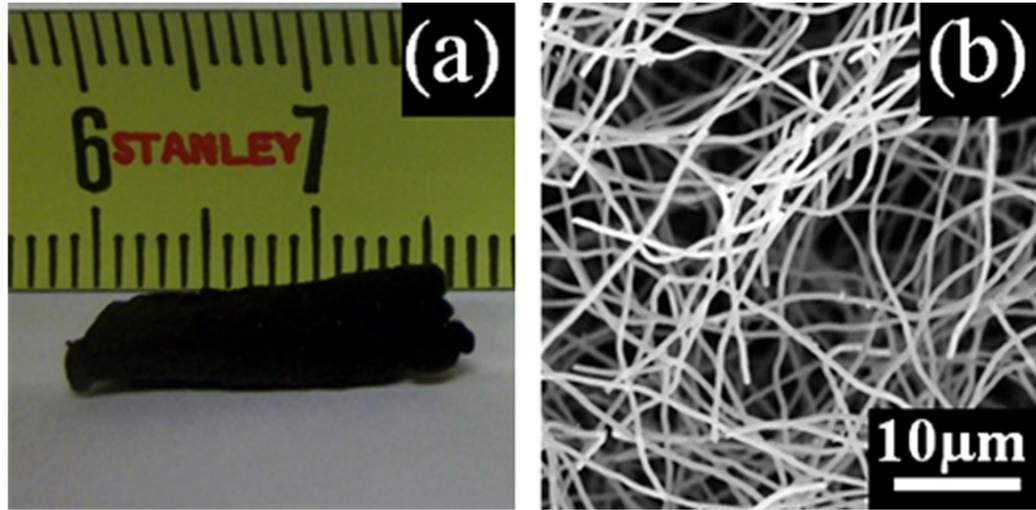


Figure 7: (a) Picture of CNT network (b) Scanning electron microscopy (SEM) of representing its porous structure. (Camilli et al., 2013)

As reported, the electrical conductivity of this material was reported 0.035 S/cm and it linearly increased to about 615% with applied compression. Figure 8 represents effect of compression on the conductivity of the material. (Camilli et al, 2013). The increase in conductivity on applied compression is ascribed to the increased contact point between adjacent CNTs within the network giving rise to new percolating pathways for charge carrier. When the pressure was applied, the intertube pores squeeze making the CNT denser leading to more CNTs touching each other. The removal of pressure or compressive load from the material, resulted in full recovery of its original shape, number of contact points and electrical conductivity to the initial values.

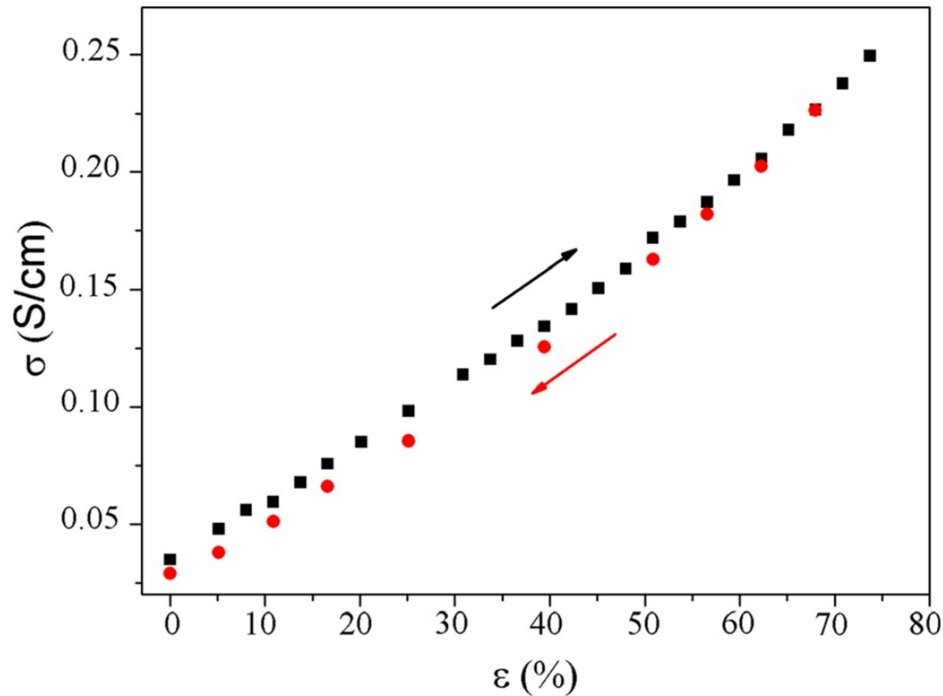


Figure 8: Plot represents relation of conductivity of the CNT network (3DCNF) with compressive strain under load (black squares) and release (red dots) (as reported in Camilli et al., 2013).

The plot (Figure 8) also demonstrates the elastic properties of the CNT network. The material sustained compressions up to 75% and elastically recovered its morphology and conductivity during the release period. The elasticity of this material was about 5kPa (within the range of rodent and human brain tissue stiffness 0.1-20 kPa; Tyler 2012).

### 3.2 PDMS and its functionalization with CNTs

Silicon based scaffolds have widely been used in clinical applications as neural electrode devices and implants. One such derivative is a highly flexible and tunable polymer called as polydimethylsiloxane (PDMS). Due to the inherent flexible capacity of PDMS, it can be molded into different shapes and space filling agents making it more ideal for implantation into complex CNS injury sites within spinal cord and/or brain. Another important property of PDMS is the ease of fabrication of this material into soft three-dimensional structures which can mimic *in vivo* ECM environment. PDMS can readily be

tailored to any size or shape. It is soft, flexible, penetrable, and elastic and most importantly can provide landscapes for functionalization/customization options. (Guo et al 2013,. Heo et al 2017,)

Three dimensional structures of PDMS can easily be customized into desirable structures of micro or nanodimension of high porosities. This is due to the mechanical characteristics of this polymer. These properties of PDMS can be used to design platforms for porous polymer networks for the purpose of neural tissue interfaces.

PDMS has been used successfully as an artificial dura with microchannel to deliver drugs and electrically conductive gold coatings for eliciting electrical stimulation (Chaejeong Heo, et al., 2016, Minev, et al., 2015). It has also been used as a substitute for the skull and dura to introduce a cranial window. The purpose of this study was to allow ease of insertion of microelectrodes and micropipettes into cortical tissue for electropysiological recording and chemical injection. In both studies, a low immune reaction to PDMS was observed (Chaejeong Heo, et al., 2016, Minev, et al., 2015).

While *in vivo* studies have shown limited astroglial to PDMS when implanted into rat cortex (Lu Wang et al 2009, Pennisi et al., 2010), the surface properties of this material fail to integrate with neural tissues. This can however be achieved by various nanofabrication techniques, for e.g layering PDMS with a bioadhesive material.

Cellular adhesion and tissue integration can further be enhanced by employing such customization techniques and/or functionalization with a bioadhesive material. For instance, use of peptide laminin or carbon nanotubes can further improve properties of silicon-based materials for therapeutic applications (Pennisi et al., 2010 Choi et al.2009). Since the use of PDMS as a neural substrate ranges from cell seeding to neural electrical devices, it would be a great advantage to customize PDMS with electrically active materials such as CNTs. This approach can not only aim at improving surface interaction with biological membranes but can also provide properties attributed to electrically active materials (as previously described).

A recent study demonstrated use of 3D PDMS scaffold constituting interconnected micropore structures of very high porosity, shown in Figure 9 and Figure 10. The pore size and geometry of the material was derived from a mold of crystalline sugar allowing cellular

penetration of hippocampal neurons and adequate diffusion of nutrients to the cells. (Bosi et al., 2015)

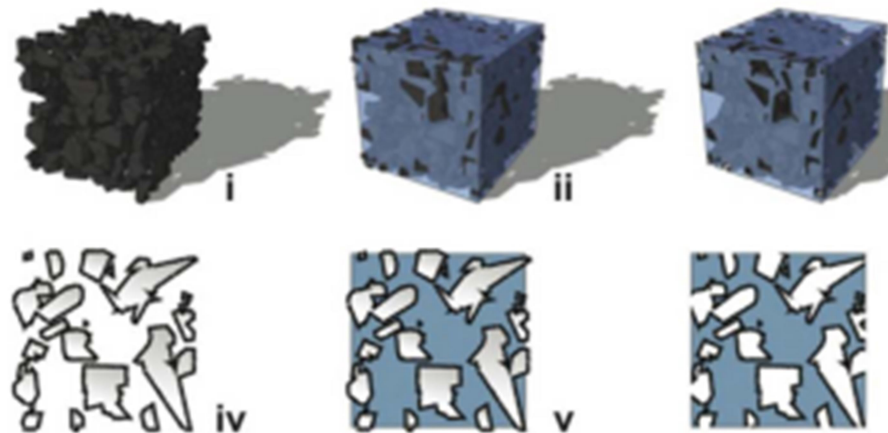


Figure 9. Fabrication steps of the PDMS scaffold (i) the starting sugar mould entrapped with MWCNTs (ii) uncured PDMS forced via a vacuum process within the mould (iii) after PDMS heat curing the sugar framework is dissolved leaving a self-standing PDMS replica enriched with MWCNTs lining the contours of the pores; from (iv) to (vi) sketched cross sections of the previous steps. (Bosi et al., 2015)

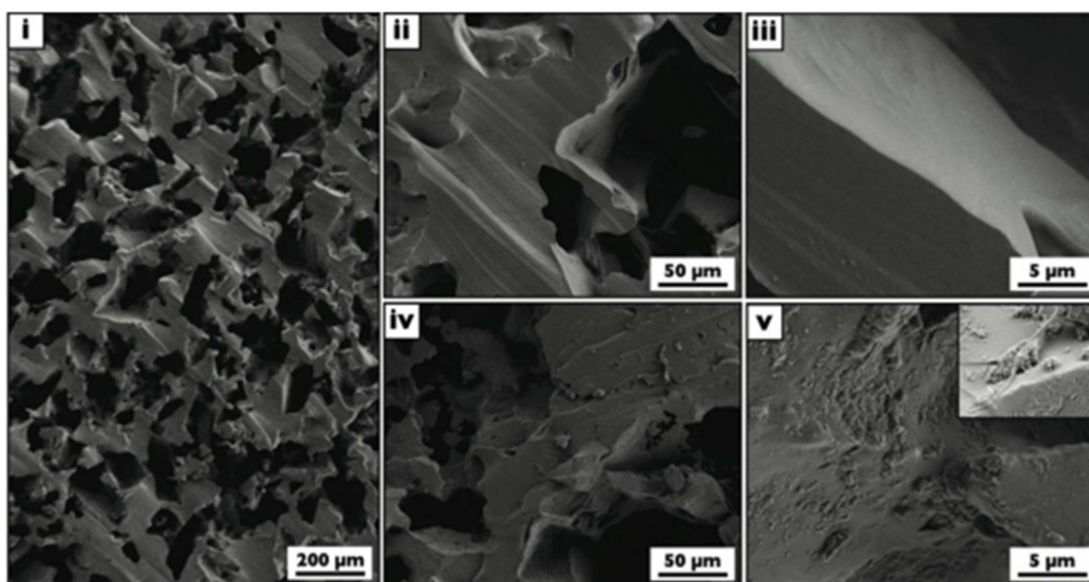


Figure 10. SEM images of the PDMS based scaffolds: (i) PDMS scaffold. (ii) and (iv) higher magnification images of PDMS and PDMS-MWCNTs scaffolds, respectively; (iii) and (v) higher magnification details of the previous images. In (iv) and (v) exposed MWCNTs at the surface are visible. Inset in (v) a cell process in contact with the carbon nanotubes. (Bosi et al., 2015)

#### 4. Functional neurological impairment following spinal cord injury

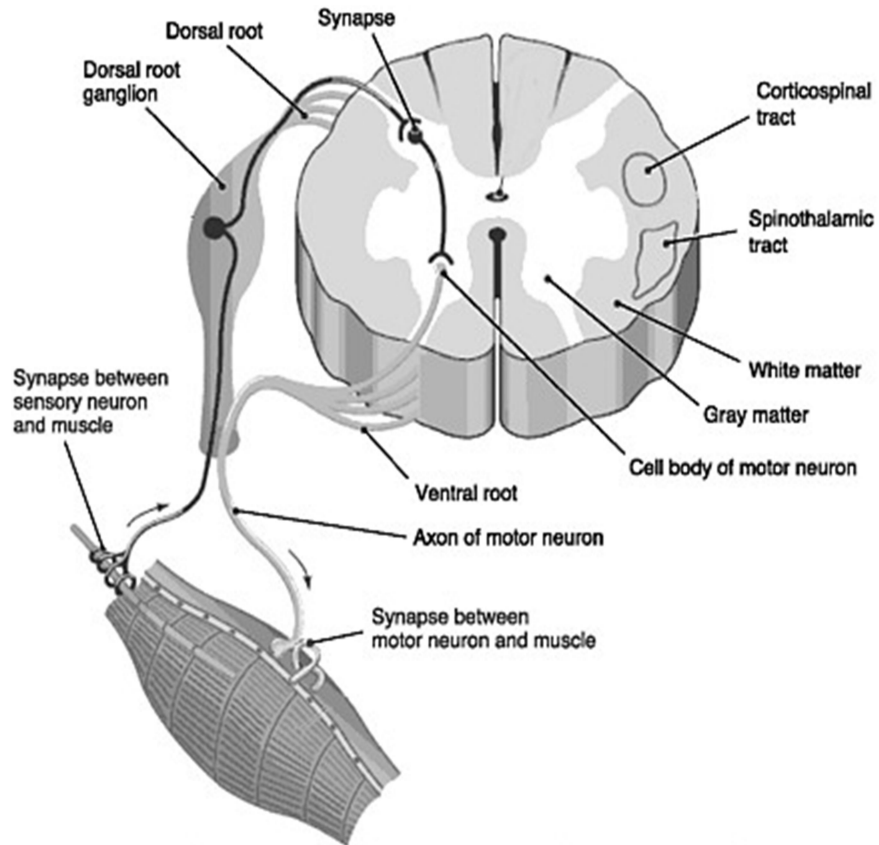


Figure 11. Cross section of the spinal cord (Taber and Thomas 1997)

Spinal cord is the part of the CNS that connects brain to all muscles of the body and most sensory nerves to brain. Surrounded by a protective vertebrae, the outer edge of the spinal cord is white matter which contains branching portions of nerve cells known as axons wrapped around by fatty white substance –myelin. Myelin helps to speed up the nerve impulse from brain to rest of the body. Cell bodies of these axons are clustered together in gray matter of the spinal cord (a central butterfly shaped structure within the spinal cord). Gray matter composes of ventral and dorsal horns. Ventral horn contains cell bodies of motor neurons while dorsal horn contains primary sensory pathways. Cell bodies of sensory neurons lie outside the spinal cord in clusters known as dorsal root ganglion (Figure 11).

Despite intensive studies towards finding solutions for CNS disease or injuries, there is a need for groundbreaking research to find an efficient approach to address areas such as spinal cord post injury. Every year there are roughly 17,000 cases of SCI reported in US alone (<https://www.nscisc.uab.edu/Public/Facts%202016.pdf>).

Despite recent advances in supportive care, after SCI, there is essentially no regrowth of axons beyond the point of the lesion, leaving intact, although nonfunctional, circuits below the site of injury. Because SCI interrupts axons and alters myelination, which impairs sensory and motor pathways, recovery of lesion in spinal tissue involves regeneration of the long neuronal tracts mediating such functions. Neuroregenerative strategies include implantable synthetic scaffolds, that can be engineered to contain electrodes for recording and stimulation; however, the state-of-the-art is far from reaching optimal stability of the device at the synthetic-biological interface (Marchesan et al Science 2017). Typically, implants are composed of stiff and static materials defined at best to the micrometer scale, that are ultimately rejected by the human organism. In fact, as previously addressed, the biggest challenge that neural interfaces face *in-vivo* is their biocompatibility. An immune reaction elicited in response to a scaffold and the extent of the reaction determines majorly how safe the implant is. Immune reaction *in vivo* can be measured by means of identifying and quantitatively analyzing the markers for inflammation. By the use of histology, various markers like Iba1 (microglia), ED1 (reactive microglia), GFAP (astrocytes) can be exploited to quantify the thickness of gliotic scar post implantation. A limited or negligible gliotic reaction permits better integration of the material with biological tissue, hence allowing it to compensate for damaged neural function by providing a neuron-permissive environment at different stage of SCI.

Spinal cord injury triggers a cascade of biological events that occur from within seconds proceeding for months or even years. It involves nervous system, immune system and vascular system. These systems interact dynamically in response to injury. Tissue damage following SCI can expand beyond the site of injury. A final outcome of a serious spinal cord injury is loss of reflexes, loss of sensation and paralysis.

In order to inspire a smart approach to repair injured tissue, it is important to have an understanding of pathophysiology, biochemical pathways and progression of SCI.



On the basis of pathology spinal cord injuries can be classified as contusion, laceration and solid spinal cord injuries. Types of spinal cord injury, severity and its level determine the prognosis and functional damage.

Type of Spinal Cord Injury	Percentage of Total Injuries	Description
Contusion	25 to 40	Bruising, but not severing, of the spinal cord
Laceration	25	Severing or tearing of the spinal cord and introduction of connective tissue into the spinal cord, typically from gunshot or knife wounds
Solid cord injury	17	Axon injury and demyelination

Table 1. Types of spinal cord injury (Source: Progression of spinal cord injury; Bunge et al, 1993, 1997, Harper et al., 1996, Hulsebosch, 2002)

Acute (Seconds after Injury)	Secondary (Minutes to Weeks)	Chronic (Months to Years)
<ul style="list-style-type: none"> <li>• Systemic hypotension and spinal shock</li> <li>• Hemorrhage</li> <li>• Cell death from direct insult or ischemia (disruption of blood supply)</li> <li>• Edema (swelling)</li> <li>• Vasospasm (reduction in blood flow)</li> <li>• Shifts in electrolytes</li> <li>• Accumulation of neurotransmitters</li> </ul>	<ul style="list-style-type: none"> <li>• Continued cell death</li> <li>• Continued edema</li> <li>• Continued shifts in electrolytes</li> <li>• Free-radical production</li> <li>• Lipid peroxidation</li> <li>• Neutrophil and lymphocyte invasion and release of cytokines</li> <li>• Apoptosis (programmed cell death)</li> <li>• Calcium entry into cells</li> </ul>	<ul style="list-style-type: none"> <li>• Continued apoptosis radiating from site of injury</li> <li>• Alteration of ion channels and receptors</li> <li>• Formation of fluid-filled cavity</li> <li>• Scarring of spinal cord by glial cells</li> <li>• Demyelination</li> <li>• Regenerative processes, including sprouting by neurons</li> <li>• Altered neurocircuits</li> <li>• Syringomyelia</li> </ul>

Table 2. Major features of the three phases of SCI (Source: Progression of spinal cord injury; Sekhon and Fehlings 2001, Hulsebosch, 2002)

Biological responses to a SCI can be divided based on temporal sequences into acute (seconds to minutes after the injury), secondary (minutes to weeks after the injury), and chronic (months to years after the injury). Various cells and molecules from nervous, immune and vascular systems are involved in each phase. Such events that are designed to heal the injury can paradoxically lead to further neuronal injury or death spreading up to four spinal segments adjacent to the site of injury (Crowe et al., 1997; Liu et al., 1997).

Series of such pathological events can also result into other complications like haemorrhage, oedema, neuronal necrosis, axonal fragmentation, demyelination of the remaining axons, and formation of cyst (Syringomyelia). Neural cell death and series of sequential biochemical pathological deviations can cause disruption of blood supply to the site of injury. Filling up of immune cells into the affected area, result into formation of a 'glial scar'. Glial scar and its expansion is the major factor that hampers regeneration post CNS injuries. Glial scar consists of astrocytes and fibroblasts and growth inhibiting molecules derived from breakdown of damaged nerve cells, such as chondroitin sulphate

proteoglycans. These inhibit axon growth by forming a physicochemical barrier for regeneration (Figure 12).

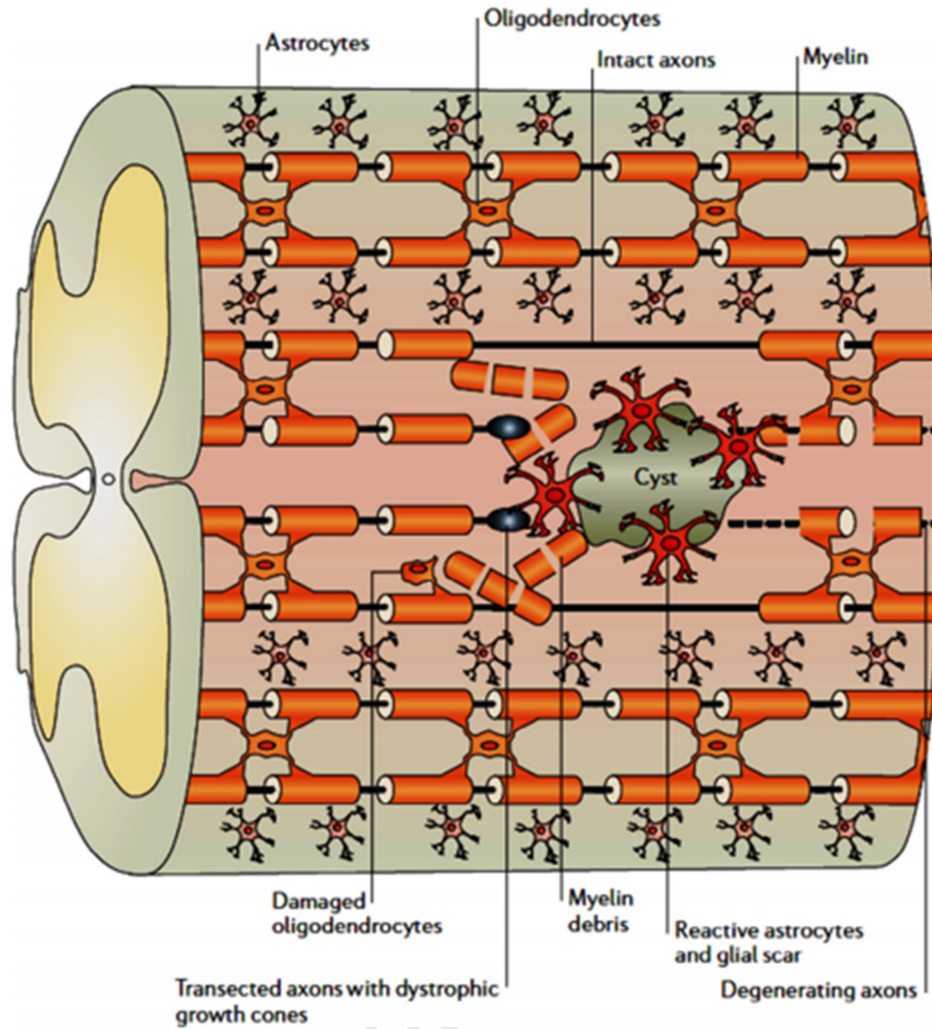


Figure 12. Schematic representation of injured spinal cord (Yiu and He 2006)

## 5. Mechanisms of spontaneous recovery

In case of incomplete spinal injuries, most individuals show substantial degrees of recovery (Tator et al., 1998). Since mature nerve cells lack the capacity to divide once injured, this natural recovery is largely a result of plasticity in the surviving neurons.

### **Mechanisms of spontaneous recovery after SCI**

---

- Remyelination by Schwann cells entering the spinal cord after injury
- Remyelination by oligodendrocyte precursors
- Recovery of conduction in demyelinated axons
- Strengthening of existing synapses
- Regrowth and sprouting of intact axons to form new circuits
- Release of growth factors and guidance molecules
- Shift of function to alternate circuits

Table 3: Source: SCI: Progression of spinal cord injury.

Some degree of re-myelination can take place leading to spontaneous recovery either by Schwann cell migration from PNS or by means of oligodendrocyte precursor cells (Bunge and Wood, 2004). It may also be possible for demyelinated axons may reorganize at molecular levels acquiring ability to conduct nerve impulses without myelin insulation. Regrowth of axons and sprouting of new branches of existing axons forming new synapses can be another mechanism for functional recovery (Raineteau and Schwab, 2001). Studies have also reported production and release of certain growth promoting molecules (neurotrophins) by surviving cells (Raineteau and Schwab, 2001).

## 6. Organotypic spinal cultures in material screening

Mechanistic studies of the interplay between neural interfaces and nervous tissue may require sophisticated *in vitro* models tested in the laboratory to investigate spinal tissue responses at cellular resolution, prior to implantation *in vivo*. It is necessary to study *in vitro* effects of a possible approach, before moving further to implantation into *in vivo* live brain or spinal models (Saracino et al., 2013, Gilbert RJ et al., 2011). One of such model widely used, accepted and deeply investigated is of organotypic spinal cord slices obtained from embryonic rats or mice (Pandamooz et al., 2015).

Organotypic slice cultures developed from the embryonic mouse spinal cord represent a complex *in vitro* model where sensory-motor cytoarchitecture, dorso-ventral orientation, synaptic properties and spinal cord resident cells are retained (Gawhiler et al., 1997, Streit et al., 1991, Pena F et al., 2010, Avossa et al., 2003; Furlan et al., 2007). Decades of development of organotypic cultures in our lab have reported use of organotypic cultures in studying neural network dynamics. This is due to the fact that these long term cultures preserve electrical properties maintained well at synaptic levels. The choice of organotypic slice preparation can be embryonic or neonatal, since the essential cytoarchitecture of CNS is already established in both cases. Earlier stages, in fact show more survival compared with adults (Gawhiler, 1997).

It is important to note the developmental differences associated with the spinal circuit since they play a major role in shaping ventral outputs emerging from spinal slices. In mouse spinal cord, spontaneous rhythmic activity can be seen in early stages of embryogenesis, prior to the completion of muscular innervations, however this spontaneous activity is different from late locomotor like activity. The differences are mainly in the aspects such as firstly; early spontaneous activity is in the form of synchronized episodic bursts across the rostro-caudal extent of the spinal cord. The generation of the activity is not mediated by glutamate but rather excitatory drive is supplied by GABAergic, glycinergic and cholinergic transmissions (Hansen and Landmesser, 2003). Lastly the generation of spontaneous activity at early embryonic age is mediated by chemical and electrical transmissions unlike later neonatal rodents where chemical transmissions predominate (Tresch and Kiehn 2000).

The presence of this spontaneous rhythmic activity is primarily due to predominant excitatory nature of developing synaptic connections (as GABA and glycine are excitatory at this stage) and the presence of activity dependent depression of neuronal and network excitability (O'Donovan et al 1998).

Early stages of development *in vitro*, (1 week) is started to be considered a late embryonic stage and at this age, a synchronous bursting activity is displayed by ventral interneurons. This activity plays an essential role in driving muscle contractions. Further 2-3 weeks *in vitro*, represent early postnatal phase, and at this phase, the activity drastically reduces and also its correlation with motor responses (Rosato-Siri et al 2004).

Role of GABA and glycine; the two major inhibitory neurotransmitters tend to have an interplay during spinal circuit development. At early fetal periods, immature high intracellular chloride concentrations, upon GABA and glycine receptor activation result in depolarizing response; playing a role in neuronal growth and differentiation due to elevated cytoplasmic calcium (Cherubini et al 1991), Gao et al 2001). This depolarizing effect mediated by inhibitory components, diminish as neuron mature. In addition to this, during this phase, a transition of GABAergic synapses to glycinergic synapses on motor neurons take place. This GABA glycine interplay together, eventually play a dominant role in driving sensory and motor patterns of activity specifically motor neuron outputs from ventral horn of the spinal cord.

Due to the dynamic characteristics of such organotypic spinal models, they are known to be partly mimicking the *in vivo* environment (Ravikumar et al., 2012). Electrophysiological experiments like patch clamp recordings, local field potential recordings and multi electrode arrays can very conveniently be performed to detect changes in neural activity when interfaced to different environments. These recordings can include spontaneous synaptic activity, rhythmic activity induced by pharmacological treatment and response to stimulation (Fabbro et al., 2012, Avossa et al., 2003). Rhythmic activity can be triggered at later post natal phase by a pharmacological block of GABA and glycine receptors, giving rise to glutamatergic bursts or rhythmic patterns of activity also called as 'disinhibited bursting' (Streit J, 1993).

This activity can be exploited in organotypic spinal cord slices used singularly, or in pairs to investigate synaptic reconnection due to network interactions. Previous studies have

demonstrated failure in reconnection of separated organotypic spinal slices at a distance larger than 300  $\mu\text{m}$  (Heidemann et al., 2014). This study was performed on E14 rat embryonic spinal cord sections. Transverse spinal sections were co-cultured and a lesion was made at a time window of 8-28 days *in vitro* (DIV). Authors recorded spontaneous extracellular neuronal activity 2-3 weeks post-lesion. While lesions made at 7-9 days showed higher synchronization due to reconnection, co-cultures lesioned at more than 19 days showed distinct reduction in reconnection under basal conditions (Heidemann et al., 2014).

This failure to reconnect spinal segments can be used as a tool to study various interfaces, materials or efficacious cues that may or may not play roles in forming potential reconnection of spinal cord networks.

## 7. Tools for assessing spinal cord injury and repair

Since the spinal cord is encased in a protective surrounding of vertebrae, it is challenging to gain access to spinal cord readily. While many *in vitro* techniques have been put to use, by isolating cells and tissues, it is of utmost importance to put to evaluate any strategy into a live animal model. It helps to examine and verify results obtained under *in vitro* in a more complex biological system. It is also not necessary that *in vitro* results show similar outcomes when tested in animal models (Snow et al., 1990, Bradbury et al., 2002).

Animal models provide in-depth understanding of anatomical and molecular changes occurring in response to SCI. These insights play critical role in interpreting results before trying them on humans.

To achieve this purpose, various animal models have been determined with an attempt to closely replicate injury in humans. Most important characteristics for an optimal model of SCI injury include precise nature and extent of the lesion, a histological method to evaluate immune markers and neuronal growth through lesion, recording electrical activity to analyze functional synaptic transmissions beyond lesion, and lastly a behavioral measure for detecting restoration of known circuits (Ramer et al., 2000)

### Value of Animal Models for Spinal Cord Injury Research (Spinal cord injury)

- Allows in-depth investigation of the anatomical changes that occur in response to an injury
- Regeneration of axonal tracts between the brain and the spinal cord can be studied in detail
- Individual components of the complex neural circuitry required for sensory perception and motor control can be examined
- Factors that influence DNA and proteins can be characterized
- Provides a means to examine the effects of specific genes
- Provides a tool to identify and test the efficacies of potential therapeutic agents and targets
- Identifies clinical end points that can be used to assess the efficacies of therapeutic agents



In order to understand prognosis and severity of the injury, a standard way of grading the functional severity of a SCI is followed. This is achieved by clinicians by the use of American Spinal Injury Association (ASIA) Impairment scale. Similarly to assess severity of SCI in animal models and to present standards for reliable rating, Basso Beattie, Bresnahan (BBB) locomotor rating scale is used. The purpose of this scale is to set efficient, elaborate and unambiguous way to compare inter-laboratory locomotor outcomes (ASIA 2000, Basso et al., 1995). BBB rating scale is largely used to compare functional motor recovery post SCI in rats with injuries below thoracic levels.

---

0	No observable hind limb (HL) movement.
1	Slight movement of one or two joints, usually the hip and/or knee.
2	Extensive movement of one joint or extensive movement of one joint and slight movement of one other joint.
3	Extensive movement of two joints.
4	Slight movement of all three joints of the HL.
5	Slight movement of two joints and extensive movement of the third.
6	Extensive movement of two joints and slight movement of the third.
7	Extensive movement of all three joints of the HL.
8	Sweeping with no weight support or plantar placement of the paw with no weight support.
9	Plantar placement of the paw with weight support in stance only (i.e., when stationary) or occasional, frequent, or consistent weight supported dorsal stepping and no plantar stepping.
10	Occasional weight supported plantar steps, no forelimb (FL)-HL coordination.
11	Frequent to consistent weight supported plantar steps and no FL-HL coordination.
12	Frequent to consistent weight supported plantar steps and occasional FL-HL coordination.
13	Frequent to consistent weight supported plantar steps and frequent FL-HL coordination.
14	Consistent weight supported plantar steps, consistent FL-HL coordination; and predominant paw position during locomotion is rotated (internally or externally) when it makes initial contact with the surface as well as just before it is lifted off at the end of stance or frequent plantar stepping, consistent FL-HL coordination, and occasional dorsal stepping.
15	Consistent plantar stepping and consistent FL-HL coordination; and no toe clearance or occasional toe clearance during forward limb advancement; predominant paw position is parallel to the body at initial contact.
16	Consistent plantar stepping and consistent FL-HL coordination during gait; and toe clearance occurs frequently during forward limb advancement; predominant paw position is parallel at initial contact and rotated at lift off.
17	Consistent plantar stepping and consistent FL-HL coordination during gait; and toe clearance occurs frequently during forward limb advancement; predominant paw position is parallel at initial contact and lift off.
18	Consistent plantar stepping and consistent FL-HL coordination during gait; and toe clearance occurs consistently during forward limb advancement; predominant paw position is parallel at initial contact and rotated at lift off.
19	Consistent plantar stepping and consistent FL-HL coordination during gait; and toe clearance occurs consistently during forward limb advancement; predominant paw position is parallel at initial contact and lift off; and tail is down part or all of the time.
20	Consistent plantar stepping and consistent coordinated gait; consistent toe clearance; predominant paw position is parallel at initial contact and lift off; tail consistently up; and trunk instability.
21	Consistent plantar stepping and coordinated gait, consistent toe clearance, predominant paw position is parallel throughout stance, consistent trunk stability, tail consistently up.

---

Originally published in Journal of Neurotrauma, Volume 12, Number 1, 1995.

Table 4. BBB locomotor rating scale used for assessment of functional recovery of SCI-injured rats. It is a 0-21 rating scale, where 0 denotes no hind limb movement while 21 stands for a normal gait (Basso 1995)

Behavioral tests are used to provide insights to distinct aspects of motor function in order to determine even subtle loss of movement capacity. Pre-trained animals are made to perform various tasks in order to examine their locomotor function. Foot fault test or ladder rung test and foot print analysis or FPA are such behavioral tests used for assessment of function related to motor function.

Foot fault test or ladder rung test reveals deficits in locomotor function which are not apparent during a normal gait. Limb placing, stepping and motor control, are used as parameters for scoring the performance of the animals (Metz et al., 2009). FPA on the other hand is a sensory-motor test that evaluates walking stability, body balance and inter-limb placement. Measures of stride length, base of support and angle of rotation, give insights to functional muscular innervations (Scali et al., 2013)

Due to complex environmental conditions of CNS, it is necessary to investigate responses of a biomaterial in simple and further complex models before its translation into clinics.

Therefore, keeping in consideration biomaterial strategies and biological milieu post CNS injury, we were prompted to investigate biological interactions and impact on neurite growth, electrical activity and synaptic connections *in vitro* as well as biocompatibility *in vivo* for 3D freestanding pure meshes of CNTs as well as its functionalized analogs composed of PDMS skeleton. Our focus is to understand morphological, anatomical, electrical and functional response of neural cells by using above mentioned interfaces.

# 3D meshes of carbon nanotubes guide functional reconnection of segregated spinal explants

Sadaf Usmani,<sup>1\*</sup> Emily Rose Aurand,<sup>2\*</sup> Manuela Medelin,<sup>2</sup> Alessandra Fabbro,<sup>2</sup> Denis Scaini,<sup>2,3</sup> Jummi Laishram,<sup>2</sup> Federica B. Rosselli,<sup>1</sup> Alessio Ansuini,<sup>1</sup> Davide Zoccolan,<sup>1</sup> Manuela Scarselli,<sup>4</sup> Maurizio De Crescenzi,<sup>4</sup> Susanna Bosi,<sup>5</sup> Maurizio Prato,<sup>5,6,7†</sup> Laura Ballerini<sup>1†</sup>

2016 © The Authors, some rights reserved; exclusive licensee American Association for the Advancement of Science. Distributed under a Creative Commons Attribution NonCommercial License 4.0 (CC BY-NC). 10.1126/sciadv.1600087

In modern neuroscience, significant progress in developing structural scaffolds integrated with the brain is provided by the increasing use of nanomaterials. We show that a multiwalled carbon nanotube self-standing framework, consisting of a three-dimensional (3D) mesh of interconnected, conductive, pure carbon nanotubes, can guide the formation of neural webs in vitro where the spontaneous regrowth of neurite bundles is molded into a dense random net. This morphology of the fiber regrowth shaped by the 3D structure supports the successful reconnection of segregated spinal cord segments. We further observed in vivo the adaptability of these 3D devices in a healthy physiological environment. Our study shows that 3D artificial scaffolds may drive local rewiring in vitro and hold great potential for the development of future in vivo interfaces.

## INTRODUCTION

Multimodal neuronal prostheses of the future will combine tissue engineering with electrical interfacing technologies to develop neurohybrid microsystems capable of improving the innate capacity of the central nervous system (CNS) to recover or rehabilitate lost functions (1–4). Despite obvious difficulties, implantable devices hold tremendous promise to overcoming the effects of CNS lesions and diseases. Nanotechnology enters this arena by developing new generations of nanomaterials to interface neuronal network formation and signaling with unprecedented abilities (5). In particular, carbon-based nanostructures, such as multiwalled carbon nanotubes (MWCNTs), have great potential for neurological applications, featuring dimensions and properties reminiscent of specific compartments of the neural machinery, and have already been shown to govern in vitro synapse formation, cell excitability, and synaptic processing (6–12). The precise biophysical mechanisms of these special interactions between MWCNTs and neurons are not completely understood (6, 7). However, the features and the remarkable applications of such materials (13), together with their ability to manipulate neural activity, hold strong promise in manufacturing interfaces enriched by artificial environmental cues that can guide tissue reconstruction. The transition from being two-dimensional (2D) to becoming 3D in such MWCNT constructs may open new horizons in treating injured CNS tissues, such as the spinal cord. In implant technology, the design of electroactive scaffolds has been exploited to support electrical interactions within neuronal cell networks and to improve guided tissue regeneration (14–16). An additional study reported that soluble functionalized carbon nanotubes may exert potential benefits when administered in the lesioned spinal cord, representing a promising substrate for scaffolding (17); however, the potential impact of pure carbon nanotubes when used as scaffolds has not been explored. Here, we test the ability of MWCNT-based 3D

structures to dictate neurite web morphology toward successful reconnection of segregated spinal explants in vitro. By confocal microscopy, we address the ability of 3D MWCNT to design the geometry of the newly formed neural nets. By means of electrophysiology, we address to what extent these 3D MWCNT-neurite structures promote the synchronization of rhythmic outputs generated by separated spinal explants. In addition, we report, for the first time, the tissue reaction and glial scar formation upon in vivo implantation of these materials.

## RESULTS AND DISCUSSION

We have previously characterized, in vitro, the ability of MWCNT 2D layers to support neuronal growth and synapse formation (6–11). To investigate the potential ability of these nanomaterials to guide CNS network reorganization in 3D, we manufactured self-standing 3D meshes of interconnected MWCNTs (Fig. 1A). These structures were interfaced in vitro with long-term, cocultured pairs of mouse organotypic spinal cord explants that allow the development of spinal networks over extended periods (18–21). Cocultured transverse slices were separated by a distance known to impair their functional reconnection under basal conditions (>300 μm) (18) and represent an efficient experimental paradigm to test the effectiveness of spontaneous regeneration of intrinsic interneuron projections (18) in recovering coherent motor outputs (22). Control slices (Controls) were grown embedded in a gelified protein-rich plasma clot (that is, fibrin glue; average distance among the two slices, 1.91 ± 0.50 mm; *n* = 40 slices), whereas those supported by the 3D carbon nanotube frame (3D CNF) were interfaced with the 3D MWCNT structures and included in the same plasma gel (average slice distance, 1.63 ± 0.42 mm; *n* = 36 slices; not significantly different from Controls, *P* = 0.08).

### 3D microsystems reconnecting segregated spinal explants

Spinal organotypic slices upon >2 weeks of culturing exhibit a characteristic outgrowth of nerve fibers (8, 21) in both groups (highlighted in Fig. 1B). We explore the patterns of growth by randomly acquiring visual fields (28 and 30 fields, *n* = 9 and *n* = 11, for Control and 3D CNF, respectively) via confocal microscopy, where β-tubulin III-positive or SMI-32-positive processes surrounding the slice explants were

<sup>1</sup>International School for Advanced Studies (SISSA/ISAS), Trieste 34136, Italy. <sup>2</sup>Department of Life Sciences, University of Trieste, Trieste 34127, Italy. <sup>3</sup>NanoInnovation Laboratory, ELETTRA Synchrotron Light Source, Trieste 34149, Italy. <sup>4</sup>Department of Physics, University of Rome Tor Vergata, Rome 00173, Italy. <sup>5</sup>Department of Chemical and Pharmaceutical Sciences, University of Trieste, Trieste 34127, Italy. <sup>6</sup>Carbon Nanobiotechnology Laboratory, CIC biomaGUNE, Paseo de Miramón 182, 20009 Donostia-San Sebastián, Spain. <sup>7</sup>Ikerbasque, Basque Foundation for Science, 48013 Bilbao, Spain. \*These authors contributed equally to this work.

†Corresponding author. Email: laura.ballerini@sisssa.it (L.B.); prato@units.it (M.P.)

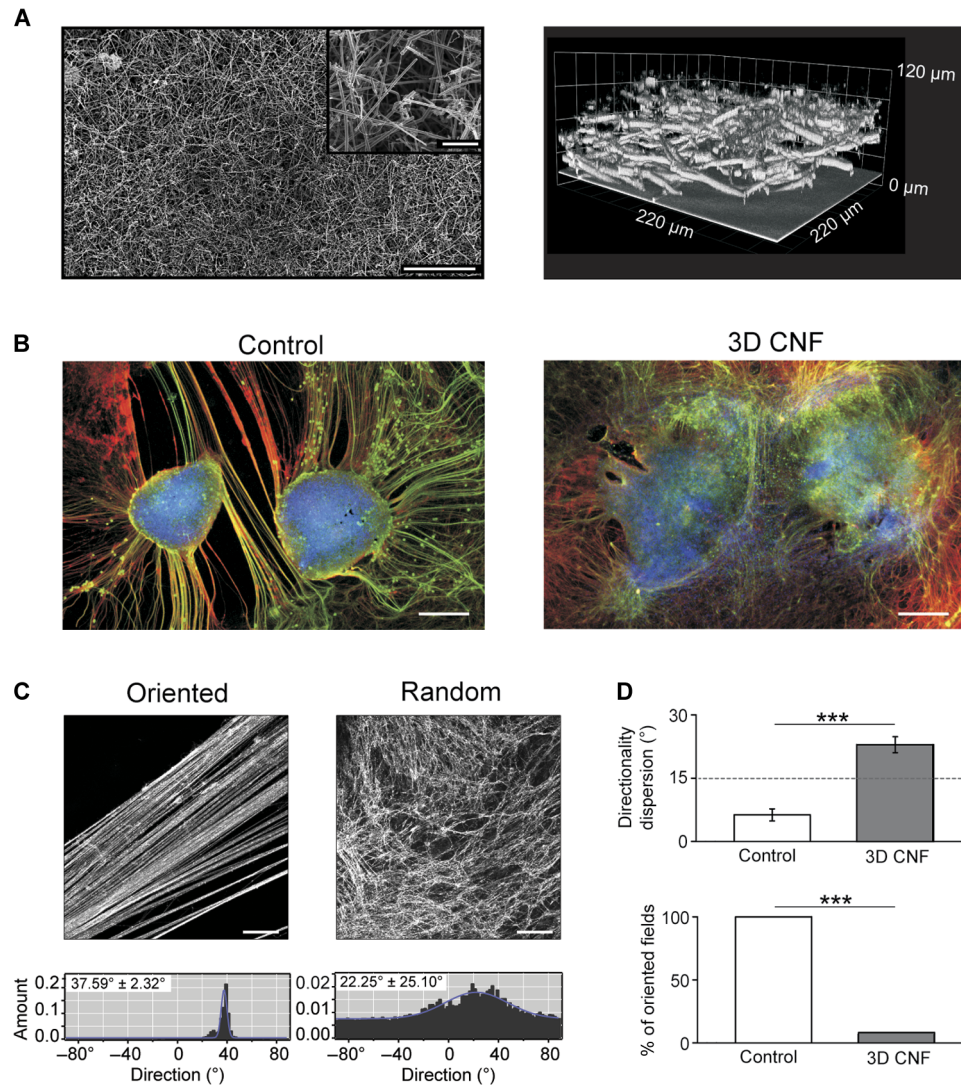


**Fig. 1. 3D CNF scaffolds redirect neurite outgrowth between spinal organotypic slices.** (A) SEM micrographs (left) of 3D CNF. At higher magnification (inset), the random skeleton of interconnected MWCNTs is shown. Confocal 3D reconstruction (right; reflection mode) of the same CNF scaffold. (B) Spinal slices cocultured in Control and in 3D CNF after 14 days of growth. Immunofluorescence is for neuron-specific microtubules ( $\beta$ -tubulin III; red), neurofilament H (SMI-32; green), and nuclei [4',6-diamidino-2-phenylindole (DAPI); blue]. (C) Confocal micrographs showing  $\beta$ -tubulin III-positive neuronal projection appearance in Control (oriented; left) and in 3D CNF (random; right) and the corresponding plots (bottom) of fiber angle direction distribution. In the example, oriented field fibers are characterized by a mean directionality value of  $37.6^\circ$  and a dispersion value of  $2.3^\circ$ , whereas random field fibers show values of  $22.3^\circ$  and  $25.1^\circ$ , respectively (values evaluated from the Gaussian fitting; see Materials and Methods). (D) Top histograms summarize the mean values of fiber orientation dispersion in Control and 3D CNF ( $***P < 0.001$ ); bottom histograms depict the percentage of visual fields in which fibers are aligned with a degree of dispersion less than  $15^\circ$ . In Controls, all samples (100%) contained oriented fibers with less than  $15^\circ$  of dispersion, whereas 7% of 3D CNF contained fibers with less than  $15^\circ$  of dispersion ( $***P < 0.001$ ). Scale bars, 250 and 25  $\mu\text{m}$  (inset) (A), 500  $\mu\text{m}$  (B), and 100  $\mu\text{m}$  (C).

visualized. In Controls, as previously reported (8), the outgrowth of neuronal projections was typically organized into thick bundles of aligned fibers [Fig. 1C (top left) and fig. S4A]. In contrast, the support of 3D CNF shaped the morphology of neurites outgrowing from the spinal explants into a complex web of randomly oriented processes [Fig. 1C (top right) and fig. S4B] invading the scaffold into the third dimension (see below). By fiber directionality analysis (23), we measured the dispersion of the mean fiber's direction in the two groups (see examples in fig. S4). Figure 1C (bottom) shows sample histograms plotting the angular distribution of the detected

structures. In these plots, the Gaussian fitting shows a narrow peak (left) in the presence of small directionality dispersion, indicating clear fiber orientation; conversely, the Gaussian fitting shows a broader distribution (right) indicating randomly oriented fibers (see Materials and Methods). Figure 1D top histograms summarize these results for Controls and 3D CNF [note the significant difference ( $P < 0.001$ ) in the directionality dispersion values]. We quantified the percentage of fields containing aligned oriented fibers, defined as fields showing mean directionality dispersion lower than  $15^\circ$  (see Materials and Methods). These results are summarized in the bar plot of Fig. 1D (bottom), which

shows that the occurrence of oriented fields was significantly reduced in 3D CNF ( $\chi^2 = 23.26$ ,  $P = 0.000001$ ; see the Supplementary Materials).

To explore whether the neuronal processes followed the third dimension of the scaffold in 3D CNF, we reconstructed 3D images from confocal Z stacks (Fig. 2A). The neurite networks emerging from spinal slices on the 3D MWCNTs are reconstructed in the confocal rendering in Fig. 2B, whereas Fig. 2C shows a scanning electron microscopy (SEM) snapshot of the hybrid web, where the MWCNT's mesh is nearly paralleled by the morphology of the neuronal fibers. We directly

compared webs of  $\beta$ -tubulin III-positive and SMI-32-positive processes from Control and 3D CNF and found that the depth of the neuronal process networks was significantly greater ( $P < 0.05$ ) with the 3D CNF, demonstrating that the neurites from the spinal slices are populating the third dimension of the nanoscaffold (for  $\beta$ -tubulin III-positive processes: Control,  $19 \pm 6 \mu\text{m}$  in  $n = 9$  visual fields; 3D CNF,  $49 \pm 33 \mu\text{m}$  in  $n = 14$  visual fields; for SMI-32-positive processes: Control,  $18 \pm 6 \mu\text{m}$  in  $n = 9$  visual fields; 3D CNF,  $38 \pm 20 \mu\text{m}$  in  $n = 14$  visual fields; Fig. 2, D and E).

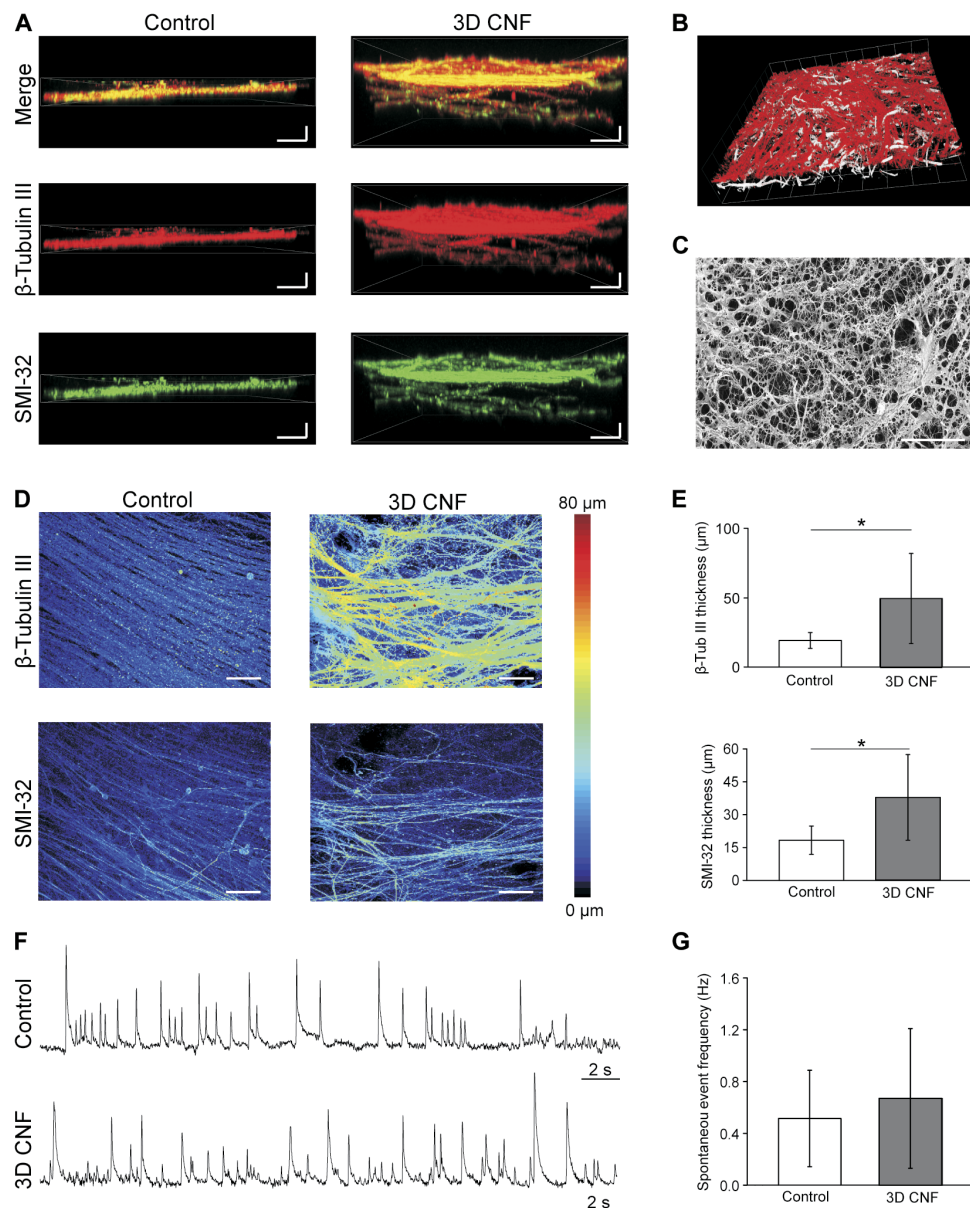


**Fig. 2. 3D CNF favors neuronal process paths in the third dimension.** (A) Detailed Z stack distribution of neuronal processes. Control neuronal processes are compared to 3D CNF ones by confocal microscopy. (B) Tilted confocal reconstruction of the intricate network of 3D CNF (white) and neuronal projections ( $\beta$ -tubulin III; red) (note the emergence of a 3D hybrid network knitted by the neuronal processes and the MWCNTs). (C) SEM micrograph of the hybrid network [same sample as in (B)]. (D) Volume rendering of the Z stacks of the neuronal processes in Control and 3D CNF samples. Neuronal processes under control conditions are relatively flat, whereas processes form a thicker layer when supported by 3D CNF. (E) Plots quantify the thicknesses of  $\beta$ -tubulin III-positive and SMI-32-positive processes ( $*P < 0.05$ , Student's t test). (F) Spontaneous LFPs recorded in Control and 3D CNF. (G) Spontaneous LFP mean frequencies. Scale bars, 25  $\mu\text{m}$  (horizontal) and 10  $\mu\text{m}$  (vertical) (A), 40  $\mu\text{m}$  (C), and 25  $\mu\text{m}$  (D).

Cultured spinal explants display prominent spontaneous electrical activity (8, 24–27). We monitored ventrally recorded extracellular potentials [local field potentials (LFPs)] to gain insights into the function of premotor circuits under the two growth conditions. Figure 2F shows sample tracings of spontaneous LFPs detected from Control and 3D CNF slices. When we analyzed 15 organotypic cocultures ( $n = 8$  Control and  $n = 7$  3D CNF; four different culture series; Fig. 2, F and G), the voltage tracings displayed similar LFP frequency ( $0.51 \pm 0.37$  and  $0.67 \pm 0.54$  Hz, respectively;  $P = 0.52$ ), confirming that 3D CNF favors the usual spinal network growth and maturation.

Simultaneous recordings of ventral LFPs were performed from the two cocultured spinal slices in both groups (sketched in Fig. 3A) to assess the presence of synchronous ventral outputs (18). To examine the functional consequences of the different patterns of projections in Control and 3D CNF ( $n = 16$  culture series), we used the glycine/ $\gamma$ -aminobutyric acid type A receptor antagonists strychnine (1  $\mu$ M) and bicuculline (20  $\mu$ M) to weaken synaptic inhibition. As previously reported for the entire spinal cord (27) and organotypic spinal slices (20, 24), the weakening of inhibition induced a switch from random bursting to synchrony, leading to the appearance of slow-paced bursting in the cocultured explants in all cultures tested (Fig. 3B, sample tracings for Control and 3D CNF). The bursting frequency, quantified as interevent interval, was similar in Control and 3D CNF ( $14.5 \pm 6.3$  and  $16.5 \pm 8.8$  s,  $n = 8$  and  $n = 14$ , respectively;  $P = 0.60$ ). The functional connectivity between the two slices was assessed by cross-correlation analysis of the disinhibited bursting. In Control, only 27% (6 of 22 pairs) of the cocultured explants were correlated, displaying a Pearson correlation coefficient (CCF) that was significantly larger than that expected by chance (see the Supplementary Materials and fig. S1), whereas the mean CCF was  $0.25 \pm 0.22$  ( $n = 22$ ; Fig. 3, C and D). In 17 Controls, stimulating (0.05 to 0.2 Hz) the dorsal region (Fig. 3, E and F) of one explant entrained the disinhibited rhythm of the same explant, but only a minority (29%; 5 of 17 pairs) succeeded in entraining (mean latency,  $118 \pm 92$  ms) the nonstimulated slice (cross-entrainment; Fig. 3G); this result did not change when the stimulation was moved to the contralateral slice. Together, these data indicate that only in a minority of Controls was there successful reconnection of the two cocultured explants, despite the huge outgrowth of fibers (8, 21).

On the contrary, in 3D CNF, the mean CCF value was  $0.56 \pm 0.27$  ( $n = 17$ ), which was significantly different from the Control (Fig. 3C;  $P < 0.001$ ), and correlated activity of disinhibited bursting between the two explants was observed in 94% of cases (16 of 17 pairs; see the Supplementary Materials and fig. S1), a fraction that was significantly larger than what was observed for the Control (Fig. 3D;  $\chi^2 = 16.56$ ,  $P < 0.001$ ). Because distance is a relevant variable (18), it is important to note that, within the range of distances analyzed, the CCF values of correlated pairs were not positively correlated ( $r = -0.271$ ,  $P = 0.31$ ) with the interslice distance variability, as reported in fig. S1D. Furthermore, when stimulating the dorsal area of one slice, cross-entrainment (mean latency,  $156 \pm 84$  ms; a value that was not significantly different from Controls,  $P = 0.448$ ) between explants was present in 10 of 13 pairs (that is, in 77% of cases; Fig. 3, F and G) and was also present when changing the stimulated slice within a given pair. In both groups, the emergence of functional coupling was unrelated to age in culture (Fig. 3H; note that blue symbols indicate functional correlated pairs measured as described in the Supplementary Materials and fig. S1).

To assess the impact of promoting 3D growth of fibers in the absence of MWCNTs, we next challenged cocultured pairs of spinal

slices with polydimethylsiloxane (PDMS)-based 3D porous structures (3D-PDMS) (28) ( $n = 5$ ; fig. S2). 3D-PDMS scaffolds are characterized by micropores of irregular shapes and dimensions interconnected with random paths of connectivity and were shown to implement 3D neurite's growth (28). In 3D-PDMS-cocultured spinal slices, the outgrowing  $\beta$ -tubulin III-positive fibers successfully infiltrated the structure in the third dimension (fig. S2A). However, 3D-PDMS samples displayed a mean value of the angular distribution of fibers (fig. S2C) and a value of the fraction of correlated pairs (fig. S2F) that were not significantly different ( $P = 0.24$  and  $P = 0.68$ , respectively) from Controls ( $n = 7$ ; fig. S2F). In a parallel approach, we tested 2D MWCNT substrates (8) to isolate the impact of MWCNTs per se in reestablishing an effective connectivity (fig. S2B;  $n = 7$ ). MWCNTs were reported to affect spinal slices (8); however, in cocultured explants, the fraction of correlated pairs did not significantly differ ( $P = 0.58$ ) from Controls (fig. S2F). Morphological analysis of the explants outgrowing fibers revealed that in 2D MWCNTs, the angular distribution displayed a significantly higher ( $P = 0.008$ ) dispersion when compared to Controls (fig. S2C). In the attempt to quantify the amount of fibers outgrowing the spinal slices under the different conditions, we measured the percentage of area of  $\beta$ -tubulin III-positive processes. As depicted in the bar plot of fig. S2D, we found a significantly increased [one-way analysis of variance (ANOVA),  $F_{3,38} = 3.99$ ,  $P = 0.015$ ]  $\beta$ -tubulin III-positive fluorescence area in 2D MWCNTs ( $P = 0.011$ ) and 3D CNF ( $P = 0.004$ ), suggesting that the high dispersion of fibers results in higher area values when slices are interfaced with 2D or 3D carbon nanotubes. We have previously reported that 2D MWCNTs improve the regrowth of neurites' bundles when interfaced with single spinal explants (8); however, it is difficult to consistently document a similar improvement in 3D CNF. The 3D regrowth implies a different volume distribution of the neurites. Ultimately, comparing thick fasciculation of processes in 2D with the outgrowth of dispersed 3D fibers in CNF renders these data inconclusive.

The morphological analysis of the four growth conditions suggests that crucial to the effects of 3D CNF is the ability of these scaffolds to guide the 3D random morphology of outgrowing neurites in the third dimension, because the improved directionality dispersion and the amount of  $\beta$ -tubulin III-positive area brought about by 2D MWCNT are insufficient to significantly improve the fraction of correlated pairs. Alternatively, the conductive scaffold may mediate a direct electrical transmission between cultured slices; however, this seems to be excluded by the entrainment testing, where we detected comparable values of latencies in stimulated coupled slices between 3D CNF and Controls. The measured latency values agree with the reported intersegmental delays in the entire spinal cord (29) and may indicate the presence of multisynaptic pathways in guiding the functional reconnection of the explanted segments. Thus, 3D CNF restores and/or reinforces the functional coupling among artificially separated spinal slices when compared to fibrin glue alone, and these effects are not reproduced by 3D-PDMS or 2D MWCNTs when tested separately. The interactions among the numerous physical, chemical, and biological factors translating the exposure to 3D MWCNTs into axonal regrowth, synapse formation, and extracellular matrix deposition along with the coculture growth in vitro are not further addressed in the current study, all of these being potential factors that could enable proper synapse formation and reconstruct functional bridges among severed networks (30). Nevertheless, it is tempting to speculate that destructuring fiber fasciculation by a 3D template of carbon nanotubes may contribute to the functional reconnection of separated spinal slices, leading to an improved synchrony of rhythmic outputs.

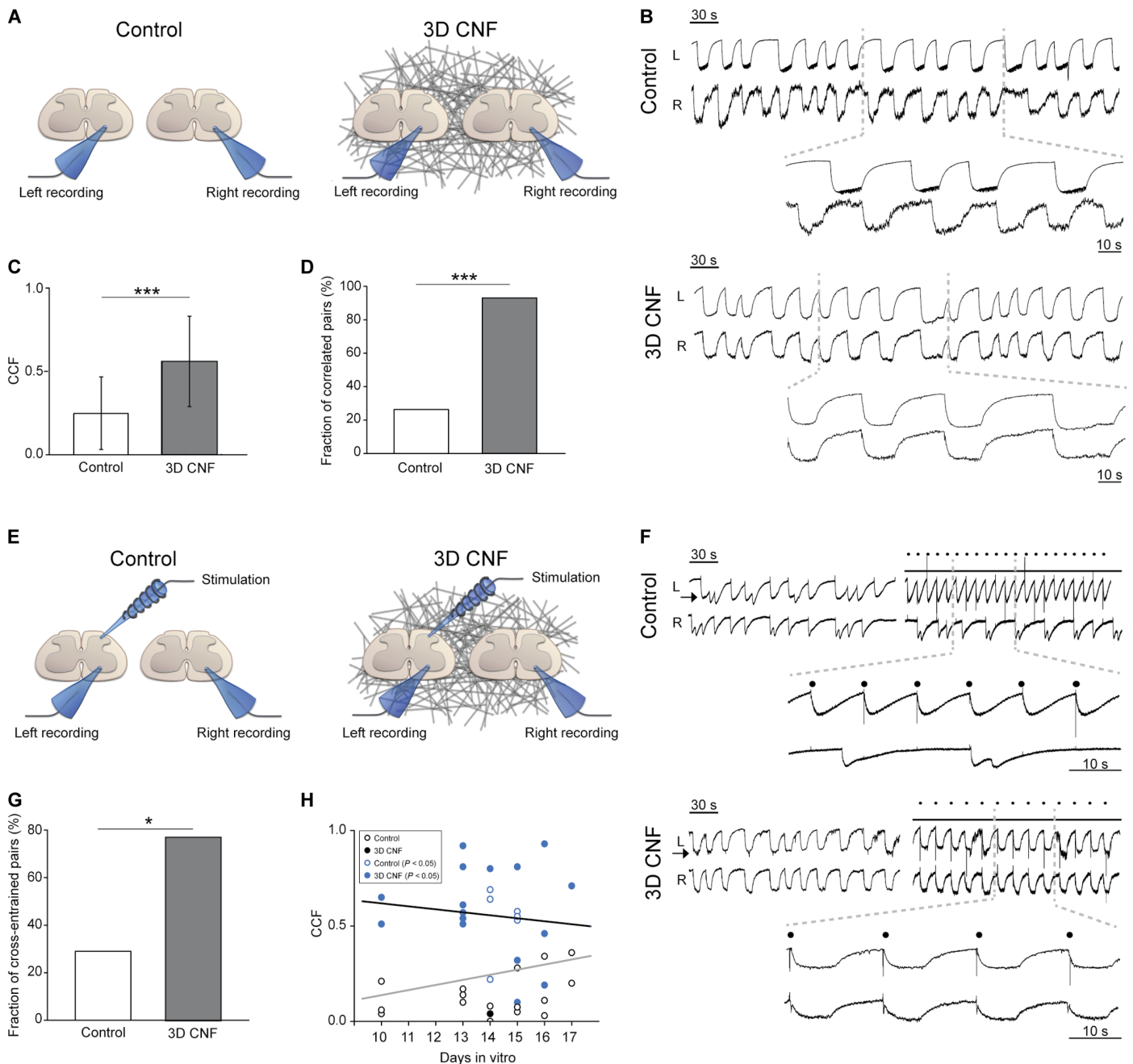


**Fig. 3. 3D CNF guides the functional reconnection of ventral outputs in segregated spinal organotypic slices.** (A) Sketch of the experimental setting for double-slice ventral recordings. (B) LFP bursting induced by strychnine and bicuculline recorded simultaneously from left (L) and right (R) slices in Control and 3D CNF. Right insets are the corresponding cross-correlation plots. (C) Average CCF from Control and 3D CNF (\*\*\*\* $P < 0.001$ ). (D) The fraction of spinal explants that were significantly correlated is significantly larger in 3D CNF (\*\*\*\* $P < 0.001$ ,  $\chi^2$  test). (E) Sketch of the experimental setting for dorsal stimulation. (F) Bursting LFP entrainment by dorsal electrical stimulation (dots) of left slices (arrow) in Control and 3D CNF slice pairs (note 3D CNF premotor output entrainment in both slices). (G) 3D CNF increases the fraction of cross-entrained explants (\* $P < 0.05$ ,  $\chi^2$  test). (H) Age in vitro is not correlated with CCF values (gray and black lines: regression lines for Control and 3D CNF conditions,  $r = 0.249$  and  $-0.113$ , respectively; blue open and filled circles highlight significant correlated pairs).

### Biocompatibility of 3D CNF implanted in vivo

In vitro 3D CNF was invaded by regrowing fibers, and we suggest that the interactions between neuronal processes and MWCNTs in the third dimension promote successful transfer of information between separated CNS explants. Although 3D CNF scaffolds appear beneficial to neuronal function in vitro, their biointeraction in vivo has never been tested. The ultimate potential of any new multifunctional device with microfeatures and nanofeatures for biomedical applications resides in its integration with the biological milieu in vivo. An assessment of the microenvironment responses to 3D CNF implants should entail evaluating the surrounding distribution patterns and the infiltration of microglia together with astrocyte aggregation at the scaffold interface (14, 31, 32). In addition, a recent report has demonstrated the ability of graphene-based implants to attract migrating neuroblasts (14). Thus, to reduce the current gap in the knowledge of 3D CNF performance in the CNS, we designed a study to observe the in vivo biocompatibility of 3D CNF. Before any larger assessment of the functional outcomes of 3D CNF was implanted into, for example, the lesioned spinal cord, we felt it pertinent to report here the performance of 3D CNF when challenged by a physiological environment. We implanted pure 3D CNF scaffolds in the brains of four adult male Wistar rats using material samples with a relatively large lateral dimension when compared to typical neuroprosthetic devices, such as electrodes (33). These scaffolds were completely implanted into the visual cortex and the animals were sacrificed at 4 weeks after implantation to assess the in vivo response to the material. We focused our experimental group at the 4-week time point, because this is the optimal time to explore the persistence of inflammatory states and glial activation [in agreement with similar studies (34–36)]. In addition, we performed an exploratory longitudinal study with five animals sacrificed at different time points to confirm tissue response progression.

Figure 4 reports the tissue reaction to the implanted scaffold. Notably, when immunolabeled for glial fibrillary acidic protein (GFAP), the GFAP fluorescence intensity profile peak in the tissue immediately surrounding the scaffold was limited, at 4 weeks, within a relatively restricted reactive area (<20  $\mu\text{m}$ ; Fig. 4, A to C) (14) when compared to other artificial implants (~60 to 100  $\mu\text{m}$ ; highlighted by the dashed line in Fig. 4A) (37, 38). Although a notable astrocytic response, the limited thickness of the GFAP-reactive region suggests that this formation may not be inhibitory to successful long-term integration of the material into the tissue (37–41). Ionized calcium-binding adapter protein 1 (Iba1)-positive microglial reactivity in the area immediately surrounding the tissue was low across all animals (Fig. 4D). Iba1-positive microglia were found to have effectively infiltrated the scaffold (Fig. 4E) but did not form a significant scar-like formation at the implant edge (Fig. 4D), and we never detected any sign of progressive cavitation usually accompanying large inflammation processes.

The tissue reaction detected is promising, suggesting implant integration with the tissue. We further investigated whether the astrocyte and microglial localization within and around the 3D CNF represented a barrier for neurons to invade the construct (42, 43). In 79% of horizontal sections tested (19 of 24 horizontal slices), we detected  $\beta$ -tubulin III-positive cells (Fig. 4G, top) progressively infiltrating the implanted 3D CNF, coexisting but never colocalizing with either Iba1-positive cells (Fig. 4G, top left) inside the structure or GFAP-positive cells located at the implant edges (not shown). We cannot exclude the fact that some  $\beta$ -tubulin III-positive processes penetrate the implant and embrace unlabeled cell somata. To clarify this issue, we used a specific neuronal

marker. Further supporting the presence of neuronal cells is the finding of neuronal nuclear antigen (NeuN)-positive cells within the scaffold (Fig. 4G, bottom). Because of the scaffold infiltration that improves stiffness before implantation (see Materials and Methods), we discount the fact that these are neurons that became trapped in the implant during insertion. These cells could be newly generated neurons migrating as a result of injury-mediated mechanisms (14, 44, 45). The presence of neuronal cells within the implant is surprising but agrees with a recent report describing migrating neuroblasts localized in implanted graphene-based scaffolds even at a certain distance from their source (14). Further studies are required to solve this issue beyond the current investigation; however, this evidence supports the notion that the immune response to the scaffold at 4 weeks does not prevent the infiltration of neuronal populations.

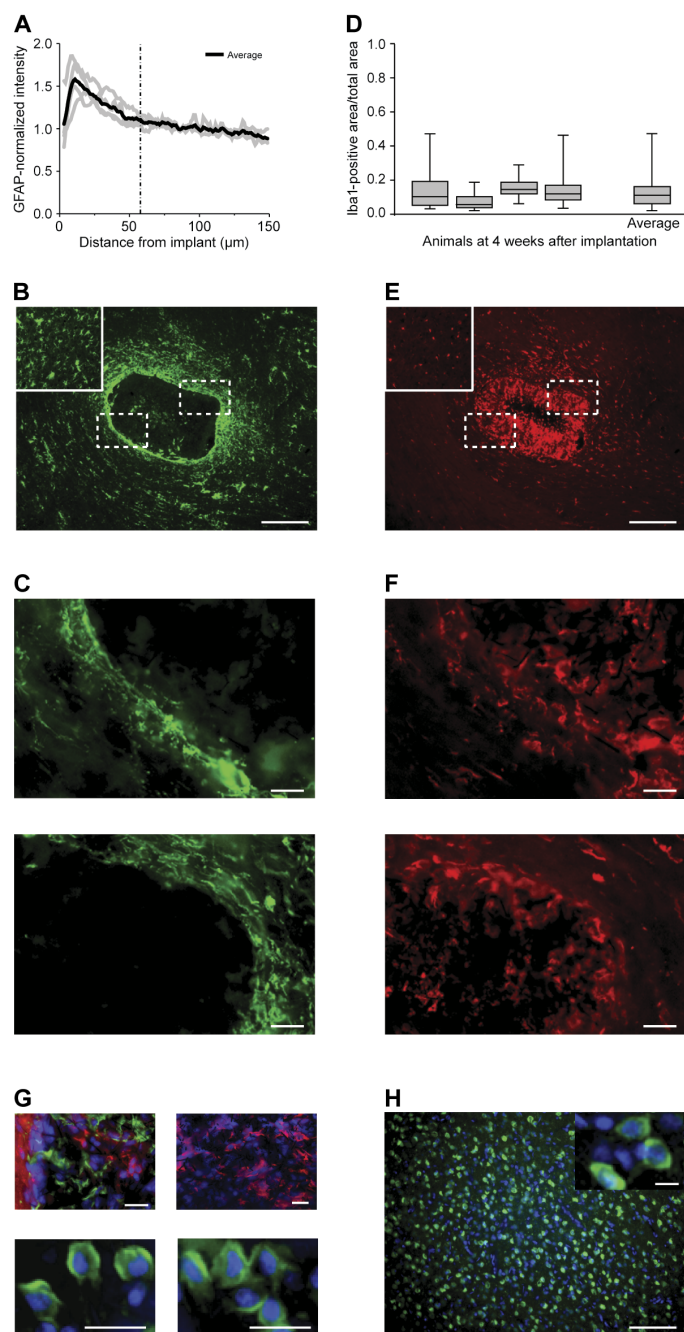
It is tempting to speculate that the presence of microglia localized inside the 3D CNF may also represent a reaction beneficial to tissue repair (14, 46, 47). Certainly, the tissue reaction to the implant is complex, but our evidence regarding scar formation and neuronal infiltration supports the hypothesis that the material is capable of integrating into the surrounding neural tissue. We observed no gross differences in tissue anatomy in other brain regions removed from the immediate implant area, including the contralateral hemisphere (insets to Fig. 4, B, E, and H).

In addition to the four animals analyzed at 4 weeks after implantation, we were interested in the tissue response over time. Thus, in an exploratory longitudinal study, we assessed the long-term immune reaction surrounding the implanted CNF scaffold over time in additional animals (each sacrificed at five different time points). The animals were sacrificed immediately following implantation (0 weeks, as an indicator of implant procedure damage) and at 1, 2, 4, and 8 weeks after implantation. After 8 weeks, the peak of the GFAP-reactive area is even smaller (<10  $\mu\text{m}$ ; fig. S5A) compared with after 4 weeks, with several areas completely devoid of GFAP reactivity. Figure S5B illustrates samples of the regions of interest (ROIs) used for analysis to demonstrate how the astrocyte reactivity in the adjacent tissue changes over time. Microglia reactivity was found to be increased at 1 week after implantation in the area immediately surrounding the 3D CNF, which is likely due to the initial inflammatory response to the compressive tissue damage induced by introducing the material itself (33, 37, 40, 41). However, 2 weeks after implantation and up until 8 weeks, the Iba1 reaction surrounding the implant progressively declined toward normal values and became sparse close to the 3D CNF (fig. S5, C and D). Although the reported longitudinal data in vivo are indeed preliminary, we suggest that, in a more complete study, adverse effects to CNS-implanted 3D CNF are likely to be limited.

Here, we tested the biointegration of implanted 3D CNF and animal survival within the time frame generally accepted in biocompatibility assessments (4 to 8 weeks) (14, 34–36, 48, 49). The general animal conditions (see the Supplementary Materials), together with the subsequent tissue histology, support the good postimplantation survival of all tested 3D CNF subjects. We observed no substantial effects of scaffold implantation on general animal behavior and/or well-being at any time point. There is no reason to suspect that the health of implanted animals beyond 8 weeks would be compromised; however, because of the well-known long-term stability in the biological milieu of carbon nanotube structures (50), the long-term survival (beyond 8 weeks) of implanted animals and the resulting implications of scaffold presence in the CNS will require additional studies. The in vivo monitoring of long-term responses to implantable neural technologies



**Fig. 4. Tissue reaction to CNF scaffolds implanted into the adult rat visual cortex.** (A) GFAP fluorescence intensity profile as a function of the distance from the edge of the implant in brain tissue. The average GFAP intensity at 4 weeks after implantation peaked at 10  $\mu\text{m}$  from the implant edge on average and gradually decreased away from the implant edge. (B) GFAP-positive cells (green) are found surrounding the implant and within the material; boxed areas indicate high-magnification images shown in (C); inset: contralateral hemisphere used as a control. (C) High magnification of GFAP reactivity at the implant edge demonstrates the minimal and irregular cellular localization around the scaffold. (D) Iba1-positive area (as a fraction of total tissue area in the ROI) varies from  $0.08 \pm 0.05$  to  $0.17 \pm 0.05$  (roughly 8 to 17% of the tissue area) at 4 weeks after implantation, with an average of  $0.13 \pm 0.08$ . (E) Iba1-positive cells (red) are dispersed consistently throughout the tissue and within the material; boxed areas indicate high-magnification images shown in (F); inset: contralateral hemisphere used as a control. (F) High-magnification images of the Iba1 reactivity demonstrate no obvious border at the implant edge to indicate scar formation. (G) Top left:  $\beta$ -Tubulin III-positive cells (red; DAPI, blue) within the scaffold and surrounded by Iba1-positive microglia (green) (note the absence of colocalization). Top right:  $\beta$ -Tubulin III-positive cells (red; DAPI, blue) within the scaffold from another animal, suggestive of the fact that neuronal process infiltration may be consistent at 4 weeks after implantation. Bottom: NeuN-positive cells (green; DAPI, blue) within the scaffold and two different areas are shown. (H) NeuN-positive cells (green; DAPI, blue) within the contralateral hemisphere; inset: high magnification of NeuN-positive cells. Scale bars, 200  $\mu\text{m}$  (B and E), 50  $\mu\text{m}$  (C and F), 20  $\mu\text{m}$  (G), and 100 and 10  $\mu\text{m}$  (inset) (H).



presents unique challenges and represents an active area of research (51). Our study identifies artificial, conductive (52) 3D CNF constructs as suitable structures to guide neuronal fiber reconstruction and signal transmission in vitro. In vivo, the low tissue reaction induced by the implantation of unmodified MWCNT microsystems provides a crucial factor to the further design of miniaturized platforms based on entirely new materials and concepts toward functionally integrated interfaces (1–4). Understanding the potential of nanomaterial-based conductive scaffolds may promote the design of novel interventions (14, 53) where the scaffold in itself is critical to the success of the implant.

## MATERIALS AND METHODS

### 3D CNFs, PDMS scaffolds, and 2D MWCNTs

3D CNFs were obtained from the laboratory of M.D.C. as previously reported (52, 54, 55) (see the Supplementary Materials for details). The bulky 3D scaffolds were cut into thin square slices (lateral size, 3 mm  $\times$  4 mm; thickness, 250 to 400  $\mu\text{m}$ ) and then secured on standard glass coverslips (Kindler) by PDMS (Sylgard 184 silicone elastomer, Dow Corning) cured at 150°C for 15 min. Thereafter, substrates were cleaned under low-pressure air plasma for 5 min (PDC-32G Plasma Cleaner, Harrick Plasma) and ultraviolet (UV)–sterilized for 20 min before use.

PDMS scaffolds are 3D, self-standing, porous microsponges fabricated as described by Bosi *et al.* (28). 2D MWCNT supports were obtained as previously described by Fabbro *et al.* (8).

### Organotypic spinal explant preparation

Organotypic cultures were obtained from spinal cords of E12 embryonic mouse (C57BL) as previously reported (8, 21, 26) (see the Supplementary Materials for details). To ensure homogeneous experimental conditions between the two analyzed populations (Control and 3D CNF double-cultured spinal slice pairs), pairs of organotypic spinal explants with interslice distance (measured between the center of the two explants by

bright-field imaging) exceeding the 0.8- to 2.5-mm range were discarded for electrophysiological and immunofluorescence experiments.

### Electrophysiological recordings

All electrophysiological experiments were performed at room temperature as previously described (8, 20, 21). The synchrony between the bursting activities of the two explants in each pair was assessed by computing the Pearson CCF between the two voltage time series (see the Supplementary Materials for details).

## Immunofluorescence labeling and confocal imaging of spinal slice explants

Images of labeled organotypic cultures were acquired using a Nikon C2 or a Leica DMIRE2 confocal microscope, both equipped with argon/krypton, helium/neon, and UV lasers. Images were acquired with a 20×, 40×, or 63× oil objective (numerical aperture, 1.4) using oil-mounting medium (1.515 refractive index). Analysis and 3D reconstruction of the image Z stack were accomplished using NIS-Elements AR (Nikon), Volocity (PerkinElmer), and Fiji (<http://fiji.sc/Fiji>) software.

To measure the alignment of outgrowing fibers, we quantified their relative orientation based on fiber directionality analysis (23): When the dispersion of the mean fiber's direction was lower than 15°, we defined them as "oriented," whereas when it was higher than 15°, we defined them as "random." Briefly, the mean fiber's direction and relative dispersion were computed from 640 μm × 640 μm confocal images (12 and 15 randomly sampled images,  $n = 4$  and  $n = 5$ , for Control and 3D CNF, respectively) where neuronal processes were visualized by β-tubulin III immunofluorescence (fig. S4). The analysis was carried out using the Directionality plugin of Fiji software inferring the preferred orientation of "structures" present in the input image. Fiber orientation was calculated via a Fourier component analysis (23).

A histogram that indicates the amount of structures displaying a given direction was computed, and a Gaussian fitting was applied (see Fig. 1C and fig. S4). Images with a completely isotropic content will result into a flat histogram, leading to a high dispersion value of the Gaussian fitting, whereas images with a clear alignment (for example, bundles of fibers with preferred orientations) will present a narrow peak at that orientation in the relative histogram and will be characterized by a smaller dispersion value. The dispersion value is the SD of the Gaussian fit (see the Supplementary Materials for additional details on image analysis).

## Brain tissue implantation with 3D CNF

All surgical procedures were performed on anesthetized male Wistar rats (Harlan Laboratories;  $n = 9$ ) aged 3 to 6 months and weighing 450 to 550 g. The implant consisted of a sharp-pointed cylinder (~2 mm in length and  $0.5 \pm 0.2$  mm in diameter) carved out of a larger 3D CNF scaffold and mounted on an electrode holder (ZIF-Clip, Tucker-Davis Technologies). Implant stiffness was increased via polyethylene glycol (PEG) scaffold permeation before the carving procedure to facilitate the insertion of the material into the brain tissue. The PEG-stiffened 3D CNF scaffold was inserted into the visual cortex. For the study of biocompatibility (data reported in Fig. 4),  $n = 4$  animals were sacrificed at 4 weeks after implantation. For the exploratory longitudinal study aimed at investigating the response over time,  $n = 5$  animals were sacrificed at 0, 1, 2, 4, and 8 weeks after implantation (data reported in fig. S5; see the Supplementary Materials for details).

## Brain tissue preparation, immunohistochemistry, image acquisition, and analysis

Animals were anesthetized with chloral hydrate and then sacrificed via transcardial perfusion with 0.1 M phosphate-buffered saline (PBS) followed by 4% formaldehyde (prepared from fresh paraformaldehyde) in PBS. Brains were removed, postfixed, embedded in optimal cutting temperature compound (Tissue-Tek), and cryosectioned horizontally as 25-μm-thick sections. After immunohistochemistry, sections were mounted on glass coverslips using Vectashield Hard Mounting Medium (Vector Laboratories). We measured the brain tissue reaction at 4 weeks after implantation using GFAP for astrocytes and Iba1 for microglia.

We also labeled the tissue sections for neurons using β-tubulin III and a marker for NeuN. At 4 weeks after implantation, the mean-normalized GFAP intensity in the region up to 150 μm from the edge of the implant was  $1.11 \pm 0.19$ , with an average peak of fluorescence intensity (as an indicator of the maximum localization of GFAP-positive astrocytes) of 25 μm from the implant edge. In the four animals at this time point, this peak ranged from 8 to 16 μm from the edge of the implant, which is a relatively tight window. As a fraction of the total tissue area, normalized to the reactivity in the contralateral hemisphere, the average Iba1-reactive area for these animals was  $0.13 \pm 0.08$ . This indicates that, on average, about 13% of the total tissue area within 500 μm surrounding the implant was composed of Iba1-positive microglia (see the Supplementary Materials for details).

## Scanning electron microscopy

3D CNF morphology before and after culturing was qualitatively assessed through SEM. Images were acquired through collecting secondary electrons on a Gemini SUPRA 40 SEM (Carl Zeiss NTS GmbH). Before imaging, samples were gold-metalized on a metal sputter coater.

## Mechanical characterization

The mechanical properties of 3D CNF scaffolds were evaluated via uniaxial microcompression tests conducted on a Galdabini SUN 500 apparatus. Tests were performed in air at room temperature. Elastic data were determined by calculating the initial linear slope of the stress-strain curve (see the Supplementary Materials for details).

## Statistics

All values from samples subjected to the same experimental protocols were pooled together and expressed as means  $\pm$  SD, with  $n$  being the number of cultures, unless otherwise specified. Where not otherwise indicated, statistically significant differences between data sets were assessed by Student's  $t$  test (after validation of variance homogeneity by Levene's test) for parametric data and by the Mann-Whitney  $U$  test for nonparametric data. For estimating significantly synchronous slices in the two groups and for the percentage of oriented fields, we performed a homogeneity test with the  $\chi^2$  method. One-way ANOVA was used to determine significance when multiple groups were compared (for example, directionality dispersion), and Fisher's least significant difference was used to determine significance post hoc. Statistical significance was determined at  $P < 0.05$ .

## Ethical statement

All animal procedures were conducted in accordance with the National Institutes of Health and with international and institutional standards for the care and use of animals in research, and after consulting with a veterinarian. All experiments were performed in accordance with European Union (EU) guidelines (2010/63/UE) and Italian law (decree 26/14) and were approved by the local authority veterinary service and by our institutional (SISSA-ISAS) ethical committee. All efforts to minimize animal suffering and to reduce the number of animals used were made. Animal use was approved by the Italian Ministry of Health, in agreement with the EU Recommendation 2007/526/CE ([http://eur-lex.europa.eu/legal-content/EN/TXT/?uri=uriserv:OJ.L\\_.2007.197.01.0001.01.ENG&toc=OJ.L:2007:197:TOC](http://eur-lex.europa.eu/legal-content/EN/TXT/?uri=uriserv:OJ.L_.2007.197.01.0001.01.ENG&toc=OJ.L:2007:197:TOC)).

## SUPPLEMENTARY MATERIALS

Supplementary material for this article is available at <http://advances.sciencemag.org/cgi/content/full/2/7/e1600087/DC1>

Supplementary Materials and Methods

fig. S1. Illustration of the permutation test to assess the statistical significance of the synchrony between the bursting activities of two cocultured explants.

fig. S2. Organotypic spinal slices cultured on 2D MWCNT substrates and on 3D-PDMS scaffolds.

fig. S3. Extracellular voltage transients represent evoked or spontaneous synaptic, action potential-mediated activity.

fig. S4. Directionality analysis of spinal neuronal process outgrowth.

fig. S5. Immune reaction over time to CNF scaffolds implanted into the adult rat visual cortex as a pilot study.

References (56–61)

## REFERENCES AND NOTES

- B. Tian, J. Liu, T. Dvir, L. Jin, J. H. Tsui, Q. Qing, Z. Suo, R. Langer, D. S. Kohane, C. M. Lieber, Macroporous nanowire nanoelectronic scaffolds for synthetic tissues. *Nat. Mater.* **11**, 986–994 (2012).
- D. K. Cullen, J. A. Wolf, D. H. Smith, B. J. Pfister, Neural tissue engineering for neuroregeneration and biohybridized interface microsystems in vivo (part 2). *Crit. Rev. Biomed. Eng.* **39**, 241–259 (2011).
- J. L. Collinger, S. Foldes, T. M. Bruns, B. Wodlinger, R. Gaunt, D. J. Weber, Neuroprosthetic technology for individuals with spinal cord injury. *J. Spinal Cord Med.* **36**, 258–272 (2013).
- A. Jackson, J. B. Zimmermann, Neural interfaces for the brain and spinal cord—Restoring motor function. *Nat. Rev. Neurol.* **8**, 690–699 (2012).
- N. A. Kotov, J. O. Winter, I. P. Clements, E. Jan, B. P. Timko, S. Campidelli, S. Pathak, A. Mazzatenta, C. M. Lieber, M. Prato, R. V. Bellamkonda, G. A. Silva, N. W. S. Kam, F. Patolsky, L. Ballerini, Nanomaterials for neural interfaces. *Adv. Mater.* **21**, 3970–4004 (2009).
- G. Cellot, E. Cilia, S. Cipollone, V. Rancic, A. Sucupane, S. Giordani, L. Gambazzi, H. Markram, M. Grandolfo, D. Scaini, F. Gelain, L. Casalis, M. Prato, M. Giugliano, L. Ballerini, Carbon nanotubes might improve neuronal performance by favouring electrical shortcuts. *Nat. Nanotechnol.* **4**, 126–133 (2009).
- G. Cellot, F. M. Toma, Z. K. Varley, J. Laishram, A. Villari, M. Quintana, S. Cipollone, M. Prato, L. Ballerini, Carbon nanotube scaffolds tune synaptic strength in cultured neural circuits: Novel frontiers in nanomaterial–tissue interactions. *J. Neurosci.* **31**, 12945–12953 (2011).
- A. Fabbro, A. Villari, J. Laishram, D. Scaini, F. M. Toma, A. Turco, M. Prato, L. Ballerini, Spinal cord explants use carbon nanotube interfaces to enhance neurite outgrowth and to fortify synaptic inputs. *ACS Nano* **6**, 2041–2055 (2012).
- A. Fabbro, M. Prato, L. Ballerini, Carbon nanotubes in neuroregeneration and repair. *Adv. Drug Deliv. Rev.* **65**, 2034–2044 (2013).
- V. Lovat, D. Pantarotto, L. Lagostena, B. Cacciari, M. Grandolfo, M. Righi, G. Spalluto, M. Prato, L. Ballerini, Carbon nanotube substrates boost neuronal electrical signaling. *Nano Lett.* **5**, 1107–1110 (2005).
- A. Mazzatenta, M. Giugliano, S. Campidelli, L. Gambazzi, L. Businaro, H. Markram, M. Prato, L. Ballerini, Interfacing neurons with carbon nanotubes: Electrical signal transfer and synaptic stimulation in cultured brain circuits. *J. Neurosci.* **27**, 6931–6936 (2007).
- H. Hu, Y. Ni, V. Montana, R. C. Haddon, V. Pargura, Chemically functionalized carbon nanotubes as substrates for neuronal growth. *Nano Lett.* **4**, 507–511 (2004).
- M. F. L. De Volder, S. H. Tawfik, R. H. Baughman, A. J. Hart, Carbon nanotubes: Present and future commercial applications. *Science* **339**, 535–539 (2013).
- K. Zhou, S. Motamed, G. A. Thouas, C. C. Bernard, D. Li, H. C. Parkinson, H. A. Coleman, D. I. Finkelstein, J. S. Forsythe, Graphene functionalized scaffolds reduce the inflammatory response and supports endogenous neuroblast migration when implanted in the adult brain. *PLoS One* **11**, e0151589 (2016).
- B. Zhu, S.-C. Luo, H. Zhao, H.-A. Lin, J. Sekine, A. Nakao, C. Chen, Y. Yamashita, H.-h. Yu, Large enhancement in neurite outgrowth on a cell membrane-mimicking conducting polymer. *Nat. Commun.* **5**, 4523 (2014).
- T. Dvir, B. P. Timko, D. S. Kohane, R. Langer, Nanotechnological strategies for engineering complex tissues. *Nat. Nanotechnol.* **6**, 13–22 (2011).
- J. A. Roman, T. L. Niedzielko, R. C. Haddon, V. Pargura, C. L. Floyd, Single-walled carbon nanotubes chemically functionalized with polyethylene glycol promote tissue repair in a rat model of spinal cord injury. *J. Neurotrauma* **28**, 2349–2362 (2011).
- M. Heidemann, J. Streit, A. Tschertcher, Functional regeneration of intraspinal connections in a new in vitro model. *Neuroscience* **262**, 40–52 (2014).
- J. Gerardo-Nava, D. Hodde, I. Katona, A. Bozkurt, T. Grehl, H. W. M. Steinbusch, J. Weis, G. A. Brook, Spinal cord organotypic slice cultures for the study of regenerating motor axon interactions with 3D scaffolds. *Biomaterials* **35**, 4288–4296 (2014).
- L. Ballerini, M. Galante, M. Grandolfo, A. Nistri, Generation of rhythmic patterns of activity by ventral interneurons in rat organotypic spinal slice culture. *J. Physiol.* **517**, 459–475 (1999).
- D. Avossa, M. D. Rosato-Siri, F. Mazzarol, L. Ballerini, Spinal circuits formation: A study of developmentally regulated markers in organotypic cultures of embryonic mouse spinal cord. *Neuroscience* **122**, 391–405 (2003).
- G. Courtine, B. Song, R. R. Roy, H. Zhong, J. E. Herrmann, Y. Ao, J. Qi, V. R. Edgerton, M. V. Sofroniew, Recovery of supraspinal control of stepping via indirect propriospinal relay connections after spinal cord injury. *Nat. Med.* **14**, 69–74 (2008).
- Z. Q. Liu, Scale space approach to directional analysis of images. *Appl. Opt.* **30**, 1369–1373 (1991).
- J. Streit, Regular oscillations of synaptic activity in spinal networks in vitro. *J. Neurophysiol.* **70**, 871–878 (1993).
- M. Galante, A. Nistri, L. Ballerini, Opposite changes in synaptic activity of organotypic rat spinal cord cultures after chronic block of AMPA/kainate or glycine and GABA<sub>A</sub> receptors. *J. Physiol.* **523**, 639–651 (2000).
- F. Furlan, G. Taccola, M. Grandolfo, L. Guasti, A. Arcangeli, A. Nistri, L. Ballerini, ERG conductance expression modulates the excitability of ventral horn GABAergic interneurons that control rhythmic oscillations in the developing mouse spinal cord. *J. Neurosci.* **27**, 919–928 (2007).
- E. Bracci, L. Ballerini, A. Nistri, Localization of rhythmogenic networks responsible for spontaneous bursts induced by strychnine and bicuculline in the rat isolated spinal cord. *J. Neurosci.* **16**, 7063–7076 (1996).
- S. Bosi, R. Rauti, J. Laishram, A. Turco, D. Lonardoni, T. Nieuw, M. Prato, D. Scaini, L. Ballerini, From 2D to 3D: Novel nanostructured scaffolds to investigate signaling in reconstructed neuronal networks. *Sci. Rep.* **5**, 9562 (2015).
- E. Bracci, M. Beato, A. Nistri, Afferent inputs modulate the activity of a rhythmic burst generator in the rat disinhibited spinal cord in vitro. *J. Neurophysiol.* **77**, 3157–3167 (1997).
- M. M. Stevens, J. H. George, Exploring and engineering the cell surface interface. *Science* **310**, 1135–1138 (2005).
- E. R. Aurand, J. Wagner, C. Lanning, K. B. Bjugstad, Building biocompatible hydrogels for tissue engineering of the brain and spinal cord. *J. Funct. Biomater.* **3**, 839–863 (2012).
- E. Fournier, C. Passirani, C. N. Montero-Menei, J. P. Benoit, Biocompatibility of implantable synthetic polymeric drug carriers: Focus on brain biocompatibility. *Biomaterials* **24**, 3311–3331 (2003).
- J. Thelin, H. Jörentell, E. Psouni, M. Garwicz, J. Schouenborg, N. Danielsen, C. E. Linsmeier, Implant size and fixation mode strongly influence tissue reactions in the CNS. *PLoS One* **6**, e16267 (2011).
- R. Biran, M. D. Noble, P. A. Tresco, Directed nerve outgrowth is enhanced by engineered glial substrates. *Exp. Neurol.* **184**, 141–152 (2003).
- J. P. Seymour, D. R. Kipke, Neural probe design for reduced tissue encapsulation in CNS. *Biomaterials* **28**, 3594–3607 (2007).
- J. N. Turner, W. Shain, D. H. Szarowski, M. Andersen, S. Martins, M. Isaacson, H. Craighead, Cerebral astrocyte response to micromachined silicon implants. *Exp. Neurol.* **156**, 33–49 (1999).
- Y. Zhong, R. V. Bellamkonda, Dexamethasone-coated neural probes elicit attenuated inflammatory response and neuronal loss compared to uncoated neural probes. *Brain Res.* **1148**, 15–27 (2007).
- B. D. Winslow, M. B. Christensen, W.-K. Yang, F. Solzbacher, P. A. Tresco, A comparison of the tissue response to chronically implanted Parylene-C-coated and uncoated planar silicon microelectrode arrays in rat cortex. *Biomaterials* **31**, 9163–9172 (2010).
- W. He, G. C. McConnell, R. V. Bellamkonda, Nanoscale laminin coating modulates cortical scarring response around implanted silicon microelectrode arrays. *J. Neural Eng.* **3**, 316–326 (2006).
- G. Lind, C. E. Lindmeier, J. Schouenborg, The density difference between tissue and neural probes is a key factor for glial scarring. *Sci. Rep.* **3**, 2942 (2013).
- Y.-T. Kim, R. W. Hitchcock, M. J. Bridge, P. A. Tresco, Chronic response of adult rat brain tissue to implants anchored to the skull. *Biomaterials* **25**, 2229–2237 (2004).
- C. J. Rivet, K. Zhou, R. J. Gilbert, D. I. Finkelstein, J. S. Forsythe, Cell infiltration into a 3D electrospun fiber and hydrogel hybrid scaffold implanted in the brain. *Biomatter* **5**, e1005527 (2015).
- D. R. Nisbet, A. E. Rodda, M. K. Horne, J. S. Forsythe, D. I. Finkelstein, Neurite infiltration and cellular response to electrospun polycaprolactone scaffolds implanted into the brain. *Biomaterials* **30**, 4573–4580 (2009).
- H. T. Ghashghaei, C. Lai, E. S. Anton, Neuronal migration in the adult brain: Are we there yet? *Nat. Rev. Neurosci.* **8**, 141–151 (2007).
- A. M. Osman, M. J. Porritt, M. Nilsson, H. G. Kuhn, Long-term stimulation of neural progenitor cell migration after cortical ischemia in mice. *Stroke* **42**, 3559–3565 (2011).
- H. Neumann, M. R. Kotter, R. J. M. Franklin, Debris clearance by microglia: An essential link between degeneration and regeneration. *Brain* **132**, 288–295 (2009).
- U.-K. Hanisch, H. Kettenmann, Microglia: Active sensor and versatile effector cells in the normal and pathologic brain. *Nat. Neurosci.* **10**, 1387–1394 (2007).
- I. R. Mineev, P. Musienko, A. Hirsch, Q. Barraud, N. Wenger, E. M. Moraud, J. Gandar, M. Capogrosso, T. Milekovic, L. Asboth, R. F. Torres, N. Vachicouras, Q. Liu, N. Pavlova,

- S. Duis, A. Larmagnac, J. Vörös, S. Micera, Z. Suo, G. Courtine, S. P. Lacour, Biomaterials. Electronic dura mater for long-term multimodal neural interfaces. *Science* **347**, 159–163 (2015).
49. S. De Faveri, E. Maggolini, E. Miele, F. De Angelis, F. Cesca, F. Benfenati, L. Fadiga, Bio-inspired hybrid microelectrodes: A hybrid solution to improve long-term performance of chronic intracortical implants. *Front. Neuroeng.* **7**, 7 (2014).
50. A. Nunes, C. Bussy, L. Gherardini, M. Meneghetti, M. A. Herrero, A. Bianco, M. Prato, T. Pizzorusso, K. T. Al-Jamal, K. Kostarelos, In vivo degradation of functionalized carbon nanotubes after stereotactic administration in the brain cortex. *Nanomedicine* **7**, 1485–1494 (2012).
51. T. D. Y. Kozai, J. R. Eles, A. L. Vazquez, X. T. Cui, Two-photon imaging of chronically implanted neural electrodes: Sealing methods and new insights. *J. Neurosci. Methods* **258**, 46–55 (2016).
52. L. Camilli, C. Pisani, M. Passacantando, V. Grossi, M. Scarselli, P. Castrucci, M. De Crescenzi, Pressure-dependent electrical conductivity of freestanding three-dimensional carbon nanotube network. *Appl. Phys. Lett.* **102**, 183117 (2013).
53. M. E. Spira, A. Hai, Multi-electrode array technologies for neuroscience and cardiology. *Nat. Nanotechnol.* **8**, 83–94 (2013).
54. L. Camilli, C. Pisani, E. Gautron, M. Scarselli, P. Castrucci, F. D'Orazio, M. Passacantando, D. Moscone, M. De Crescenzi, A three-dimensional carbon nanotube network for water treatment. *Nanotechnology* **25**, 065071 (2014).
55. X. Gui, J. Wei, K. Wang, A. Cao, H. Zhu, Y. Jia, Q. Shu, D. Wu, Carbon nanotube sponges. *Adv. Mater.* **22**, 617–621 (2010).
56. W. J. Tyler, The mechanobiology of brain function. *Nat. Rev. Neurosci.* **13**, 867–878 (2012).
57. A. Tschertter, M. O. Heuschkel, P. Renaud, J. Streit, Spatiotemporal characterization of rhythmic activity in rat spinal cord slice cultures. *Eur. J. Neurosci.* **14**, 179–190 (2001).
58. M. D. Rosato-Siri, D. Zoccolan, F. Furlan, L. Ballerini, Interneurone bursts are spontaneously associated with muscle contractions only during early phases of mouse spinal network development: A study in organotypic cultures. *Eur. J. Neurosci.* **20**, 2697–2710 (2004).
59. K. B. Bjugstad, K. Lampe, D. S. Kern, M. Mahoney, Biocompatibility of poly(ethylene glycol)-based hydrogels in the brain: An analysis of the glial response across space and time. *J. Biomed. Mater. Res. A* **95**, 79–91 (2010).
60. K. B. Bjugstad, D. E. Redmond Jr., K. J. Lampe, D. S. Kern, J. R. Sladek Jr., M. J. Mahoney, Biocompatibility of PEG-based hydrogels in primate brain. *Cell Transplant.* **17**, 409–415 (2008).
61. G. Paxinos, C. Watson, *The Rat Brain in Stereotaxic Coordinates* (Elsevier Academic Press, San Diego, 2005).

**Acknowledgments:** We are grateful to M. Gandolfo and D. Cojoc for supervising the confocal image analysis and reconstruction, G. Turco for characterizing the material compressibility, and L. Camilli for the pioneering work on the growth of MWCNT networks. Istituto Officina dei Materiali – Tecnologie Avanzate e Nano Scienza (Trieste) is also acknowledged for SEM assistance. **Funding:** We acknowledge financial support from EOARD no. FA9550-14-1-0047 to M.D.C. and NEUROSCAFFOLDS-FP7-NMP-604263, CARBONANOBIDGE-ERC-2008-227135, and PRIN-MIUR no. 2012MYESZW to M.P. and L.B. **Author contributions:** S.U. and A.F. performed electrophysiology, immunofluorescence, confocal experiments, and all experimental analysis on slice cultures; M.M. and E.R.A. designed and performed histology, immunofluorescence confocal microscopy, and analysis on brain sections; J.L. performed immunofluorescence confocal microscopy; F.B.R. and D.Z. designed and performed the neurosurgery experiments; A.A. and D.Z. designed and implemented the statistical analysis to assess the synchrony of the bursting activity; D.S. designed the experiments, designed and contributed to the experimental analysis of data, and performed material preparation, measurements, and SEM; M.S. and M.D.C. provided the material; S.B. contributed to material analysis and preparation; M.P. and L.B. conceived the study and provided funding; L.B. designed the experiments and designed and contributed to the analysis of data; and E.R.A. and L.B. wrote the article. All authors discussed the results and commented on the article. **Competing interests:** The authors declare that they have no competing interests. **Data and materials availability:** All data needed to evaluate the conclusions in the paper are present in the paper and/or the Supplementary Materials. Additional data related to this paper may be requested from the authors.

Submitted 18 January 2016

Accepted 22 June 2016

Published 15 July 2016

10.1126/sciadv.1600087

**Citation:** S. Usmani, E. R. Aurand, M. Medelin, A. Fabbro, D. Scaini, J. Laishram, F. B. Rosselli, A. Ansuini, D. Zoccolan, M. Scarselli, M. De Crescenzi, S. Bosi, M. Prato, L. Ballerini, 3D meshes of carbon nanotubes guide functional reconnection of segregated spinal explants. *Sci. Adv.* **2**, e1600087 (2016).

This article is published under a Creative Commons license. The specific license under which this article is published is noted on the first page.

For articles published under [CC BY](#) licenses, you may freely distribute, adapt, or reuse the article, including for commercial purposes, provided you give proper attribution.

For articles published under [CC BY-NC](#) licenses, you may distribute, adapt, or reuse the article for non-commercial purposes. Commercial use requires prior permission from the American Association for the Advancement of Science (AAAS). You may request permission by clicking [here](#).

***The following resources related to this article are available online at <http://advances.sciencemag.org>. (This information is current as of July 22, 2016):***

**Updated information and services**, including high-resolution figures, can be found in the online version of this article at:

<http://advances.sciencemag.org/content/2/7/e1600087.full>

**Supporting Online Material** can be found at:

<http://advances.sciencemag.org/content/suppl/2016/07/11/2.7.e1600087.DC1>

This article **cites 60 articles**, 11 of which you can access for free at:

<http://advances.sciencemag.org/content/2/7/e1600087#BIBL>

*Science Advances* (ISSN 2375-2548) publishes new articles weekly. The journal is published by the American Association for the Advancement of Science (AAAS), 1200 New York Avenue NW, Washington, DC 20005. Copyright is held by the Authors unless stated otherwise. AAAS is the exclusive licensee. The title *Science Advances* is a registered trademark of AAAS

## Supplementary Materials for

### **3D meshes of carbon nanotubes guide functional reconnection of segregated spinal explants**

Sadaf Usmani, Emily Rose Aurand, Manuela Medelin, Alessandra Fabbro, Denis Scaini, Jummi Laishram, Federica B. Rosselli, Alessio Ansuini, Davide Zoccolan, Manuela Scarselli, Maurizio De Crescenzi, Susanna Bosi, Maurizio Prato, Laura Ballerini

Published 15 July 2016, *Sci. Adv.* **2**, e1600087 (2016)

DOI: 10.1126/sciadv.1600087

#### **This PDF file includes:**

- Supplementary Materials and Methods
- fig. S1. Illustration of the permutation test to assess the statistical significance of the synchrony between the bursting activities of two cocultured explants.
- fig. S2. Organotypic spinal slices cultured on 2D MWCNT substrates and on 3D-PDMS scaffolds.
- fig. S3. Extracellular voltage transients represent evoked or spontaneous synaptic, action potential-mediated activity.
- fig. S4. Directionality analysis of spinal neuronal process outgrowth.
- fig. S5. Immune reaction over time to CNF scaffolds implanted into the adult rat visual cortex as a pilot study.
- References (56–61)

## Supplementary Materials

### Supplementary Materials and Methods

#### *Carbon nanotubes three-dimensional frame and spinal cord organotypic culture preparation*

Carbon nanotube three-dimensional frames (3D CNF) were obtained from Prof. Maurizio De Crescenzi's laboratory (52). As previously reported (52, 54, 55), manufactured carbon nanotube freestanding frameworks were three-dimensional meshes of self-assembled, interconnected large multi-walled carbon nanotubes (MWCNT). MWCNTs were up to 0.4  $\mu\text{m}$  in diameter and up to hundreds of  $\mu\text{m}$  in length, 3D CNF were obtained by chemical vapor deposition (CVD) as described in previous works (52, 54, 55). 3D CNFs were characterized by a bulky stiffness, measured by a compressive load cell, of about 5 kPa, a value within the range of the reported tissue stiffness for rodent and human brains (from 0.1 to 20 kPa) (56). 3D CNFs also displayed high electrical conductivity (52). The bulky 3D scaffolds were cut into thin square slices (3 mm  $\times$  4 mm lateral size; 250–400  $\mu\text{m}$  thickness) and then secured on standard glass coverslips (Kindler) by PDMS (Sylgard® 184 silicone elastomer, Dow-Corning, US) cured at 150°C for 15 minutes. Thereafter substrates were cleaned under low-pressure air plasma for 5 minutes (PDC-32G Plasma Cleaner, Harrick Plasma) and UV sterilized for 20 minutes before use.

Organotypic cultures were obtained from spinal cords of E12 embryonic mouse (C57Bl) as previously reported (8, 21, 26). Pregnant mice were sacrificed by CO<sub>2</sub> overdose and decapitation and fetuses delivered by caesarean section. Isolated fetuses were decapitated and their backs were isolated from low thoracic and high lumbar regions and transversely sliced (275  $\mu\text{m}$ ) with a tissue chopper. After dissecting the spinal cord slices from the surrounding tissue, two of them were mounted on control glass coverslips (Control) or on 3D CNF attached to the coverslips, and arranged at a similar distance in both conditions, to interface slice growth. In both conditions, slices were embedded into a thick matrix obtained by chicken plasma (Rockland) and thrombin (Sigma) clot. Slices were cultured in plastic tubes with 1.5 mL medium containing 67% DMEM (Invitrogen), 8% sterile water for tissue culture, 25% fetal bovine serum (Invitrogen), and 25 ng/mL nerve growth factor (Alomone Laboratories); osmolarity, 300 mOsm; pH 7.35. The tubes were kept in a roller drum rotating 120 times per hour in an incubator at 37°C in the presence of humidified atmosphere, with 5% CO<sub>2</sub>. Slices were cultured for 10–17 days. To ensure

homogeneous experimental conditions between the two analyzed populations (Control and 3D CNF double explants), for electrophysiological and immunofluorescence experiments pairs of organotypic spinal explants with inter-slice distance (measured between the center of the two explants by bright field imaging) exceeding the 0.8–2.5 mm distance-range were discarded.

### *Electrophysiological recordings*

Coverslips with spinal cultures were placed in a recording chamber, mounted on an upright microscope (Leica DM LFS), and superfused with Krebs' solution containing (in mM): 152 NaCl, 4 KCl, 1 MgCl<sub>2</sub>, 2 CaCl<sub>2</sub>, 10 HEPES, and 10 Glucose. The pH was adjusted to 7.4 with NaOH. All experiments were performed at room temperature (RT; 20–22°C). Simultaneous extracellular recordings were obtained from the ventral area of each explant using low resistance glass micropipettes (4–6 MΩ) filled with KCl (20 mM) solution; microelectrodes were positioned with micromanipulators (Luigs and Neumann SM1, Germany) and advanced into spinal tissue manually by micro-steps. The electrodes were usually placed in close proximity (20–100 μm) to the ventral fissure, as this area, on both sides of the spinal cord, has been described as the prominent source of rhythmic activity in spinal slice cultures (57, 58). Voltage transients could be attributed to synaptic activity and action potential firing. Bursting activity was completely suppressed by bath-applied 6-Cyano-7-nitroquinoxaline-2,3-dione (CNQX; 10 μM) plus tetrodotoxin (TTX; 1 μM) in 100% of cases (n=13 explants, Control and 3D CNF; fig. S3B). The recorded signals were amplified (Axopatch 1D; Axon Instruments) and the offset of the traces was neutralized by current injection through the amplifier. Signals were recorded using the Clampex 8.2 software (pClamp suite, Axon Instruments) and acquired digitized (Digidata 1322A, Axon Instruments) at 10 kHz, filtered at 2 kHz and stored on a PC. Disinhibited rhythmic bursts were obtained by bath co-application of strychnine and bicuculline (1 μM and 20 μM, respectively)(20). Extracellular electrical stimulation was performed by placing a low-resistance patch pipette containing external bath solution in the dorsal horn of one explant, ipsilateral to the ventral area being recorded. Short current pulses (200 μs) of various amplitudes (i.e. the amplitude able to elicit the appearance of a voltage burst response in the ipsilateral ventral region in 100% of stimuli; ranges 100–500 μA; sample in fig. S3A), were delivered by a STG4002 stimulator (Multichannel Systems).



Recordings were off-line, lowpass-filtered at 20 Hz for spontaneous activity analysis, and for disinhibited bursts analysis at 100 Hz (cross-entrainment analysis) or 3 Hz (cross-correlation and inter-event interval analysis). To evaluate the frequency of spontaneous voltage transients (in the absence of any pharmacological treatment or electrical stimulation), only the events with peak amplitudes above threshold (set to three times the baseline noise) were included. Disinhibited bursts occurrence was evaluated by measuring the mean inter-event interval (IEI; i.e. the time between the beginning of one burst and the beginning of the following one; >25 bursts for each measure).

We further assessed the synchrony between the bursting activities of the two explants in each pair by computing the Pearson correlation coefficient between the two voltage time series as follows: in the experiments in which the Control slices were compared to 3D CNF slices (see Fig. 3A-D) or to 2D MWCNTs and 3D-PDMS (see fig. S2), the statistical significance of the correlation coefficient was determined by performing a permutation test (see fig. S1). For each pair of time series, we randomly sampled time windows of consecutive data points of size  $s = N/5$  (where  $N$  is the total number of data points of the time series), and, for each window, we computed the Pearson correlation coefficient between the resulting chunks of time series (see the example in fig. S1A, where the dashed lines indicate the extremes of a randomly sampled time window and the gray traces indicate the portions of the time series that were used to compute the correlation coefficient). This procedure was repeated  $10^4$  times, thus yielding  $10^4$  correlation coefficients that were averaged to obtain an estimate of the correlation between the two time series (for the sample of time series shown in fig. S1A, the resulting average correlation coefficient is shown by the red line in the plot of fig. S1C). This value was compared to the null distribution of correlation coefficients that was obtained by taking time windows of consecutive data points of the same size  $s$  as before, but with the onsets of the time windows that were independently, randomly sampled for the two time series (see, as an example, the gray portions of the time series in fig. S1B). Again, this procedure was repeated  $10^4$  times, yielding the distribution of correlation coefficients that one would expect to observe if the voltage signals recorded from a pair of explants happened to correlate purely by chance, even in absence of synchrony (see the histogram in fig. S1C). By measuring how likely it was for the values of this null distribution to be larger or equal than the real correlation coefficient (i.e., for the values of

the histogram in fig. S1C to be larger than the red line), it was possible to understand whether the correlation between the pair of time series was significantly larger than expected by chance (with  $P=0.05$ ). Since, in general, two time series could be anti-correlated as well as correlated, the same test was applied to the left tail of the null distribution, in case the measured correlation coefficient was negative (i.e., we checked how likely it was for the values of the null distribution to be smaller or equal than the measured correlation coefficient). This procedure allowed for determining what fraction of co-cultured slices exhibited a significantly synchronous bursting activity, for all the tested conditions. The resulting fractions of significantly synchronous slices were then compared by performing a homogeneity test with the chi-squared method (shown in Fig. 3D). For the stimulation-based experiments (Fig. 3E-G), the bursting activities of two explants in a pair were considered synchronous, when the magnitude of their CCF was larger than 0.5.

#### *Immunofluorescence labeling and confocal imaging of spinal slice explants*

Following electrophysiological recordings, spinal organotypic cultures were fixed with 4% formaldehyde (prepared from fresh paraformaldehyde; Sigma) in PBS. Coverslips were rinsed with PBS. Free aldehyde groups were quenched in 0.1 M glycine in PBS for 5 minutes. The samples were incubated for 30 minutes in a blocking solution (5% BSA, Sigma, 0.3% Triton X-100, Carlo Erba, 1% Fetal Bovine Serum, Gibco, in PBS), then incubated with anti- $\beta$ -tubulin III primary antibody (rabbit polyclonal; 1:250, Sigma) and SMI-32 primary antibody (mouse anti-neurofilament H antibody, 1:200, Sternberger Monoclonals Inc.) diluted in PBS with 5% FBS at 4°C, overnight. After subsequent washing in PBS, samples were incubated in secondary antibodies (goat anti-mouse Alexa 488, Invitrogen, 1:500; goat anti-rabbit Alexa 594, Invitrogen, 1:500; DAPI, Invitrogen 1:500) for 2 h at room temperature. Following secondary antibody incubation, samples were washed in PBS and briefly rinsed with water and mounted on glass coverslips using Vectashield hardset mounting medium (Vector laboratories).

Images were acquired using Nikon C2 or Leica DMIRE2 Confocal microscopes, both equipped with Ar/Kr, He/Ne, and UV lasers. Images were acquired with a 40 $\times$  or 63 $\times$  oil objective (numerical aperture 1.4) using oil mounting medium (1.515 refractive index). Confocal sections were acquired every 1  $\mu\text{m}$  and the total Z-stack thickness was set such that all emitted

fluorescence was collected from the sample. In order to visualize the 3D CNF scaffold along with the immunolabeled components, the reflection mode setting (excitation with the 488 nm laser line and acquisition of the reflected signal in the 460–500 nm range) available in the Leica confocal microscope was utilized. Analysis and 3D reconstruction of the image Z-stacks were accomplished using one of the following softwares: NIS-Elements AR (Nikon), Volocity (PerkinElmer), and FIJI (<http://fiji.sc/Fiji>).

Analysis of fiber outgrowth morphology was performed by selecting random regions of 160  $\mu\text{m}$  *per* 160  $\mu\text{m}$  of visual field dimension at 40 $\times$  magnification. To visualize and appreciate the difference in the 3D distribution of the neuronal processes in Control and 3D CNF networks, the three-dimensional extent of the processes was also visualized by color-coding for the thickness through which they extended; FIJI and MATLAB software packages were employed for this analysis. The Z-stacks of representative neuronal processes extensions were first viewed using FIJI and color-coded for the thickness by using the *Temporal-color code* command in the *Hyperstacks* section of the software. The images obtained were then visualized in MATLAB and the figure color-map was set such that for both conditions, the color depth demonstrated equal thickness, thus ensuring homogeneity in the color scheme in Control and 3D CNF. To quantify the distribution of neuron processes along the thickness of the image stack, 9 regions from 6 coverslips of Control and 14 regions from 5 coverslips of 3D CNF were compared. The thickness through which the immunolabeled processes were distributed was calculated (using FIJI) and the statistical differences between the datasets were assessed by Student's t test (after validation of variances homogeneity by Levene's test; Statistica software).

In order to rule out any possible discrepancy in the fluorescence emission due to the 3D scaffold, images of fluorescent beads (2  $\mu\text{m}$  biodegradable micro-particles from Kisker, PBD-GF-2.0; a kind gift from Dr. Dan Cojoc, CNR-IOM, Trieste) deposited on glass and on 3D CNF were acquired using identical settings. The intensity of the fluorescence was analyzed using the Volocity software to confirm that the substrate did not produce any artifact in the emitted fluorescence signal.

### *Brain tissue implantation with 3D CNF*

The implant consisted of a sharp-pointed cylinder (~2 mm length,  $0.5\pm 0.2$  mm in diameter) carved out of a larger 3D CNF scaffold and mounted on an electrode holder (ZIF-Clip<sup>®</sup>, Tucker-Davis Technologies, USA). Scaffold stiffness was increased before carving procedure in order to facilitate the insertion of the material into the brain tissue. This stiffening was achieved by filling the scaffold with water-soluble polyethylene glycol (PEG), a biocompatible polymeric material commonly used for implants and hydrogels (59, 60). Briefly, the 3D CNF scaffold was dipped into melted PEG-4000 (Poly(ethylene glycol); 81240 from Sigma Aldrich, average MW 4,000 Da) at 65°C. PEG molecules permeate the scaffold, filling all empty spaces. The sample was allowed to cool to RT and shaped with a razor blade. To facilitate handling and positioning during the surgical procedure, the scaffold was fixed to the electrode holder using PEG.

All surgical procedures were performed on Wistar male rats (Harlan Laboratories), 3–6 months of age and weighing 450–550 gr. Anesthesia was induced and maintained with Isoflurane (2% in 100% O<sub>2</sub>, Sigma Aldrich) administered via a nose cone throughout the procedure. Anesthetic depth was monitored by checking the absence of tail and paw reflexes. The anesthetized animal was placed in a stereotaxic apparatus (Narishige SR-5R, Japan) to measure the exact location of the craniotomy and the penetration site. Body temperature was maintained at 37°C with a thermostatically controlled heating pad (temperature control unit HB 101/2; Panlab/Harvard Apparatus, Barcelona, Spain) to avoid anesthesia-induced hypothermia. Heart rate and oxygen saturation level were constantly monitored via a pulse oxymeter (Pulsesense LS1P-10R, Nonin Medical Inc, Medair AB, Hudiksvall, Sweden). A square, 2 mm × 2 mm craniotomy was performed over the left hemisphere using a micro drill and the *dura mater* was removed, exposing the brain. Tissue adhesive (B. Braun Aeusculap, Germany) was applied on the inner perimeter of the craniotomy to prevent brain dimpling.

The PEG-stiffened 3D CNF scaffold was inserted at –4.5 mm from Bregma (in the anterior-posterior axis) and –3.5 mm in the medial-lateral axis. These coordinates refer, in the adult rat, to the visual cortex, specifically to the cortical junction between V2ML and V1 (61). 3D CNF scaffold was quickly placed into the cortex via a micro-drive at a speed of insertion of about 0.5 mm/s in order to prevent premature PEG melting. When the desired depth was reached, i.e. the

sponge penetrated the cerebral tissue for approximately its whole length (~2 mm in the dorsal-ventral axis), the craniotomy was filled with silicone (Kwik-Cast&Kwik-sil, World Precision Instrument, USA) in order to isolate the exposed brain tissue, and the whole skull surface covered by bone cement (Super Bond, C&B, USA).

Throughout the whole procedure, both rat eyes and cortex were periodically irrigated, using an ophthalmic solution (Epigel, CevaVetem, Italy), and a 0.9% NaCl saline solution, respectively. Atropine (1.5 mg/kg, subcutaneous) and Lactated Ringer's Solution (1 mL, subcutaneous) were administered every hour, to reduce secretions and maintain the animal's physiological state. Analgesic solution (Rymadyl; 5 mg/kg, intraperitoneal) and antibiotic (Baytril; 5 mg/kg, intramuscular) were administered to the rat via injection, immediately before the surgery and one hour prior to the end of the surgical procedure. Both solutions were administered following surgery via the animals' drinking water for three days post-surgery. Animals were monitored for recovery immediately after the surgery and at least 3 times per day for the first 72 h. We used a general distress-scoring sheet (Institutional Standards for the Care and Use of Animals in Research and after consulting with a veterinarian) to assess pain and distress in animals using physiological (appearance) and behavioral (natural and provoked behavior) parameters. For each parameter a numerical score starting from 0=normal and reaching 3=grossly abnormal is determined. An extra point is added for each 3 given. The provoked behavior was tested first after 72 h post-implantation. This method allows an objective monitoring of animals general conditions, to evaluate the need of analgesics or euthanization. All the animals used in the study did not show any sign of pain or distress (score=0). Following this 72 h period, animals were monitored once per day until sacrifice.

#### *Brain tissue preparation, immunohistochemistry, image acquisition, and analysis*

Animals were sacrificed at 4 weeks post-implantation and, in an exploratory longitudinal study, at five different post-implantation time points, as follows: 0 weeks (in which the animal was euthanized immediately after the implantation, "acute"), 1 week, 2 weeks, 4 weeks and 8 weeks. Animals were anesthetized with 5% chloral hydrate (7 mL/kg) and then perfused transcardially with 0.1 M PBS followed by 4% PFA in PBS. Brains were removed, postfixed for 24 h at 4°C, and cryoprotected in 15% sucrose in PBS at 4°C for 24 h and then in 30% sucrose in PBS at 4°C

for at least 24 h. Finally, brains were embedded in optimal cutting temperature (OCT) compound (Tissue-Tek), frozen at  $-20^{\circ}\text{C}$ , and cryosectioned horizontally in 25  $\mu\text{m}$  thick sections.

Tissue-Tek was removed by PBS washing and tissue sections were incubated 5 min in glycine 0.1 M and blocked in 3% BSA, 3% FBS, 0.3% Triton X-100 in PBS for 30 min at room temperature followed by incubation overnight at  $4^{\circ}\text{C}$  with primary antibodies (mouse anti-GFAP, 1:200, Sigma; rabbit anti-Iba1, 1:400, Wako; rabbit anti- $\beta$ -tubulin III, 1:250, Sigma; mouse anti-NeuN, 1:100, Millipore; mouse anti-CD68/ED1, 1:100, AbD Serotec; rabbit anti-CX3CR1, 1:200, Sigma) in 5% FBS in PBS. After washing in PBS, sections were incubated in secondary antibodies (goat anti-rabbit Alexa 594, 1:500, Invitrogen; goat anti-mouse Alexa 488, 1:500, Invitrogen; DAPI, 1:200, Invitrogen) in 5% FBS in PBS for 2 h at room temperature. Sections were mounted on glass coverslips using Vectashield hard mounting medium (Vector Laboratories).

We measured the brain tissue reaction at specific time after implants by markers for reactive astrocytes, with glial fibrillary acidic protein (GFAP), for microglia with ionized calcium-binding adaptor protein-1 (Iba1), and for neurons ( $\beta$ -tubulin III; NeuN). In order to quantify GFAP and Iba1 labeling, fluorescence images were acquired using a Leica DM6000 upright microscope with a  $10\times$  dry objective. Identical binning, gains and exposure times were used for all images of the same marker. Image analysis was performed using the FIJI software. Different quantification methods were used for GFAP and Iba1 labeling. For GFAP, eight regions of interest (ROIs;  $100\ \mu\text{m} \times 500\ \mu\text{m}$ ) were drawn at random intervals around the implant, starting from the edge of the implant and extending 500  $\mu\text{m}$  into the surrounding tissue. Within each ROI, three intensity profile lines were selected blindly in order to obtain a fluorescence intensity profile as a function of distance from the implant edge. To account for variations in labeling, the fluorescence intensity in the contralateral hemisphere was defined as the background intensity for each brain section and normalized to 1(37). The mean intensity profile for each animal was calculated for each micron of 0–150  $\mu\text{m}$  from the implant edge. Because differences in GFAP intensity were within a maximum of 50  $\mu\text{m}$  from the implant, the data from 0–150  $\mu\text{m}$  were further normalized to the mean intensity for 51–150  $\mu\text{m}$ .

In the longitudinal study (n=1 animal per time point; fig. S5) the mean GFAP fluorescence intensity in the 0–50  $\mu\text{m}$  ROI was increased from 4 to 8 weeks post-implantation ( $1.07\pm 0.13$  and  $1.05\pm 0.11$  normalized intensity/ $\mu\text{m}$ , respectively; n=56 and 80 ROIs) compared to 0, 1, and 2 weeks post implantation ( $0.94\pm 0.10$ ,  $0.92\pm 0.14$ , and  $0.94\pm 0.12$  normalized intensity/ $\mu\text{m}$ , respectively; n=40 ROIs for 0 and 1 weeks, n=64 ROIs for 2 weeks; fig. S5A-B).

For Iba1 labeling, eight  $100\ \mu\text{m} \times 500\ \mu\text{m}$  ROIs were selected starting from the edge of the implant and extending  $500\ \mu\text{m}$  into the surrounding tissue. The background intensity threshold was defined for each tissue section using the Iba1 labeling intensity measured in the contralateral hemisphere in the same anatomical region as the implanted material. The area within each ROI with intensity above the background threshold was calculated.

In the longitudinal study, the Iba1 immunoreactivity was greatly increased at 1 week post-implantation compared to the acute/ 0 weeks (Iba1-positive area/total area:  $0.34\pm 0.18$  and  $0.043\pm 0.02$ , respectively; n=32 and 32 ROIs, fig. S5C-D). Furthermore, microglia cells were clearly invading the 3D CNF. At 2 and 4 weeks post-implantation, the Iba1 labeling was still increased compared to the acute/0 weeks post-implantation (Iba1-positive area/total area:  $0.089\pm 0.06$ , n=64 ROIs,  $P=0.018$  and  $0.16\pm 0.11$ , n=40 ROIs); however, the reactivity at these time points was *reduced* compared to the 1 week post-implantation tissue, meaning that microglia surrounding the implanted material were primarily active in the first week following the implantation and then activation declined with time. This was further confirmed at 8 weeks post-implantation, in which the Iba1 labeling around the implant (Iba1-positive area/total area:  $0.04\pm 0.03$ , n=64 ROIs) returned to baseline condition.

In addition to the GFAP and Iba1 analysis of the animals at 4 weeks post-implantation, we analyzed the tissue for CX3CR1 and CD68/ED1, markers of inflammation and reactive astrocytes (data not shown). For this analysis, three  $150\ \mu\text{m} \times 150\ \mu\text{m}$  ROIs were selected within each 3D CNF scaffold. The background intensity threshold was defined for each tissue section using the corresponding labeling intensity measured in the contralateral hemisphere in the same anatomical region as the implanted material. The area within each ROI with intensity above the background threshold was calculated. We performed this analysis on animals sacrificed at 4

weeks post-implantation. The average values obtained for CX3CR1 (CX3CR1-positive area/total area:  $0.32 \pm 0.23$ ,  $n=18$  ROIs) and CD68/ED1 (CD68/ED1-positive area/total area:  $0.12 \pm 0.17$ ,  $n=18$  ROIs) represent the 36% and 13% of the total amount of microglia cells (calculated in the same way based on Iba1 labeling), respectively, indicating a relatively low percentage of reactive microglia inside the 3D CNF scaffold. Moreover, CD68/ED1-positive cells were totally absent in the surrounding tissue.

Confocal images of brain tissue sections were acquired and processed using the same equipment and procedures as the spinal slice explants, as described above.

### *Scanning Electron Microscopy*

3D CNF morphology was qualitatively assessed through scanning electron microscopy (SEM). Images were acquired collecting secondary electrons on a Gemini SUPRA 40 SEM (Carl Zeiss NTS GmbH, Oberkochen). Bare scaffolds were mounted on conductive double side carbon tape (Ted Pella, Inc., USA) and imaged at 5 keV.

### *Mechanical characterization*

For compressive tests, cubic samples of 3D CNF scaffolds were used, with a dimension of 5 mm per side. Uniaxial micro-compression tests were conducted on a Galdabini SUN 500 apparatus. Before compressive testing, a 0.01 N preload was applied to ensure a complete contact between the sample and the two flat surfaces compressing it. A constant speed ( $15 \mu\text{m/s}$ ) loading cycle was used with a load limit fixed at 10 N. After the limit was reached, we recorded discharging cycle to point out potential sample plastic deformation. Final peak displacement was about 3 mm. Scaffolds were indented using a 20 mm flat punch using a high sensitivity load cell for data collection (CTCA10K5 – AEP Transducers, Italy). Tests were operated at room temperature in air. Elastic data were determined by calculating the initial linear slope of the stress-strain curve.



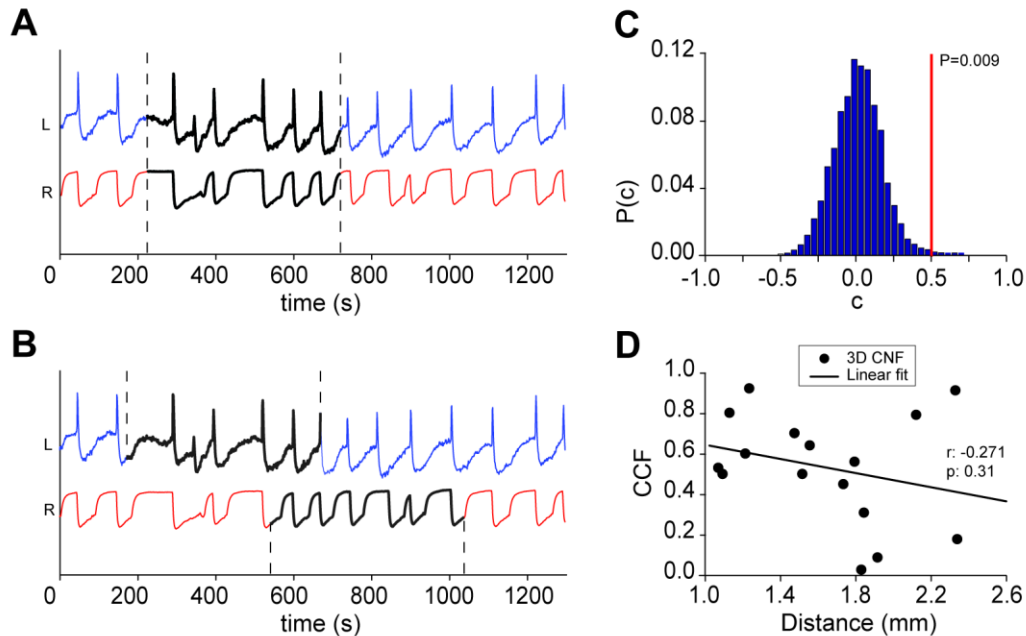


**Figure S1. Illustration of the permutation test to assess the statistical significance of the synchrony between the bursting activities of two co-cultured explants.**

**A.** Two example extracellular recordings (L, left slice; R, right slice) obtained from co-cultured slices that have been pharmacologically disinhibited. The recordings show rhythmic bursting activity, where the synchrony between the slices was determined by computing their Pearson correlation coefficient in time windows ( $10^4$  distinct time windows) that were randomly sampled from the whole duration of the recording (a single example time window is shown delineated by the dashed lines). **B.** To obtain a null distribution of correlation coefficients expected to be observed by chance, the randomly selected time window (dashed lines) for one slice was shifted within the trace and compared for synchrony with a similar length time window (now at a different time point) for the second slice. This analysis was repeated  $10^4$  times to obtain a null distribution of the correlation coefficients. The figure shows one of such randomly chosen time windows (dashed lines) and the resulting portions of the recordings (gray traces) that were compared to determine the correlation coefficient. **C.** The figure shows the null distribution (histogram, blue) of correlation coefficients for a pair of slices produced by the randomization procedures described in **B**. The red line indicates the true correlation coefficient for the same slices determined as described in **A**. For the traces shown, the true CCF value is +0.5 (red line) and the probability of observing null distribution values equal to or larger than the actual correlation coefficient ( $CCFs \geq 0.5$ ) was very low. Therefore, the bursting activity of the slices was significantly ( $P=0.009$ ) more synchronous than expected by chance. **D.** The distance between the two slices (center of slice to center of slice, in mm) does not affect the cross-correlation coefficient (CCF) in 3D CNF samples (black line indicates the regression line,  $r=-0.271$ ,  $p=0.31$ ), indicating that sample synchrony is not determined by how far the slices are separated.

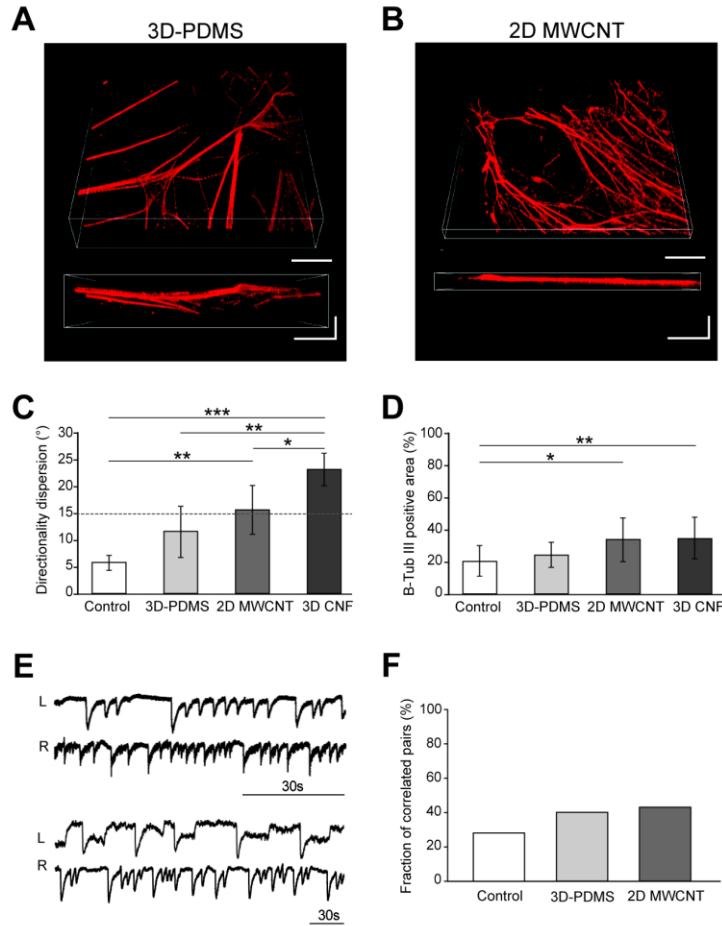


**Figure S2. Organotypic spinal slices cultured on 3D-PDMS scaffolds and on 2D MWCNT substrates.**

**A** and **B**. Confocal microscopy reconstruction depicting the three-dimensional growth of  $\beta$ -tubulin III-positive fibers on the 3D-PDMS scaffolds and on the 2D MWCNT substrates, respectively. Below, side views of reconstructions of these samples show neurites infiltrating through the z-axis on 3D-PDMS scaffolds (to a 126  $\mu\text{m}$  depth), or fasciculated into bundles and flattening on 2D MWCNT substrates (to a 40  $\mu\text{m}$  thickness). **C**. Histograms depict the average angle of dispersion of the fibers in Control, 3D-PDMS, 2D MWCNT, and 3D CNF samples. The lower angle of dispersion in Controls suggests that neurite fiber bundles are more oriented compared with 3D CNF, in which there is a high degree of dispersion, paralleling the mesh-like formation of the fibers (Control vs. 2D MWCNT  $P=0.008$ ; Control vs. 3D CNF  $P=0.000001$ ; 3D-PDMS vs. 3D CNF  $P=0.003$ ; 2D MWCNT vs. 3D CNF  $P=0.012$ ; overall significance determined by one-way ANOVA:  $F(3,38)=12.24$ ,  $P=0.000009$ ). **D**. Plots summarizing the average percentage of sample area from fiber reconstruction images positive for  $\beta$ -tubulin III immunofluorescence. These data suggest at the fiber density of the samples, but do not account for the dispersion of fibers into the third dimension. There were significant increases in  $\beta$ -tubulin III-positive area in CNT-containing samples over Controls (overall significance,  $F(3,38)=3.99$ ,  $P=0.015$ ; Control vs. 2D MWCNT  $P=0.011$ ; Control vs. 3D CNF  $P=0.004$ ). **E**. Representative LFPs of disinhibited bursts recorded simultaneously from paired slices grown on 3D-PDMS (top) and 2D MWCNT (bottom); note the absence of left-right correlation in these sample tracings. **F**. Plots of pooled data summarizing the mean fraction of correlated pairs detected in Controls, 3D-PDMS, and 2D MWCNT ( $n=7, 5, 7$ , respectively). These values did not significantly differ (Control vs. 3D-PDMS  $P=0.68$ ; Control vs. 2D MWCNT  $P=0.58$ ; 3D-PDMS vs. 2D MWCNT  $P=0.92$ ).

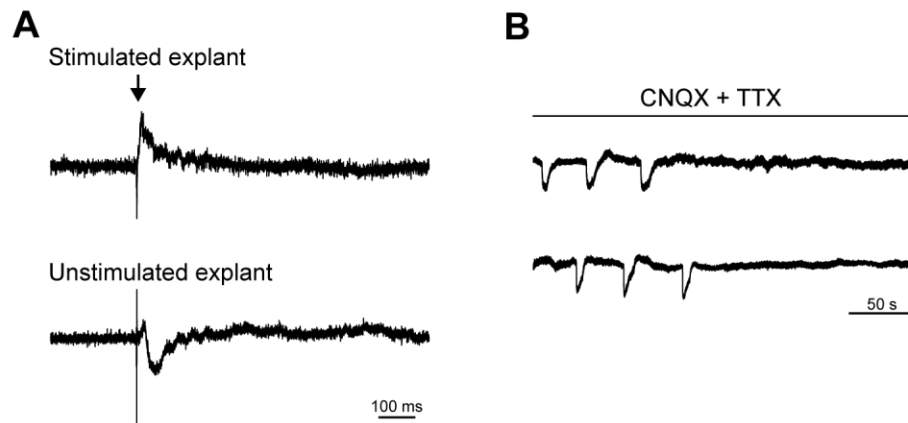


**Figure S3. Extracellular voltage transients represent evoked or spontaneous synaptic, action potential mediated, activity.**

**A.** Tracings of evoked LFPs recorded from the ventral horn of two co-cultured spinal explants in 3D CNF. The response to the dorsal electrical stimulation (arrow) is shown in the directly stimulated (top) and in the correlated (bottom) spinal slice. The delay between the application of electrical stimulation and the response onset in the directly stimulated explant was similar in both 3D CNF and Controls ( $6.2 \pm 2.0$  ms,  $n=4$  3D CNF;  $6.4 \pm 0.7$  ms,  $n=5$  Control). **B.** Bursting activity recorded in the presence of strychnine and bicuculline in Control slice pairs is completely suppressed by CNQX ( $10 \mu\text{M}$ ) and TTX ( $1 \mu\text{M}$ ) application.

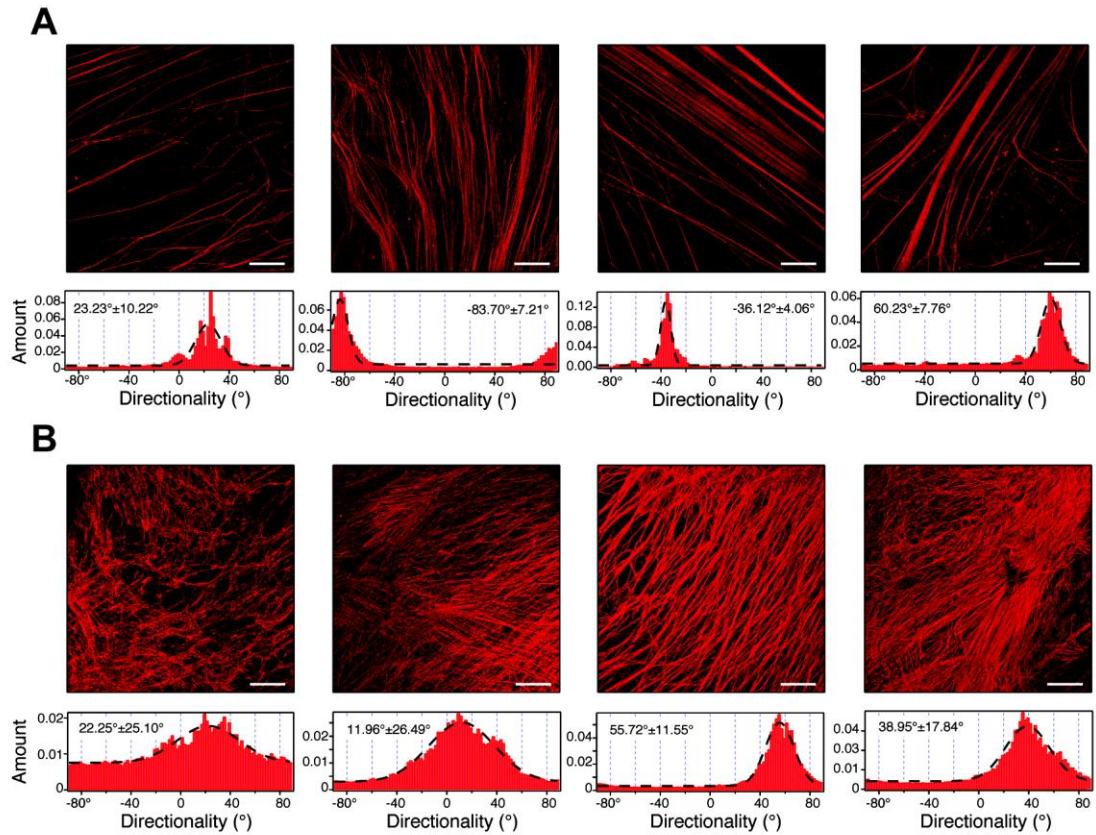


**Figure S4. Directionality analysis of spinal neuronal processes outgrowth.**

**A.** Confocal images representative of Control neuronal projection appearance (top,  $\beta$ -tubulin III stained;  $n=4$  cultures) and corresponding fiber angular distributions (bottom); note that in the majority of cases the mean directionality dispersion is lower than  $10^\circ$ . **B.** Confocal images representative of 3D CNF neuronal projection appearance (top,  $\beta$ -tubulin III stained;  $n=4$  cultures) and corresponding fiber angular distributions (bottom); note that in these samples the mean directionality dispersion is higher than  $10^\circ$ . Mean values and dispersion were calculated from Gaussian fitting (black dashed line) of fibers angular distribution and reported as histogram inset. We define a field as “oriented” if the direction dispersion is lower than  $10^\circ$ , otherwise it is defined as “random”. See SI Materials and Methods for details. Scale bars:  $100\ \mu\text{m}$ .

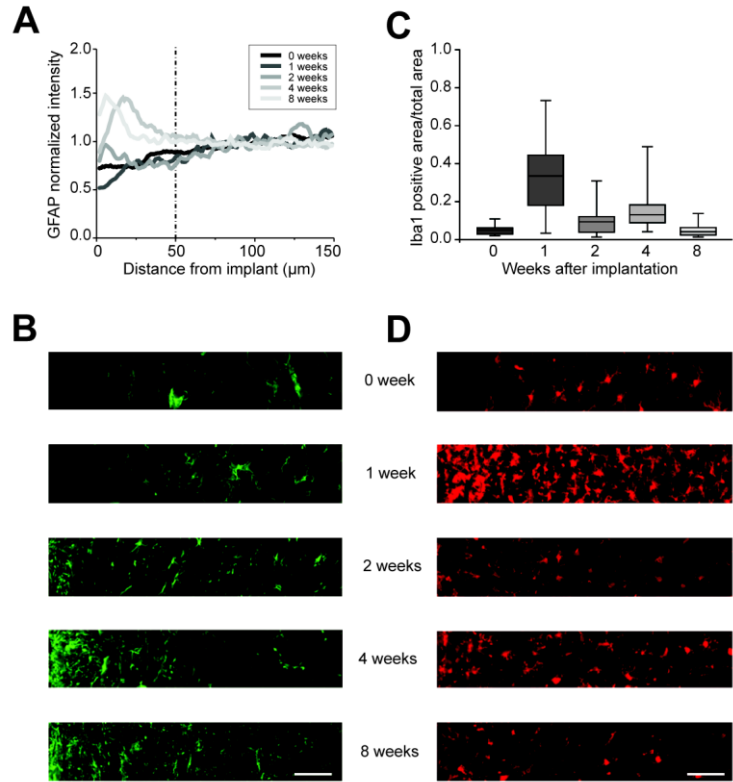


**Figure S5. Immune reaction over time to CNF scaffolds implanted into the adult rat visual cortex.**

**A.** GFAP fluorescence intensity profile in the surrounding tissue as a function of the distance from the edge of the implant. **B.** Representative images of the ROIs used for analysis, showing GFAP labeling (green) at the different time points post implantation; the edge of the CNF scaffold forms the left border of each image. **C.** Mean Iba1-positive area measured up to 500  $\mu\text{m}$  from the edge of the implant. **D.** Representative images of ROIs demonstrating the Iba1 fluorescence labeling (red); the edge of the CNF scaffold forms the left border of each image. Scale bars in **B** and **D**: 50  $\mu\text{m}$ .

# Nanostructures to Engineer 3D Neural-Interfaces: Directing Axonal Navigation toward Successful Bridging of Spinal Segments

Emily R. Aurand, Sadaf Usmani, Manuela Medelin, Denis Scaini, Susanna Bosi, Federica B. Rosselli, Sandro Donato, Giuliana Tromba, Maurizio Prato,\* and Laura Ballerini\*

Neural interfaces are the core of prosthetic devices, such as implantable stimulating electrodes or brain–machine interfaces, and are increasingly designed for assisting rehabilitation and for promoting neural plasticity. Thus, beyond the classical neuroprosthetic concept of stimulating and/or recording devices, modern technology is pursuing toward ideal bio/electrode interfaces with improved adaptability to the brain tissue. Advances in material research are crucial in these efforts and new developments are drawing from engineering and neural interface technologies. Here, a microporous, self-standing, 3D interface made of polydimethylsiloxane (PDMS) implemented at the interfacing surfaces with novel conductive nanopopographies (carbon nanotubes) is exploited. The scaffold porosity is characterized by 3D X-ray microtomography. These structures are used to interface axons regenerated from cultured spinal explants and it is shown that engineering PDMS 3D interfaces with carbon nanotubes effectively changes the efficacy of regenerating fibers to target and reconnect segregated explant pairs. An improved electrophysiological performance is shown when the spinal tissue is interfaced to PDMS enriched by carbon nanotubes that may favor the use of our substrates as regenerative interfaces. The materials are implanted in the rat brain and a limited tissue reaction surrounding the implants at 2, 4, and 8 weeks from surgery is reported.

that limits the performance, the longevity, and the stability of prostheses.<sup>[1,2]</sup> More recently, interfaces are increasingly engineered not only to improve neural recording and stimulation, but to promote neural regeneration together with the therapeutic delivery of bioactive molecules. In these developments, the interface architecture is redesigned by the use of tailored materials with nanoscale geometries mimicking topographical cues able to improve neuronal growth, viability, and adhesion.<sup>[3–5]</sup> In further advances, regenerative interfaces are cellularized by the inclusion of cell grafts to provide a target site for reinnervation. Thus, interfaces of the future may require more sophisticated neural–material hybrids tested in the laboratory to create 3D constructs that are more easily recognized by brain networks.<sup>[4,6]</sup>

We recently developed a microporous, self-standing, elastomeric scaffold made by polydimethylsiloxane (PDMS) with micrometric cavities generated upon dissolving a sugar template that was previously embedded in PDMS and we further

nanostructured the scaffold by means of carbon nanotubes, implementing the polymer with novel nanopopographies with which cells can actively interact.<sup>[7]</sup>

Carbon nanotubes have repeatedly been shown to provide an electrically favorable environment to potentiate neuronal signaling.<sup>[8–13]</sup> Improved signaling between neural cells can

## 1. Introduction

Neural prostheses are artificial, implantable devices designed to restore functions that are lost in injured or diseased central nervous system (CNS). In manufacturing CNS implants, the tissue–electrode interface represents a crucial component

Dr. E. R. Aurand, S. Usmani, Dr. F. B. Rosselli, Prof. L. Ballerini  
Scuola Internazionale Superiore di Studi Avanzati (SISSA) Via Bonomea  
265-34136 Trieste, Italy  
E-mail: laura.ballerini@sissa.it


Dr. M. Medelin, Dr. D. Scaini  
Department of Life Science  
University of Trieste  
Via Giorgieri, 1-34127 Trieste, Italy

Dr. S. Bosi, Prof. M. Prato  
Department of Chemical Sciences  
University of Trieste  
Via Giorgieri, 1-34127 Trieste, Italy  
E-mail: prato@units.it

Dr. S. Donato, Dr. G. Tromba  
Elettra-Sincrotrone Trieste S.C.p.A. Strada Statale 14 – km 163.5 in AREA  
Science Park  
34149 Basovizza, Trieste, Italy

Prof. M. Prato  
Carbon Nanobiotechnology Laboratory  
CIC biomaGUNE  
Paseo de Miramón 182, 20009 Donostia-San Sebastián, Spain

Prof. M. Prato  
Basque Fdn Sci  
Ikerbasque, Bilbao 48013, Spain

 The ORCID identification number(s) for the author(s) of this article can be found under <https://doi.org/10.1002/adfm.201700550>.

DOI: 10.1002/adfm.201700550

potentially aid in cell maturation and in the formation of complex, functional neuronal networks.<sup>[10,11]</sup> A polymer material incorporated with carbon nanotubes is, therefore, likely much more advantageous when attempting to build an interactive interface to improve axonal growth and guide synapse formation and function.

Organotypic spinal slice cultures represent a complex in vitro model where both sensory-motor cytoarchitecture and electrical properties are retained in a 3D-fashion.<sup>[10,14,15]</sup> We recently used such a model to test the ability of pure carbon nanofiber 3D interfaces in promoting successful reconnection of separated spinal explants in vitro.<sup>[16]</sup> Here, we exploit cultured slices used as pairs to test 3D PDMS interfaces with or without carbon nanotubes. Previous studies have shown that spinal slices separated at distances more than 300  $\mu\text{m}$  fail to reconnect under basal conditions,<sup>[7,15–18]</sup> despite the huge outgrowth of nerve fibers,<sup>[10,14,16]</sup> allowing for the investigation of potential reconnection in the presence of efficacious cues. In this study, we investigate by electrophysiology, immunofluorescence, and confocal microscopy, organotypic slices interfaced to 3D scaffolds made of polymer-alone or polymer and nanotubes. In particular, we address the navigation within the artificial structures of neuronal fibers exiting the slices and we correlate neurite distribution at the interface with functional slice-to-slice reconnection.

We also investigate the biocompatibility of the PDMS constructs in vivo upon implantation into adult rat visual cortex<sup>[16]</sup> observed at 2nd, 4th, and 8th week postsurgery time-points. We use immunofluorescence labeling to quantify the density of inflammatory response-mediating cells surrounding the implant material and of neuronal markers to assess the level of cellular infiltration into the scaffold in situ.

Our data indicate that the incorporation of carbon nanotubes into a 3D polymer construct confers increased neuronal activity in the spinal networks developed at the interface and guides regrowing axons toward functional reconnection of separated spinal explants. We also suggest that PDMS with carbon nanotube materials elicit minimal immune response following implantation into the CNS.

## 2. Results and Discussion

### 2.1. Scaffolds Used to Interface Organotypic Slice Cultures: A Microtomography Analysis

Two different, microporous, free-standing, elastomeric scaffolds, able to sustain the development of organotypic slices, were developed following the procedure described in our previous work.<sup>[7]</sup> PDMS scaffolds are the negative replica of a generating sugar framework; this allows for fabrication of 3D sponge-like structures characterized by irregular porosity, with random channels connecting the pores. Within the same fabrication procedure, we generate micrometric cavities by a sugar mold previously mixed to multiwalled carbon nanotubes<sup>[7]</sup> (MWCNTs, **Figure 1**). This permits the formation of 3D sponges with the pore surfaces layered by a MWCNT carpet, stably trapped in the PDMS matrix.<sup>[7]</sup> Scanning electron microscopy (SEM) analysis of the PDMS scaffolds and of the

PDMS decorated by the MWCNTs (PDMS+CNT) reveals similar “sponge-like” morphologies (Figure 1a,b), with the PDMS+CNT showing the presence of a layer of MWCNTs lining the inner facets of the pores (Figure 1b, inset).

3D X-ray microtomography ( $\mu\text{CT}$ ) reconstructions allow a comparison of the inner pore and channel morphologies of the two materials (Figure 1c). These measures show that both scaffolds display similar hollow features. Regarding the general porosity, PDMS scaffolds ( $n = 3$ ) contain  $50\% \pm 11\%$  empty volume and similarly, in PDMS+CNT scaffolds ( $n = 3$ ), the empty volume is  $54\% \pm 6\%$  (Figure 1d). Interestingly, the isotropic index is  $0.89 \pm 0.03$  and  $0.91 \pm 0.02$  for PDMS and PDMS+CNT samples, respectively. This reveals that pore shape and channel directions are both isotropic traits of the manufactured scaffolds (Figure 1d). The diameter of the inscribed sphere (mean  $\pm$  SD) in PDMS samples is  $29 \pm 8 \mu\text{m}$ , with the interconnecting channel mean size of  $16 \pm 1 \mu\text{m}$ , while in PDMS+CNT scaffolds the mean inscribed sphere diameter is  $23 \pm 2 \mu\text{m}$ , with  $14 \pm 1 \mu\text{m}$  channel size (Figure 1e). These values were not significantly different ( $P = 0.25$  and  $P = 0.14$  for pores and throats, respectively; Figure 1e).

After this characterization, PDMS and PDMS+CNT substrates were used over extended periods to interface the development of neural networks in long-term, cocultured pairs of mouse organotypic spinal cord explants.<sup>[10,16]</sup>

### 2.2. Spinal Explants Interfaced to the PDMS and PDMS+CNT Constructs: Axonal Colonization of the Interfaces in the Third Dimension

Spinal organotypic slices after >10 d of in vitro development exhibit a characteristic outgrowth of nerve fibers<sup>[10,16]</sup> and a rich neurite network observed in PDMS and PDMS+CNT conditions (**Figure 2a,b**). Pairs of slices, when interfaced to PDMS or to PDMS+CNT, sprout neuronal processes that rapidly invade the 3D structure of the interfaces. In this set of experiments, we explore the infiltration of fibers within the sponges<sup>[10,16]</sup> and we investigate their patterns of growth by confocal microscopy and comparing the regions of interest (ROI:  $640 \times 640 \mu\text{m}$ ; 20 and 28 ROI,  $n = 5$  and  $n = 9$  cultures, PDMS and PDMS+CNT, respectively) sampled from the area surrounding the slice explants.<sup>[16]</sup>

To determine if there were any differences between the PDMS and PDMS+CNT substrates' ability to guide neuronal process distribution, we acquired z-stacks to reconstruct the sampled ROIs (Figure 2a,b, right panels) and measured the thickness through which the  $\beta$ -tubulin III-positive neurites were detectable within the interface materials.

Image stacks demonstrate that neurites are distributed in complex network formations across the surface of the substrates, reaching varying depths into the manufactured interfaces (Figure 2a,b, right panels). Interestingly, we found that the depth through which neurites are traveling in the PDMS substrates (see Figure 2a,b, bottom insets to right panels) is significantly greater than the neurite distribution in PDMS+CNT substrates ( $105.5 \pm 8.6$  and  $52.7 \pm 3.9 \mu\text{m}$ , respectively,  $P < 0.001$ ; Figure 2c), despite the absence of any significant difference in substrate pore/channel size (Figure 1e), excluding

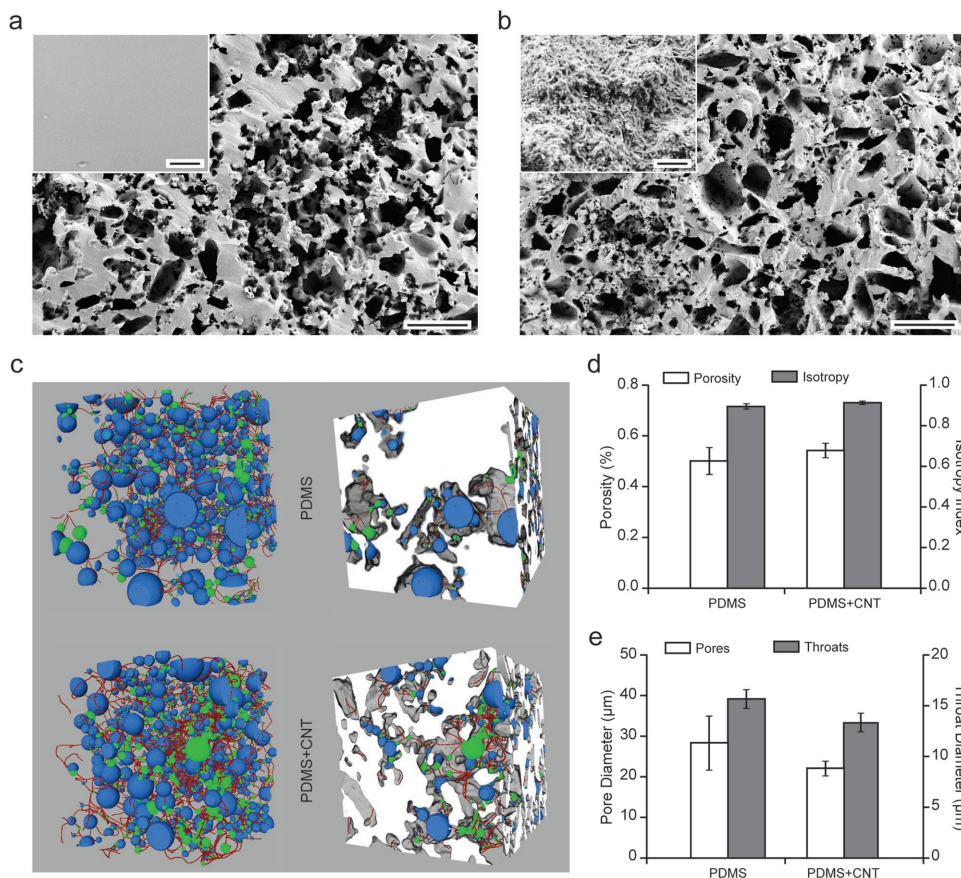


**Figure 1.** PDMS and PDMS+CNT scaffolds: SEM and  $\mu$ CT measures. a) SEM image of a PDMS scaffold slice showing the typical “sponge-like” aspect. The high-resolution image of the pore surface shown in the top-left inset highlights the PDMS smoothness. b) SEM image of a PDMS+CNT scaffold slice showing a similar porous morphology; a high-resolution image of the pore surface (top-left inset), nicely illustrates the carpet of MWCNTs decorating exclusively pores’ walls and resulting in a rough surface. SEM images scale bar: 100  $\mu$ m. Inset scale bars: 1  $\mu$ m. c) Left, an example of  $\mu$ CT volumetric reconstructions of scaffolds’ pores and channelization in a ROI of 5123 voxels of the total volume. In blue and green, the maximal filling sphere for pore and throat diameter determinations, respectively, and in red, the interconnection path. Right, the scaffold’s matrices (in white) are shown. Both samples show that all empty spaces inside the material are interconnected. d) Histograms revealing that the two scaffolds have similar levels of porosity and isotropy. e) Histogram showing the similar average values for pore diameters and throat diameters for both samples ( $n = 3$  for PDMS,  $n = 3$  for PDMS+CNT). Bars show mean  $\pm$  SD values.

that a mere variability (in the micrometer scale) of the PDMS- and PDMS+CNT-interfaced skeleton influenced the permeation of growing neurites.

To further explore the differences in fiber outgrowth and morphology within the 3D interfaces, we also quantified the overall neurite density and the degree of dispersion.<sup>[16]</sup> In fact, depending on the substrate that supports the elongation of neuronal projections exiting the interfaced spinal explant, neural fibers can be organized in thick bundles of aligned processes<sup>[10]</sup> or in complex webs of randomly oriented fibers.<sup>[16]</sup>

First, we estimated neuronal fiber density.<sup>[16]</sup> By this procedure, we detect no differences in the amount of  $\beta$ -tubulin III-positive area between PDMS ( $28.05 \pm 2.89\%$  positive area,  $n = 29$  ROIs acquired from  $n = 10$  cultures) and PDMS+CNT ( $26.77 \pm 3.53\%$  positive area,  $n = 20$  ROIs acquired from  $n = 6$  cultures) samples, suggesting that the amount of  $\beta$ -tubulin III-positive fibers outgrowing from the slices is similar (Figure 2d), although differently scattered in the third dimension (Figure 2c).

In a recent work,<sup>[16]</sup> we showed that pure carbon nanotube 3D scaffolds, when interfaced to cultured spinal slices, shape

the neuronal processes extending from organotypic slices into a mesh-like structure, compared to bundled fasciculations that occur when slices are cultured interfaced to fibrin glue layered on 2D glass coverslips.<sup>[16]</sup> We perform a similar analysis here to further investigate if this reduction in fiber orientation is tied more closely to the porous nature of the substrate or directly to the presence of carbon nanotubes. When fiber directionality is assessed in terms of degree of angular dispersion,<sup>[16]</sup> we find no differences in the mean dispersion angle values of the two samples (average degree of dispersion:  $17^\circ \pm 2^\circ$  for PDMS,  $n = 28$  ROIs;  $16^\circ \pm 3^\circ$  for PDMS+CNT,  $n = 20$  ROIs; Figure 2e). The relatively high degree of dispersion ( $>15^\circ$ ) in both samples confirms our previous experiments<sup>[16]</sup> by indicating that, once interfaced to 3D structures, the majority of fibers are not oriented in “bundle-like” assemblies but, instead, they tend to form a random network.<sup>[16]</sup>

To summarize, both constructs support and attract neuronal process growth, as shown by the comparable  $\beta$ -tubulin III-positive area measured, but the presence of MWCNTs on the porous surface seems to limit, maybe by adhesion processes,



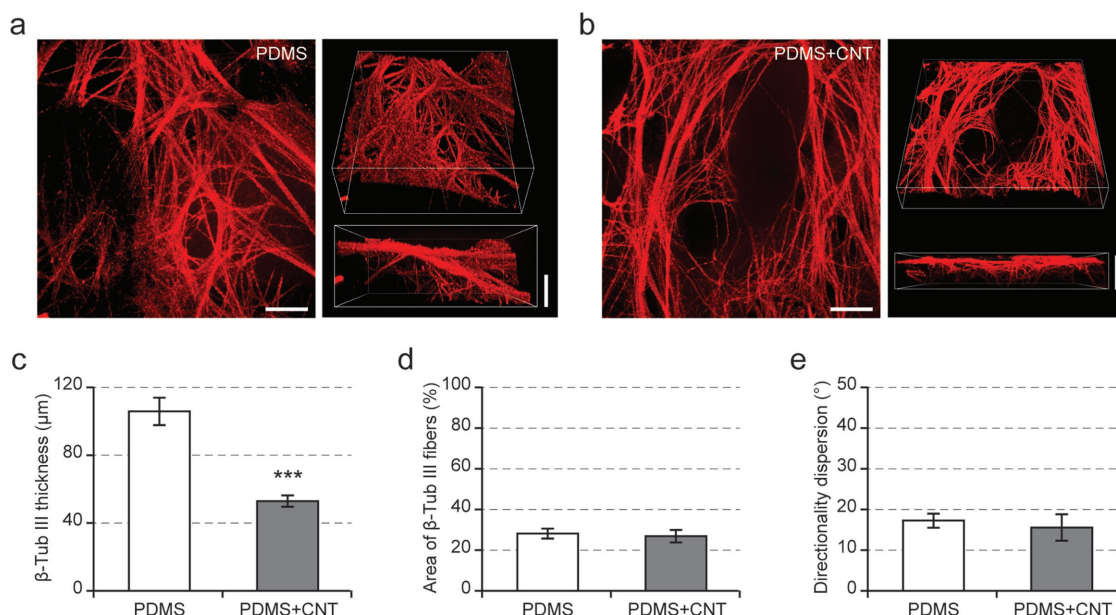


**Figure 2.** 3D distribution of neuronal processes extending from explanted spinal slices into PDMS or PDMS+CNT scaffolds.  $\beta$ -Tubulin III-positive neuronal processes form vast networks when cultured on a) 3D PDMS and b) 3D PDMS+CNT. Reconstruction of confocal image stacks permits visualization of the neurites as they penetrate the depth of the scaffolds (right panels in (a) and (b)). Scale bars: 50  $\mu$ m. c) Analysis of the depth through which  $\beta$ -tubulin III-positive processes penetrate the scaffolds. d) No differences were observed in  $\beta$ -tubulin III processes when evaluated as a percent of image area. e) The degree of directionality dispersion, a measure of neuronal fiber orientation, indicated no differences between processes developed on PDMS or PDMS+CNT supports.

the growth of neural fibers deep within the third dimension of the structure. Both porous constructs also favor the formation of intricate networks of variably oriented fibers, regardless the presence of MWCNTs, characterized by fewer thick, aligned bundles when compared to traditional 2D interfaces.<sup>[10,16]</sup>

### 2.3. Engineering PDMS Interfaces by Carbon Nanotubes Affects the Functional Rewiring of Segregated Spinal Explants

After characterizing the scaffolds' structure and the morphology of the neurite network infiltrating the structures upon interfacing spinal slices for >1 week, our primary interest is to investigate the in vitro effects of PDMS and PDMS+CNT interfaces on spinal network activity and their ability to promote functional reconnections between slice pairs.

Cultured spinal explants display prominent spontaneous electrical activity and well-characterized motor (ventral) outputs.<sup>[14,16]</sup> We monitored extracellular potentials (local field potentials, LFPs) by placing electrodes in the ventral regions of each slice (within 20–100  $\mu$ m of the ventral fissure; sketched in Figure 3a).

To examine the functional impact of interfacing slices with the two different materials, we use the glycine/GABA<sub>A</sub> receptor antagonists strychnine ( $1 \times 10^{-6}$  M) and bicuculline ( $20 \times 10^{-6}$  M) to weaken synaptic inhibition in PDMS and PDMS+CNT slice pairs ( $n = 13$  and  $n = 16$  cultures, respectively). These antagonists of inhibitory synapses are known to shift electrical motor outputs from random bursting to synchrony, as previously reported for the entire spinal cord<sup>[19]</sup> and for organotypic spinal slices,<sup>[20,21]</sup> leading, in all cultures tested, to the emergence of a slow-pace bursting (see sample tracings in Figure 3b).

A characterizing feature of spinal disinhibited rhythm is the frequency of bursting episodes that we quantified by measuring the interevent intervals (IEI). A direct comparison of IEI measured in the PDMS or PDMS+CNT constructs, reveals that the frequency distribution of IEI values is significantly shifted to the left in spinal slices cultured in the presence of carbon nanotubes ( $P < 0.001$ ; Figure 3c), the average IEI values being  $7.0 \pm 0.6$  s in PDMS+CNT ( $n = 28$  slices) and  $11.2 \pm 1.1$  s in PDMS ( $n = 23$  slices). Such an increase in rhythmic burst activity is reminiscent of the improved excitability usually detected when interfacing spinal slices to MWCNT carpets.<sup>[10]</sup> We can speculate that the MWCNTs exposed on the PDMS surfaces alter synaptic connectivity and/or firing activity in cultured slices,<sup>[10]</sup> possibly at the layer of neurons in direct contact to MWCNTs, affecting the excitability of the spinal networks.<sup>[10]</sup> However, we cannot exclude that the increased bursting activity is also reflecting an improved functional coupling among pairs of slices in the presence of carbon nanotubes. That is, when interfaced to PDMS+CNT, neuronal processes have more probability to interweave within the construct and to synapse to the cocultured spinal tissue, compared to those interfaced to PDMS alone. To clarify this issue, we further studied the functional connectivity between the two slices assessing, by cross-correlation analysis of the disinhibited bursting, the presence of synchronous ventral outputs.<sup>[15,16]</sup>

Ventral LFP recordings of disinhibited bursts were taken simultaneously from cocultured slices in PDMS or in PDMS+CNT (see Figure 3a for the experimental set-up and Figure 4a for an example of the recordings). We use a MATLAB algorithm<sup>[16]</sup> to calculate the Pearson cross-correlation coefficient (CCF) between the two cocultured slices and to determine

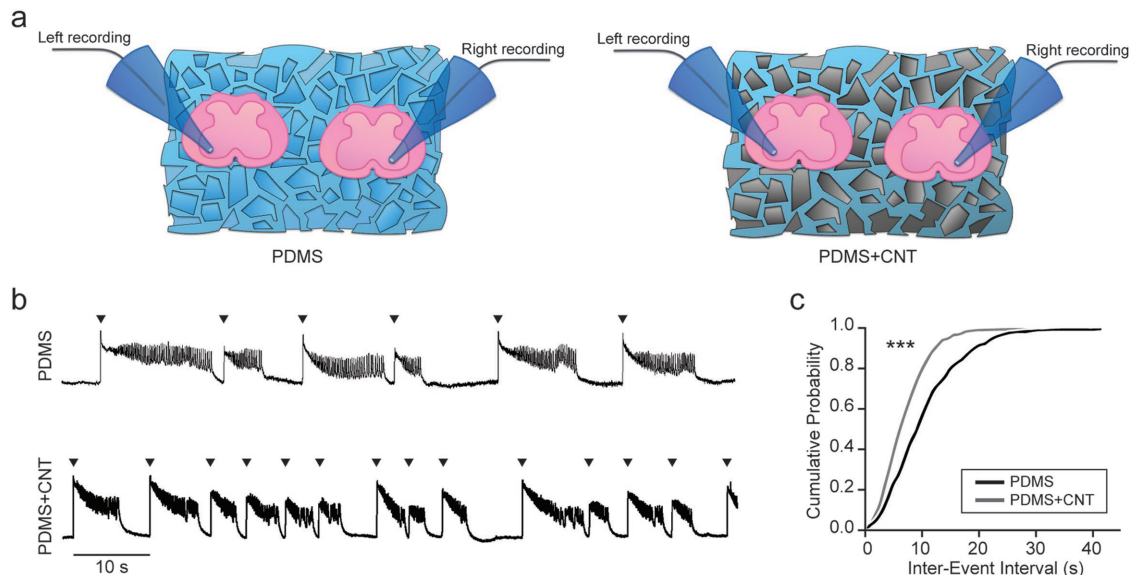


**Figure 3.** Electrophysiological activity of spinal slices on PDMS and PDMS+CNT scaffolds. a) Organotypic spinal slices were cultured as pairs on the surface of a 3D, microporous, PDMS scaffold (left) and of a PDMS+CNT (right) scaffold. Simultaneous extracellular recordings were taken from the ventral region of both slices. b) Representative traces depict the disinhibited bursting activity of the slices. Arrowheads represent onset of each burst. Inter-event interval (IEI—time interval between two subsequent black arrowheads) is shown and measured as the time between the onset of one burst and the beginning of the next. c) Relative cumulative frequency distributions of IEI values in slices grown in PDMS and in PDMS+CNT. For PDMS+CNT, the distribution of IEI values is significantly shifted to the left (K–S test;  $***P < 0.001$ ).

whether the CCF values obtained are significantly larger than that expected by chance, thus supporting the presence of functional contacts between the explants. An example of this analysis, performed for the recordings shown in Figure 4a, is shown by the plots of Figure 4b, where the distribution of CCFs obtained by randomly sampling the two time series in each experiment<sup>[16]</sup> is compared to the average CCF computed sampling consecutive time windows (the red line in the plots of Figure 4b). In PDMS+CNT, 81% of the recultured explants are correlated, displaying CCF values significantly larger than that expected by chance; on the contrary, in PDMS, correlated slices are detected only in 37.5% of samples (a significant difference;  $P < 0.05$ , Figure 4c). These results suggest that there are increased functional connections between the spinal slices interfaced with CNT-containing substrates, compared with those interfaced by PDMS alone. The low probability of reconnection in the PDMS interfaces is not surprising and is in line with our preliminary findings:<sup>[16]</sup> slices cultured side-by-side in pairs at distances known to inhibit functional reconnection in basal conditions<sup>[15,16]</sup> reconnect with a low probability even in the presence of 3D PDMS interfaces.<sup>[16]</sup> In our experiments, the average measured distance between slices is  $1.9 \pm 0.1$  mm for PDMS ( $n = 7$ ) and  $1.6 \pm 0.1$  mm for PDMS+CNT ( $n = 15$ ). The emergence of functional coupling is unrelated to the interslice distance (Figure 4d; note that filled symbols indicate functional correlated pairs measured as described above and in Figure 4b;  $r_{\text{PDMS+CNT}} = 0.30 \pm 0.30$ ,  $n = 15$ ;  $r_{\text{PDMS}} = 0.22 \pm 0.29$ ,  $n = 7$ ), as well as to the age in culture (sampled from 10 to 23 d; Figure 4e  $r_{\text{PDMS+CNT}} = 0.20 \pm 0.29$ ,  $n = 16$ ;  $r_{\text{PDMS}} = -0.08 \pm 0.29$ ,  $n = 8$ ).

Engineering PDMS 3D interfaces with MWCNTs effectively changes the efficacy of regenerating fibers to target and reconnect segregated explants. We also show an improved

electrophysiological performance that may favor the use of our substrates as regenerative interfaces.

In our previous study, we reported that when interfacing pairs of spinal explants to scaffolds, the improved directionality dispersion and the third dimensional outgrowth of neurites are needed to improve the fraction of reconnected pairs, regardless the amount of  $\beta$ -tubulin III-positive area.<sup>[16]</sup> However, 3D constructs, such as the PDMS interface used here, were not able to replicate the ability of pure 3D MWCNTs sponges<sup>[16]</sup> in reconnecting separated spinal slices by dispersed webs of axons, leaving unresolved what properties of the latter were making the difference: the tubular morphology and elastic properties of freestanding MWCNTs skeleton<sup>[16]</sup> or the physical and chemical properties of the MWCNT material in the third dimension?<sup>[12,16]</sup> Here we compare, for the first time, two PDMS-based interfaces exhibiting highly similar scaffold structures but for the presence of a layer of MWCNTs. We used PDMS elastomer since this material is a standard in microfabrication or microfluidics developments in biological applications, due to the PDMS simple manufacturing together with its gas permeability, optical transparency, flexibility.<sup>[22–24]</sup> In addition, this elastomer has been recently engineered in 2D devices showing excellent mechanical flexibility and leading to soft implants integrated in the subdural space.<sup>[25]</sup> PDMS has also been filled with MWCNTs using microcontact printing and casting mold techniques<sup>[26]</sup> to provide conductive PDMS patterns, with potential applications in biology. Here, by entrapment in the PDMS surface of nanofeatures such as carbon nanotubes, we have engineered an interfacing grid with the ability to direct the formation of reconnecting webs of neurites. The interactions among the geometry, chemistry, and the numerous physical and biological factors translating the exposure to

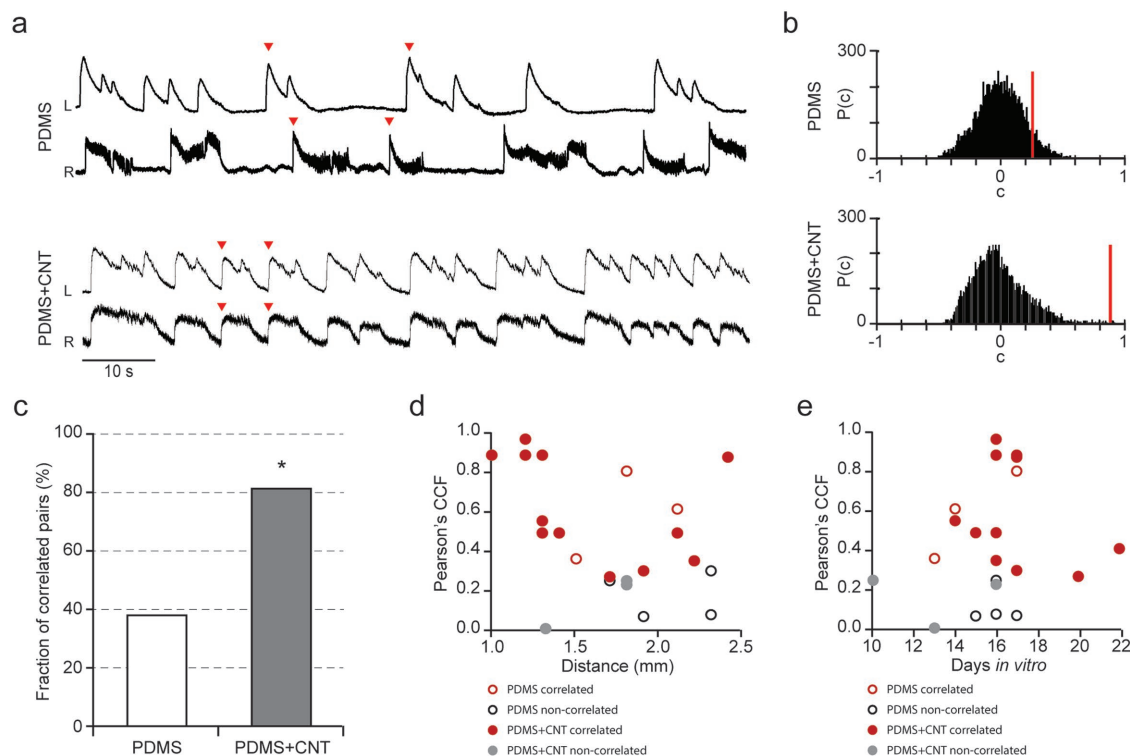


**Figure 4.** PDMS+CNT scaffolds promote functional reconnection between organotypic spinal slice pairs in vitro. a) Representative traces from simultaneous recordings of paired slices in PDMS (top) and PDMS+CNT (bottom), note the synchronous bursting in PDMS+CNT (left slice (L) right slice (R)). Red arrowheads indicate the onset of each burst in each slice. b) Histograms represent the null distribution<sup>[12]</sup> of individual CCF values obtained from time windows independently sampled for the left and right recordings of both conditions; the red line indicates the average value of the actual CCF of sampled traces. Plots refer to the two explicative traces shown in (a), and point to a significant synchronicity in PDMS+CNT traces (\*\* $P < 0.01$ ). c) The fraction of correlated pairs was significantly greater in slice pairs cultured on PDMS+CNT; \* $P < 0.05$ . d) Distance between slices was not correlated to CCF, indicating that distance had no effect on synchronous activity. e) Similar to distance, CCF did not correlate with the number of days in vitro of slice cultures.

MWCNTs into axonal regrowth and synapse formation are unknown. Interestingly, we found that neurites penetrated significantly greater depths into PDMS substrates compared with the PDMS+CNT substrates. We speculate that the presence of MWCNTs improves neurites mechanical tight associations with the interface, whereas in the case of PDMS, neurites tend to drop down into the pores following gravity, without associating with the material. That the neurite-MWCNT association is the rationale for the neuronal processes remaining within the first layers of the scaffold is supported by previous works which show that MWCNTs form extremely tight contacts with biological membranes.<sup>[8,10]</sup> We exclude large differences in the scaffolds' mechanical features, since in both PDMS and PDMS+CNT elasticity is due to the porosity of the structure.<sup>[7]</sup> In our previous study, we reported for similar porous scaffolds a Young's modulus within the range of that estimated in rodent and human brains.<sup>[7]</sup> Our in vitro results show that both scaffolds are of a mechanical stiffness conducive to neural tissue growth and sustainment.

We suggest the use of 3D PDMS scaffolds incorporated with MWCNTs as a potential candidate for manufacturing regenerating interfaces. The increasing application of nanomaterial-related technologies for engineering brain interfaces may thus ameliorate some intrinsic features of interfacing devices (such as the stability or the charge transfer to and from neurons),<sup>[27]</sup>

as well as their ability to facilitate recovery of function via guiding regenerating fibers.

#### 2.4. Biocompatibility of PDMS+CNT Implanted In Vivo

Toward further biomedical applications, any new device needs to be challenged with the biological milieu in vivo. Given the beneficial interactions in vitro of PDMS+CNT materials compared with PDMS-alone, in the last set of experiments we assess the tissue response to PDMS+CNT implantation in the cortex of adult rats.

The use of PDMS as inert polymer for generating implantable scaffolds is traditionally accepted<sup>[28]</sup> nonetheless advantages and limitations of any suitable material need to be evaluated when microfabrication technologies are designed for biological applications.<sup>[29]</sup>

Unfortunately, in our early observations, we detected a complete absence of interaction of the brain tissue with implanted PDMS scaffolds when not incorporating MWCNTs ( $n = 2$  animals; data not shown). In these animals, after 2 and 8 weeks (18 sections) postsurgery, the lack of integration of the PDMS scaffold with the surrounding cortical tissue is to an extent that the material no longer remains within the tissue following sectioning and subsequent histological processing for

immunofluorescence labeling. This makes it virtually impossible to quantify the response in the surrounding tissue at the immediate interface with the material; i.e., we cannot predict, for example, how much of the glial scar, is removed along with the implanted material during the tissue processing. These results were not entirely unexpected, as other studies have demonstrated a lack of PDMS integration with surrounding tissues when the PDMS material is not modified (such as via etching or the incorporation of adhesion molecules).<sup>[30,31]</sup> Because the in vitro results suggest that MWCNTs have a significant functional benefit over PDMS-alone substrates, we thus focused our biocompatibility study on the PDMS+CNT material.

We measured the surrounding microenvironment responses to PDMS+CNT implants, in particular we focus on the distribution patterns and infiltration of microglia together with astrocyte aggregation at the interface.<sup>[16,32–34]</sup>

Electrodes are common neural-implanted devices; extensive reporting in the literature illustrates that many, if not most,

implanted electrodes have reduced functionality over time due to the tissue response and glial scarring, an indicator of inadequate biocompatibility.<sup>[35–38]</sup> Glial scar formation typically occurs during the first 2–4 weeks following material insertion and is characterized by a dense reactive astrocyte and microglia region that can extend beyond 100  $\mu\text{m}$  from the implant.<sup>[35,36,38–40]</sup> This region can also undergo to relative neurodegeneration with a decrease in the number of local neurons.<sup>[35,36]</sup>

We implanted PDMS+CNT scaffolds into the adult rat visual cortex,<sup>[16]</sup> this allowed accessing large cortical surfaces while avoiding areas containing too many blood vessels. In addition, the choice of this region allowed effective comparisons of outcomes with our recent published work.<sup>[16]</sup> Rats were sacrificed at 2 weeks ( $n = 3$ ), 4 weeks ( $n = 3$ ), and 8 weeks ( $n = 3$ ) postimplantation. Brain tissue sections were immunolabeled for astrocytes and microglia (**Figure 5a,b**) using antibodies against glial fibrillary acidic protein (GFAP) and Iba1, respectively, to determine the level of tissue reactivity surrounding the implanted

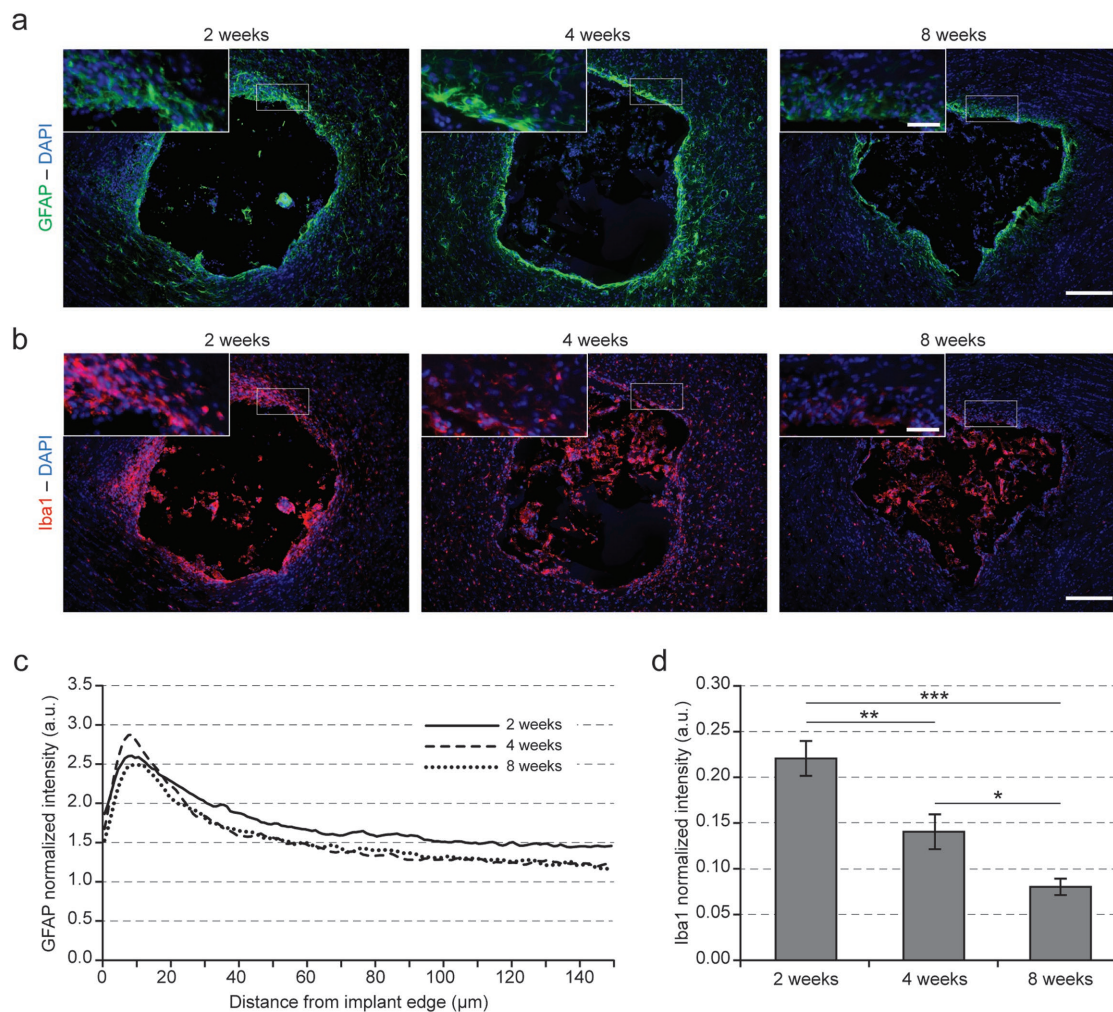


**Figure 5.** Neuroimmune response to implanted PDMS+CNT scaffolds indicated that the scaffolds were largely biocompatible in vivo. a) GFAP-positive astrocytes (green) were found in the cortex surrounding the PDMS+CNT implant at 2, 4, and 8 weeks postimplantation; (DAPI for nuclei is in blue). Boxed areas indicate magnified images shown in the insets. Scale bar: 200 and 50  $\mu\text{m}$  (inset). b) Iba1-positive microglia (red) were found surrounding the material as well as having infiltrated the scaffold; DAPI (blue). Boxed areas indicate magnified images shown in the insets. Scale bar = 200 and 50  $\mu\text{m}$  (inset). c) Increased GFAP immunoreactivity was observed primarily in the 50  $\mu\text{m}$  immediately proximal to the implant. d) Iba1-positive tissue immunoreactivity up to 500  $\mu\text{m}$  from the edge of the implant was found to significantly decrease over time; \* $P < 0.05$ , \*\* $P < 0.01$ , \*\*\* $P < 0.001$ .

material and any presence of a glial scar. Tissue sections were also immunolabeled with  $\beta$ -tubulin III and NeuN, to determine if any neurons were able to infiltrate the material.<sup>[16]</sup> Overall, the immunoreactivity of astrocytes and microglia surrounding the implanted material suggests a generally low immune response. In fact, as shown in Figure 5a, the increased GFAP immunoreactivity surrounding the implant is substantially limited to the first 50–60  $\mu\text{m}$  from the implant edge at all time points (quantified in Figure 5c). Further analysis reveals that, while the mean intensity up to 50  $\mu\text{m}$  from the implant is not different between the three time points investigated ( $P = 0.119$ ), the mean intensity up to 150  $\mu\text{m}$  (namely, to larger distances from the implant edge), of the GFAP fluorescence is significantly ( $P \leq 0.001$ ) lower in 4 and 8 weeks animals when compared to 2 weeks (2 weeks =  $1.73 \pm 0.02$  a.u., 4 weeks =  $1.55 \pm 0.02$  a.u., 8 weeks =  $1.57 \pm 0.03$  a.u.; Figure 5c). This suggests that, generally, the glial response in the surrounding tissue is likely decreasing when moving past the acute, inflammatory phase of the tissue reactivity. Regarding microglia cells, Iba1 immunoreactivity surrounding the implant (up to 500  $\mu\text{m}$ ) significantly decreases over time (Figure 5b,d). When measured, the average intensity is  $0.22 \pm 0.02$  a.u. at 2 weeks,  $0.14 \pm 0.02$  a.u. at 4 weeks;  $P = 0.004$  and  $0.08 \pm 0.01$  a.u. at 8 weeks ( $P \leq 0.001$  vs 2 weeks and  $P = 0.02$  vs 4 weeks). Iba1-positive microglia are observed to have infiltrated the implant material as early as 2 weeks postimplantation and continue to reside within the material at 8 weeks postimplantation.

Compared with other reports regarding the tissue response to cortical implants, we observe a general decrease in GFAP-positive astrocyte labeling from 2 to 8 weeks after implantation and, by 8 weeks postimplantation, limited to the area immediately surrounding the implanted material (Figure 5a).<sup>[36,37,40,41]</sup> In accordance with a reduction in inflammatory phase, there is a significant decrease in the intensity of Iba1-positive microglia labeling surrounding the implant over time. This is in contrast to the persistent upregulation of microglia associated with compromised biocompatibility and foreign body rejection often seen with implanted electrodes.<sup>[35–37,40–42]</sup> Interestingly, we observe Iba1 immunoreactivity inside the implanted material at all time-points (Figure 5b). It is interesting to note that an increased Iba1 immunoreactivity within MWCNTs, both when used as substrates<sup>[11]</sup> and as 3D scaffolds<sup>[16]</sup> has been observed before, without any indications that this increase is associated with an immune response. In vitro,<sup>[11]</sup> we observed an increase in Iba1-positive cell density in dissociated neural cells with an insubstantial immune response, while in vivo<sup>[16]</sup> the colonization of the material with native cells, as described here with the PDMS+CNT material, may sustain biocompatibility with neural tissue. Further research will be necessary to establish a thorough response profile and the true functionality of this material in vivo.

Additionally, in order to define whether the PDMS+CNT scaffold was fully integrated within the neural tissue, we investigated the presence of neurons within the material.<sup>[16]</sup> We observe  $\beta$ -tubulin III-positive neuronal processes (Figure 6a) permeating the 3D scaffold at the three time points studied (27%: 6 of 22 horizontal slices, 57%: 16 of 28 horizontal slices, and 44%: 8 of 18 horizontal slices at 2, 4, and 8 weeks post-implantation, respectively; Figure 6c). Therefore,  $\beta$ -tubulin

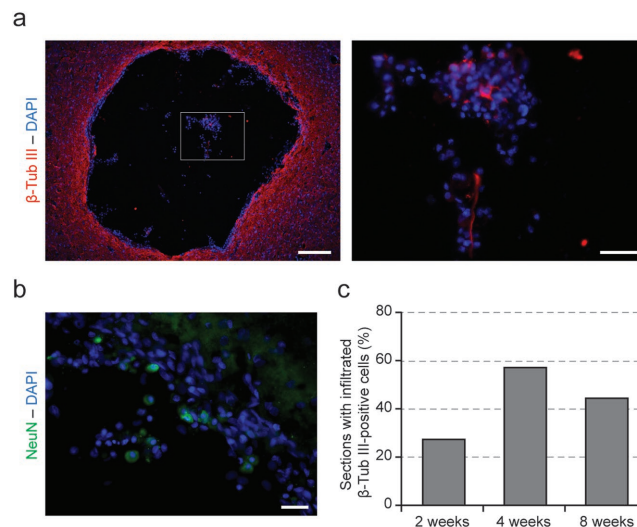


**Figure 6.** Neuronal infiltration of the PDMS+CNT scaffolds. a) Left: low magnification of PDMS+CNT implant in the cortex after 2 weeks, the finding of  $\beta$ -tubulin III-positive cells (in red; the boxed area is magnified in the right panel) within the scaffold suggests that astrocytes and microglia cells surrounding the implant do not represent a barrier for neuronal infiltration; DAPI (blue). Scale bar: 200  $\mu\text{m}$  (left) and 50  $\mu\text{m}$  (right). b) NeuN-positive neurons within the scaffold; DAPI (blue). Scale bar: 50  $\mu\text{m}$ . c)  $\beta$ -Tubulin III-positive cells invaded the implanted material as early as 2 weeks postimplantation and persisted at 4 and 8 weeks postimplantation.

III-positive cells invade the implanted material as early as 2 weeks postimplantation and their presence increases at later stages, though without reaching a statistical difference. In a subset of slices (2 animals, 2 weeks,  $n = 8$ ), we provide further evidence of infiltrated neuronal cells by exploiting the specific neuronal marker, NeuN.<sup>[16]</sup> In these experiments, we detect NeuN-positive neurons within the construct, as shown in an exemplifying image in Figure 6b. The presence of neuronal cells, perhaps migrating neuroblasts, within the implant is surprising, however is in agreement with our recent report describing NeuN-positive cells localized in implanted MWCNT-based scaffolds.<sup>[16]</sup> These findings, together with our previous work demonstrating very similar GFAP and Iba1 immunoreactivity in MWCNT-alone scaffolds,<sup>[16]</sup> confirm the MWCNTs-based materials as biocompatible 3D scaffolds and support their application as neural interfaces.

### 3. Conclusion

Controlled engineering of polymeric interfaces into 3D porous constructs favors the formation of intricate networks of variably oriented axons regrowing from the interfaced spinal tissues. The further incorporation of MWCNTs promotes the manufacturing of more efficient regenerating interfaces and guiding of regenerating axons to targets. Generally, the possibility to decorate elastomeric structures with nanomaterials implements the adhesion of axons to the interfacing devices and can be used to fabricate conductive pathways within a 3D construct. In this work, a novel 3D structure was interfaced to spinal explants in vitro and its biocompatibility was assessed in vivo. The

presented results hold the potential to exploit the use of 3D hybrids and carbon nanotubes in the area of (nano)engineering regenerative interfaces.

## 4. Experimental Section

**PDMS 3D Interface Fabrication:** 3D PDMS scaffolds are free-standing, porous structures made by PDMS (Sylgard 184, Dow Corning Co.), an elastomeric material commonly used in biomedical applications.<sup>[22–24,43]</sup> The fabrication procedures involve water dissolution of a sugar scaffold, resulting in a cast PDMS framework consisting of interconnected cavities as previously described.<sup>[7]</sup> In brief, 500 mg of food-approved sugar was passed through a No. 60 mesh sieve (Sigma-Aldrich) and mixed with 20  $\mu\text{L}$  of deionized water, placed in a silicon mold, and subsequently dried at 65  $^{\circ}\text{C}$  for 30 min. PDMS was vacuum-forced to percolate inside the resulting sugar framework until all spaces were filled, and cured in an oven at 85  $^{\circ}\text{C}$  for 1 h. After cooling, the sugar was dissolved by submersing the sample in distilled water overnight. The water-driven dissolution of sugar grains produces a network of interconnected micro-pores inside the PDMS scaffold.

MWCNTs, 20–30 nm in diameter (Nanostructured & Amorphous Materials, Inc.), were prepared as previously reported,<sup>[9]</sup> briefly MWCNTs were functionalized using 1,3-dipolar cycloaddition with heptanal and sarcosine at 180  $^{\circ}\text{C}$  for 24 h in *o*-dichlorobenzene as solvent. MWCNTs were incorporated in PDMS scaffolds by mixing functionalized MWCNTs (15 mg) with the sugar (500 mg, sifted as described above). Before use, scaffolds were sonicated in distilled water for 20 min, dehydrated in ethanol solution (99.5%), and dried in an oven at 65  $^{\circ}\text{C}$  for 2 h. Scaffold layers of about 5  $\times$  5 mm<sup>2</sup> in lateral dimensions and 300  $\mu\text{m}$  in thickness were extracted from the bulky material using a vibratome (Leica VT 1000S, Leica Biosystems) and mounted on thin glass coverslips (24  $\times$  12  $\times$  0.2 mm<sup>3</sup>) using PDMS (Sylgard 184, Dow Corning Co.).

Prior to use, PDMS and PDMS+CNT substrates were treated with low-pressure air plasma for 5 min at high power using a PDC-32G Plasma Cleaner (Harrick Plasma) and sterilized under UV light for 20 min. PDMS is characterized by pronounced hydrophobicity—the major drawback for use of the material for *in vitro* and *in vivo* applications—which was addressed by an oxygen plasma treatment. This treatment turns the PDMS surface hydrophilic by introducing hydroxyl groups en masse to the surface.<sup>[22]</sup>

**Synchrotron Radiation (SR) Computed Microtomography and Scanning Electron Microscopy (SEM):** To characterize 3D PDMS and PDMS+CNT scaffolds, computed microtomography ( $\mu\text{CT}$ ) studies were performed. X-ray  $\mu\text{CT}$  experiments were carried out at the SYRMEP beamline of the ELETTRA synchrotron light source (Trieste, Italy). In order to enhance the image contrast, a single distance phase retrieval preprocessing algorithm<sup>[44]</sup> was applied to the CT projections, prior to the reconstruction procedure based on the standard Filtered Back Projection approach. The experiment was done in the white beam configuration mode with a polychromatic spectrum. Filters were applied for low energies (1 mm of aluminum) resulting in a hardened beam with average beam energy of 22 keV. The detecting system consisted in a sCMOS chip-based camera, placed at 10 cm away from the sample, and coupled with a high numerical aperture optic so the resulting pixel size was set to 0.9  $\mu\text{m}$ . Each dataset consists in 1800 projections covering a total angle range of 180 $^{\circ}$  with an acquisition time of 0.25 s per projection. The application of the tomographic method provides the benefit of reconstructing, in a nondestructive manner, the complex 3D organization of pores and channels inside the material and to provide a map of the void spaces. 3D volumes were obtained reconstructing the series of 2D projections using the STP (SYRMEP Tomo Project) software<sup>[45]</sup> and then analysis was performed with Pore3D software library.<sup>[46]</sup> The porous matrix was evaluated in terms of number and dimension of pores and throats, connectivity density, and anisotropy index.<sup>[47]</sup> Pore and throat numbers and size distributions were obtained following a skeleton analysis<sup>[48]</sup> and using the concept of maximal

inscribed sphere, while connectivity density, a simple global measure of connectivity which gives higher values for better-connected structures and lower values for poorly connected structures, was evaluated finding the Euler characteristic.<sup>[47]</sup>

PDMS and PDMS+CNT scaffolds morphologies were assessed via SEM. Images were acquired collecting secondary electrons on a Gemini SUPRA 40 SEM (Carl Zeiss NTS GmbH, Oberkochen, Germany). Bare scaffolds were mounted on conductive double side carbon tape (Ted Pella, Inc., USA) and imaged at 5 keV. Prior to SEM characterization samples were metalized with a thin layer of gold (<10 nm) using a metal sputter coater (Polaron SC7620).

**Organotypic Spinal Cord Slice Preparation and Culture:** Organotypic slice cultures were obtained as previously described.<sup>[10]</sup> Briefly, embryos at embryonic day 12 (E12), were isolated from timed-pregnant mice (C57Bl) euthanized by CO<sub>2</sub> overdose and decapitation. Spinal columns were isolated and the low thoracic to high lumbar regions were dissected away from the surrounding tissue. This tissue was sliced by tissue-chopper transversely (275  $\mu\text{m}$ ) and further isolated the spinal cord and dorsal root ganglia tissue. Spinal cord slices were placed in cold GBSS and refrigerated for 1 h prior to placement on the substrates. Pairs of spinal cord slices were embedded into a thick matrix of chicken plasma (Rockland) and thrombin (Sigma) clot and placed upon the PDMS and PDMS+CNT substrates the distance between the slice pairs being within the range of 1.0–2.5 mm (interslice distance measured from center of the two slices); slice pairs not falling within this distances were discarded. The specified distance was necessary to ensure homogeneity in experimental conditions between the two populations (PDMS and PDMS+CNT) for electrophysiological and immunofluorescence experiments. Slice pairs were cultured for 10–22 d *in vitro* (DIV) in plastic Nunc tubes with 1.5 mL medium containing 67% Dulbecco's modified Eagle medium (DMEM) (Invitrogen), 8% sterile water for tissue culture, 25% fetal bovine serum (Invitrogen), and 25 ng mL<sup>-1</sup> nerve growth factor (Alomone Laboratories); osmolarity, 300 mOsm; pH 7.35. The tubes were kept in a roller drum rotating 120 times per hour at 37  $^{\circ}\text{C}$  in humidified conditions with 5% CO<sub>2</sub>.

**Electrophysiological Recordings and Analysis:** Organotypic slice cultures at >10 DIV were mounted in a Perspex recording chamber, installed on an upright microscope (Leica DM LFS) with a continuous superfusion of control physiological saline solution containing (in mM): 152 NaCl, 4 KCl, 1 MgCl<sub>2</sub>, 2 CaCl<sub>2</sub>, 10 HEPES, and 10 Glucose; pH adjusted to 7.4 with NaOH. Simultaneous extracellular recordings were obtained at room temperature (RT; 20–22  $^{\circ}\text{C}$ ) using low resistance glass micropipettes (4–6 M $\Omega$ ) filled with 20  $\times$  10<sup>-3</sup> M KCl saline solution. The electrodes were advanced manually using micromanipulators (Luigs and Neumann SM1, Germany) into the ventral region in both slices. Voltage LFP, as a consequence of synaptic activity and action potential firing, were recorded in regions 20–100  $\mu\text{m}$  from the ventral fissure.<sup>[23,43]</sup> The recorded signals were amplified with the offset neutralized manually through the amplifier by current injection (Axopatch 1D; Axon Instruments). Signal recordings were acquired using the Clampex 8.2 software (pClamp suite, Axon Instruments) and digitized at 10 kHz (Digidata 1322A, Axon Instruments), filtered lowpass at 2 kHz. Strychnine and bicuculline (1  $\times$  10<sup>-6</sup> and 20  $\times$  10<sup>-6</sup> M, respectively) were administered into the bath to induce disinhibited rhythmic bursting.<sup>[49]</sup> Disinhibited bursts were evaluated by mean interevent interval analysis (the time between the onset of each burst;  $\geq$ 20 bursts were used for each measure).

Disinhibited burst LFPs obtained from each spinal slice were lowpass filtered at 3 Hz and the data reduced and imported to MATLAB.<sup>[16]</sup> The synchrony was further assessed between the bursting activities of the two explants in each pair by computing the Pearson correlation coefficient between the two voltage time series. The statistical significance of the correlation coefficient was determined by performing a permutation test,<sup>[16]</sup> that allowed to measure the distribution of correlation coefficients that one would expect to observe if the voltage signals recorded from a pair of explants happened to correlate purely by chance. By measuring how likely it was for the values of this null distribution to be larger or equal than the real correlation coefficient,

it was possible to understand whether the correlation between the pair of time series was significantly larger than expected by chance. This procedure allowed for determining what fraction of cocultured slices exhibited a significantly synchronous bursting activity, for all the tested conditions. A full amelioration of the cross-correlation analysis can be found in Usmani et al.<sup>[16]</sup> The fraction of significantly correlated pairs ( $P < 0.05$ ) was compared between PDMS and PDMS+CNT groups by performing a chi-squared test for homogeneity.

**Spinal Culture Immunohistochemistry:** Following electrophysiological recordings, organotypic spinal slices were fixed at room temperature for 1 h in 4% formaldehyde (prepared from fresh paraformaldehyde, PFA) in phosphate-buffered saline (PBS) (Sigma) then washed with PBS. Samples were treated with 0.1 M glycine in PBS for 5 min to quench free aldehyde groups. Samples were incubated for 30 min in protein blocking solution (5%, bovine serum albumin (BSA), Sigma-Aldrich, 0.3% Triton X-100, Carlo Erba, 1% Fetal Bovine Serum, Gibco in PBS). Subsequently, samples were incubated with the primary antibodies, rabbit anti- $\beta$ -tubulin III (polyclonal, Sigma-Aldrich Cat# T2200, RRID: AB\_262133; used at 1:200) prepared in PBS with 5% fetal bovine serum (FBS) at 4 °C, overnight. After thorough washing in PBS, samples were incubated in secondary antibodies: goat anti-rabbit AlexaFluor 594 (polyclonal, Thermo Fisher Scientific Cat# R37117, RRID: AB\_2556545; used at 1:500) and labeled with 4',6-diamidino-2-phenylindole, diacetate (DAPI; monochemical, Thermo Fisher Scientific Cat# D3571, RRID: AB\_2307445; used at 1:500) prepared in PBS with 5% FBS at room temperature for 2 h. Following secondary antibody incubation, samples were rigorously washed in PBS and briefly with water before mounting on glass coverslips using Vectashield mounting medium (Vector laboratories).

**Spinal Culture Imaging and Analysis:** Images of immunolabeled organotypic spinal slice pairs were acquired using a Leica DM6000 epifluorescence microscope using a 2.5 $\times$  dry objective. This low magnification allowed for visualizing both slices in the same field in order to identify slice location and to measure interslice distance. Further, a Nikon C2 confocal microscope was used to acquire higher quality images of the neurites spreading 3D into the substrate (40 $\times$  oil objective, N.A. 1.3, oil mounting medium R.I. 1.515). The total stack thickness was set in order to obtain all  $\beta$ -tubulin III-positive processes from the sample with a z-step of 1  $\mu$ m. Analysis and 3D reconstruction of the image stack was accomplished using NIS-Elements AR software (Nikon), Volocity (PerkinElmer), and the open source image processing package, Fiji (<http://fiji.sc/Fiji>).

Assessment of any differences in the 3D distribution of neuronal processes on PDMS and PDMS+CNT substrates was evaluated by considering image stacks taken from regions central (area between slices) and peripheral (at the substrate edge) to the slices. Utilizing the Fiji processing software, the thickness through which the  $\beta$ -tubulin III signal was present (indicating neural process extension) was measured and compared between PDMS and PDMS+CNT samples.

To measure the density of outgrowing  $\beta$ -tubulin III-positive neuronal fibers on PDMS and PDMS+CNT scaffolds, similar image stacks, as described above, with a z-step of 2  $\mu$ m, were used. The Fiji software was used to measure the intensity of  $\beta$ -tubulin III-positive labeling of neuronal processes surrounding the spinal slice. The background intensity for each image was defined automatically by the software. The signal-positive area above the background threshold intensity was recorded to define the area of the image (depicted as a percentage of the total image area) positive for neuronal fibers (28 randomly sampled images from  $n = 10$  PDMS samples; 20 images from  $n = 6$  PDMS+CNT samples).

The alignment of fibers emerging from the spinal slices was quantified in terms of relative orientation by means of fiber directionality analysis [see ref. [16] for detailed methods]. This was carried out using the Directionality plugin of Fiji software. Fourier component analysis is executed to identify orientation of "structures;" in our case  $\beta$ -tubulin III immunolabeled neuronal processes. Confocal images measuring 640  $\times$  640  $\mu$ m<sup>2</sup> were used to compute mean fiber direction and the degree of dispersion (29 randomly sampled images from  $n = 10$  PDMS samples; 20 images from  $n = 6$  PDMS+CNT samples).

**In Vitro Data Statistical Analysis:** For all in vitro data, results are depicted as mean  $\pm$  SE of the mean, unless otherwise stated; statistically significant differences between datasets were assessed using Statistica software (StatSoft, Inc.). Student's  $t$  test (after validation of variance homogeneity by Levene's test) was used for parametric data, Mann-Whitney test for nonparametric data; results were further confirmed using MATLAB (<http://www.mathworks.com>). Differences in the relative cumulative frequency distribution were obtained using the paired Kolmogorov-Smirnov (K-S) test. Chi-squared method analysis was performed for estimating significantly synchronous slices in the two groups (PDMS and PDMS+CNT) based on results obtained by the use of MATLAB. Statistical significance was established at  $P < 0.05$ .

**In Vivo Implantation of PDMS+CNT Scaffold:** All surgical procedures were performed on Wistar male rats (Harlan Laboratories;  $n = 9$ , three animals per time point), 3–6 months of age and weighing 450–550 g. Anesthesia was induced with isoflurane (2% in 100% O<sub>2</sub>, Sigma-Aldrich) administered via a nose cone and maintained throughout the procedure. Anesthetic depth was monitored by checking the absence of tail and paw reflexes. The anesthetized animal was placed in a stereotaxic apparatus (Narishige SR-5R) and body temperature was maintained at 37 °C with a thermostatically controlled heating pad (temperature control unit HB 101/2; Panlab/Harvard Apparatus) to avoid anesthesia-induced hypothermia. Heart rate and oxygen saturation level were monitored via a pulse oxymeter (Pulsesense LS1P-10R, Nonin Medical Inc., Medair AB).

The implant consisted of a sharp-pointed cylinder ( $\approx$ 2 mm in length and 0.5  $\pm$  0.2 mm in diameter) carved out from a larger PDMS+CNT scaffold using a razor-blade and mounted on an electrode holder (ZIF-Clip, Tucker-Davis Technologies).<sup>[16]</sup> Implant stiffness was increased via polyethylene glycol (PEG-8000, Sigma-Aldrich) scaffold permeation after the carving procedure to facilitate subsequent insertion of the material into the brain tissue.

A square, 2  $\times$  2 mm<sup>2</sup> craniotomy was performed over the left hemisphere using a microdrill and the dura mater was removed, exposing the brain. Tissue adhesive (B. Braun Aesculap, Germany) was applied on the inner perimeter of the craniotomy to prevent brain dimpling. The coordinates for implantation of the PEG-stiffened PDMS+CNT implant were A-P  $-4.5$  mm from Bregma and M-L  $-3.5$  mm and relate to the visual cortex (specifically the cortical junction between V2ML and V1)<sup>[50]</sup> in the adult rat. The scaffold was inserted via a microdrive at a speed of about 0.5 mm s<sup>-1</sup> to a depth of  $\approx$ D-V 2 mm until the material was completely within the cortical tissue. The high speed of insertion is necessary to prevent premature melting of the PEG. The craniotomy was filled with silicone (Kwik-Cast&Kwik-sil, World Precision Instrument) in order to isolate the exposed brain tissue and the skull surface covered by bone cement (Super Bond, C&B).

Throughout the procedure, the animal's eyes and cortex were periodically irrigated using an ophthalmic solution (Epigel, CevaVetem) and a 0.9% NaCl saline solution, respectively. Atropine (1.5 mg kg<sup>-1</sup>) and lactated Ringer's solution (1 mL) were administered subcutaneously every hour to reduce secretions and maintain homeostasis. Analgesic solution (Rymadyl; 5 mg kg<sup>-1</sup>, intraperitoneal) and antibiotic (Baytril; 5 mg kg<sup>-1</sup>, intramuscular) were administered to the rat via injection immediately before the surgery and 1 h prior to the end of the surgical procedure. Both solutions were administered following surgery via the animals' drinking water for 3 d postsurgery. Animals were monitored for recovery immediately after the surgery and at least three times per day for the first 72 h. A general distress-scoring sheet (Institutional Standards for the Care and Use of Animals in Research and after consulting with a veterinarian) was used to assess pain and distress in animals using physiological (appearance) and behavioral (natural and provoked behavior) parameters. For each parameter, a numerical score starting from 0 = normal, and reaching 3 = grossly abnormal, was determined. An extra point was added for each 3 given. The provoked behavior was tested after the first 72 h postimplantation. This method allows an objective monitoring of animals general conditions, to evaluate the need of analgesics or euthanization. All the animals used in the study did not show any sign of pain or distress (score = 0). Following

this 72 h period, animals were monitored once per day until sacrifice. Animals were sacrificed at 2, 4, and 8 weeks postimplantation.

**Brain Tissue Preparation and Immunohistochemistry:** At the selected time points (2, 4, and 8 weeks postimplantation) animals were anesthetized with 5% chloral hydrate (7 mL kg<sup>-1</sup>) and perfused transcardially with 0.1 M PBS followed by 4% paraformaldehyde in PBS. Brains were removed, postfixed for 24 h at 4 °C in 4% PFA, and cryoprotected in 15% sucrose in PBS at 4 °C for 24 h and subsequently in 30% sucrose in PBS at 4 °C for at least 24 h. Brains were embedded in optimal cutting temperature compound (Tissue-Tek), frozen at -20 °C, and sectioned at 25 μm horizontally onto SuperFrost-Plus slides (Thermo Scientific) using a cryostat.

Tissue-Tek was removed by PBS washing and tissue sections were protein-blocked in 3% BSA, 3% FBS, 0.3% Triton X-100 in PBS for 30 min at room temperature. For primary antibody labeling, sections were incubated overnight at 4 °C with mouse anti-GFAP (monoclonal, Sigma-Aldrich Cat# G3893, RRID: AB\_477010; used at 1:200), rabbit anti-ionized calcium-binding adapter molecule 1 (Iba1; polyclonal, Wako Cat# 019-19741, RRID: AB\_839504; used at 1:400), rabbit anti-β-tubulin III (1:250, Sigma), and/or mouse antineuronal nuclei (NeuN; polyclonal, Millipore Cat# MAB377, RRID: AB\_2298772; used at 1:100) in 5% FBS in PBS. After washing in PBS, sections were incubated in secondary antibodies goat anti-rabbit AlexaFluor 594 (polyclonal, Thermo Fisher Scientific Cat# R37117, RRID: AB\_2556545; used at 1:500) and goat anti-mouse AlexaFluor 488 (polyclonal, Thermo Fisher Scientific Cat# A-11029, RRID: AB\_2534088; used at 1:500) in 5% FBS in PBS for 2 h at room temperature. Following final washing with PBS and water, tissue sections were covered with glass coverslips using Vectashield hard mounting medium with DAPI (Vector Laboratories).

**Brain Tissue Image Acquisition and Analysis:** Immunoreactivity of the brain to the implanted material was measured by labeling tissue sections for reactive astrocytes and microglia using antibodies against GFAP and Iba1, respectively. Antibodies against β-tubulin III and NeuN were used to visualize neurons that may have infiltrated the scaffold. Fluorescence images were acquired using a Leica DM6000 upright microscope. In order to quantify GFAP and Iba1 labeling, a 10× dry objective was used to take images surrounding the entirety of the implanted material. Higher magnifications were used to take detailed images for observation of cellular infiltration. Image analysis was performed using FIJI software.

For GFAP intensity measurements, 24 intensity profile lines were drawn at random intervals around the implanted material, starting from the edge of the implant and extending 500 μm into the surrounding tissue, as previously shown.<sup>[16]</sup> These lines produced a fluorescence intensity profile as a function of distance from the implant edge. To account for variations in labeling, an image of the contralateral hemisphere in the same anatomical region as the implanted material was taken at 10× and used to define the background intensity for each section (the fluorescence intensity was measured with 9 randomly placed intensity profile lines). In each tissue section, GFAP intensity values at each micrometer were calculated for 0–150 μm from the implant edge, normalized to the average intensity for the contralateral hemisphere, and finally averaged across all sections ( $n \geq 7$ ) for each animal to create a mean intensity profile. Because differences in GFAP intensity were observed to be within 50 μm from the implant, for each animal the data from 0 to 150 μm were further normalized to the average intensity measured at 51–150 μm from the edge of the implant; these data were used for statistical analyses.<sup>[16]</sup>

For Iba1 intensity measurements,  $n = 8$  ROIs (100 × 500 μm<sup>2</sup>) were selected starting from the edge of the implant and extending 500 μm into the surrounding tissue.<sup>[16]</sup> The background intensity threshold was defined for each section using the Iba1 labeling intensity measured in the contralateral hemisphere in the same anatomical region as the implanted material. The area within each ROI with intensity above the background threshold was calculated and used for statistics. The ROI for all sections were averaged for each animal and are depicted as the mean ± standard error of the mean (SEM).

Statistical analysis was performed using Statistica software (StatSoft, Inc.). One-way analysis of variance (one-way ANOVA) was used to

determine statistical significance at  $P < 0.05$ , with posthoc analysis performed using the Fisher's least significant difference (Fisher's LSD) method to compare datasets.

**Ethics Statement:** This study was carried out in accordance with the recommendations in the Guide for the Care and Use of Laboratory Animals of the National Institutes of Health and the appropriate international and institutional standards for the care and use of animals in research (Italian Ministry of Health, in agreement with the EU Recommendation 2007/526/CE). The protocols and all performed experiments are approved by the local veterinary service and the institutional (SISSA) ethical committee, in accordance with the EU guidelines (2010/63/UE) and Italian law (decree 26/14). All efforts were undertaken to minimize pain and suffering of the animals and to reduce the number of animals used.

## Acknowledgements

E.R.A. and S.U. contributed equally to this work. The authors thank the IOM-TASC (Trieste) for SEM assistance. The authors acknowledge the PRIN-MIUR No. 2012MYESZW, and the ByAxon No. 737116 to L.B. M.P., as the recipient of the AXA Chair, is grateful to the AXA Research Fund for financial support. M.P. was also supported by the Spanish Ministry of Economy and Competitiveness MINECO (Project No. CTQ2016-76721-R), the University of Trieste, and the Diputación Foral de Gipuzkoa program Red (101/16).

## Conflict of Interest

The authors declare no conflict of interest.

## Keywords

3D X-ray microtomography, carbon nanotubes, elastomeric scaffolds, electrophysiology, organotypic cultures, spinal cord

Received: January 30, 2017

Revised: April 7, 2017

Published online:

- [1] U. Chaudhary, N. Birbaumer, A. Ramos-Murguialday, *Nat. Rev. Neurol.* **2016**, *12*, 513.
- [2] J. P. Harris, D. J. Tyler, *Crit. Rev. Biomed. Eng.* **2013**, *41*, 435.
- [3] C. H. Thompson, M. J. Zoratti, N. B. Langhals, E. K. Purcell, *Tissue Eng., Part B* **2016**, *22*, 125.
- [4] H. I. Chen, D. Jgamadze, M. D. Serruya, D. K. Cullen, J. A. Wolf, D. H. Smith, *Front. Syst. Neurosci.* **2016**, *10*, 1.
- [5] R. Green, M. R. Abidian, *Adv. Mater.* **2015**, *27*, 7620.
- [6] X. Duan, C. M. Lieber, *Chem. - Asian J.* **2013**, *8*, 2304.
- [7] S. Bosi, R. Rauti, J. Laishram, A. Turco, D. Lonardoni, T. Nieuw, M. Prato, D. Scaini, L. Ballerini, *Sci. Rep.* **2015**, *24*, 9562.
- [8] G. Cellot, E. Cilia, S. Cipollone, V. Rancic, A. Sucapane, S. Giordani, L. Gambazzi, H. Markram, M. Grandolfo, D. Scaini, F. Gelain, L. Casalis, M. Prato, M. Giugliano, L. Ballerini, *Nat. Nanotechnol.* **2009**, *4*, 126.
- [9] G. Cellot, F. M. Toma, Z. K. Varley, J. Laishram, A. Villari, M. Quintana, S. Cipollone, M. Prato, L. Ballerini, *J. Neurosci.* **2011**, *31*, 12945.
- [10] A. Fabbro, A. Villari, J. Laishram, D. Scaini, F. M. Toma, A. Turco, M. Prato, L. Ballerini, *ACS Nano* **2012**, *6*, 2041.
- [11] A. Fabbro, A. Sucapane, F. M. Toma, E. Calura, L. Rizzetto, C. Carrieri, P. Roncaglia, V. Martinelli, D. Scaini, L. Masten,



- A. Turco, S. Gustincich, M. Prato, L. Ballerini, *PLoS One* **2013**, *8*, e73621.
- [12] V. Lovat, D. Pantarotto, L. Lagostena, B. Cacciari, M. Grandolfo, M. Righi, G. Spalluto, M. Prato, L. Ballerini, *Nano Lett.* **2005**, *5*, 1107.
- [13] A. Mazzatenta, M. Giugliano, S. Campidelli, L. Gambazzi, L. Businaro, H. Markram, M. Prato, L. Ballerini, *J. Neurosci.* **2007**, *27*, 6931.
- [14] D. Avossa, M. D. Rosato-Siri, F. Mazzaro, L. Ballerini, *Neuroscience* **2003**, *122*, 391.
- [15] M. Heidemann, J. Streit, A. Tschertner, *Neuroscience* **2014**, *262*, 40.
- [16] S. Usmani, E. R. Aurand, M. Medelin, A. Fabbro, D. Scaini, J. Laishram, F. B. Rosselli, A. Ansuini, D. Zoccolan, M. Scarselli, M. De Crescenzi, S. Bosi, M. Prato, L. Ballerini, *Sci. Adv.* **2016**, *2*, e1600087.
- [17] B. H. Gähwiler, S. M. Thompson, D. Muller, *Curr. Protoc. Neurosci.* **2001**, *6*, 6.11.
- [18] F. J. O'Brien, *Mater. Today* **2011**, *14*, 88.
- [19] E. Bracci, L. Ballerini, A. Nistri, *J. Neurosci.* **1996**, *16*, 7063.
- [20] L. Ballerini, M. Galante, *Eur. J. Neurosci.* **1998**, *10*, 2871.
- [21] J. Streit, *J. Neurophysiol.* **1993**, *70*, 871.
- [22] J. Zhou, D. A. Khodakov, A. V. Ellis, N. H. Voelcker, *Electrophoresis* **2012**, *33*, 89.
- [23] K. J. Regehr, M. Domenech, J. T. Koepsel, K. C. Carver, S. J. Ellison-Zelski, W. L. Murphy, L. A. Schuler, E. T. Alarid, D. J. Beebe, *Lab Chip* **2009**, *9*, 2132.
- [24] R. N. Palchesko, L. Zhang, Y. Sun, A. W. Feinberg, *PLoS One* **2012**, *7*, e51499
- [25] I. R. Mineev, P. Musienko, A. Hirsch, Q. Barraud, N. Wenger, E. M. Moraud, J. Gandar, M. Capogrosso, T. Milekovic, L. Asboth, R. F. Torres, N. Vachicouras, Q. Liu, N. Pavlova, S. Duis, A. Larmagnac, J. Vörös, S. Micera, Z. Suo, G. Courtine, S. P. Lacour, *Science* **2015**, *348*, 159.
- [26] C. X. Liu, J. W. Choi, in *Conf. Proc. IEEE Engineering in Medicine and Biology Society*, IEEE, Piscataway, NJ **2009**, p. 6391.
- [27] P. Fattahi, G. Yang, G. Kim, M. R. Abidian, *Adv. Mater.* **2014**, *26*, 1846.
- [28] J. W. Han, K. Beomseok, L. Jing, M. Meyyappan, *Appl. Phys. Lett.* **2013**, *102*, 051903
- [29] E. Berthier, E. W. Young, D. Beebe, *Lab Chip* **2012**, *12*, 1224.
- [30] C. P. Pennisi, V. Zachar, L. Gurevich, A. Patriciu, J. J. Struijk, in *Conf. Proc. IEEE Engineering in Medicine and Biology Society*, IEEE, Piscataway, NJ **2010**, p. 3804.
- [31] Y. Lu, D. Wang, T. Li, X. Zhao, Y. Cao, H. Yang, Y. Y. Duan, *Biomaterials* **2009**, *25*, 4143.
- [32] K. Zhou, S. Motamed, G. A. Thouas, C. C. Bernard, D. Li, H. C. Parkington, H. A. Coleman, D. I. Finkelstein, J. S. Forsythe, *PLoS One* **2016**, *11*, e0151589.
- [33] E. R. Aurand, J. Wagner, C. Lanning, K. B. Bjugstad, *J. Funct. Biomater.* **2012**, *3*, 839.
- [34] E. Fournier, C. Passirani, C. N. Montero-Menei, J. P. Benoit, *Biomaterials* **2003**, *24*, 3311.
- [35] G. C. McConnell, H. D. Rees, A. I. Levey, C. A. Gutekunst, R. E. Gross, R. V. Bellamkonda, *J. Neural Eng.* **2009**, *6*, 056003.
- [36] B. D. Winslow, M. B. Christensen, W. K. Yang, F. Solzbacher, P. A. Tresco, *Biomaterials* **2010**, *31*, 9163.
- [37] S. M. Gutowski, K. L. Templeman, A. B. South, J. C. Gauding, J. T. Shoemaker, M. C. LaPlaca, R. V. Bellamkonda, L. A. Lyon, A. J. García, *J. Biomed. Mater. Res., Part A* **2014**, *102*, 1486.
- [38] V. S. Polikov, P. A. Tresco, W. M. Reichert, *J. Neurosci. Methods* **2005**, *148*, 1.
- [39] A. A. Turner, M. Bouffard, H. C. Lukaski, *Int. J. Circumpolar Health* **1998**, *1*, 730.
- [40] D. H. Szarowski, M. D. Andersen, S. Retterer, A. J. Spence, M. Isaacson, H. G. Craighead, J. N. Turner, W. Shain, *Brain Res.* **2003**, *983*, 23.
- [41] J. K. Nguyen, D. J. Park, J. L. Skousen, A. E. Hess-Dunning, D. J. Tyler, S. J. Rowan, C. Weder, J. R. Capadona, *J. Neural Eng.* **2014**, *11*, 056014.
- [42] R. Biran, D. C. Martin, P. A. Tresco, *Exp. Neurol.* **2005**, *195*, 115.
- [43] W. H. Chen, S. J. Cheng, J. T. Tzen, C. M. Cheng, Y. W. Lin, *PLoS One* **2013**, *8*, e83394.
- [44] D. Paganin, S. C. Mayo, T. E. Gureyev, P. R. Miller, S. W. Wilkins, *J. Microsc.* **2002**, *206*, 33.
- [45] F. Brun, S. Pacilè, A. Accardo, G. Kourousias, D. Dreossi, L. Mancini, G. Tromba, R. Pugliese, *Fund. Inform.* **2015**, *141*, 233.
- [46] F. Brun, L. Mancini, P. Kasae, S. Favretto, D. Dreossi, G. Tromba, *Nucl. Instrum. Methods Phys. Res., Sect. A* **2010**, *615*, 326.
- [47] A. Odgaard, H. J. Gundersen, *Bone* **1993**, *14*, 173.
- [48] W. B. Lindquist, S.-M. Lee, D. A. Coker, K. W. Jones, P. Spanne, *J. Geophys. Res.* **1996**, *101*, 8297.
- [49] L. Ballerini, M. Galante, M. Grandolfo, A. Nistri, *J. Physiol.* **1999**, *517*, 459.
- [50] G. Paxinos, C. Watson, *The Rat Brain in Stereotaxic Coordinates*, Elsevier Academic Press, Cambridge, MA **2005**.

## **3D meshes of carbon nanotubes mediate functional recovery in spinal cord injured rats**

**Sadaf Usmani<sup>1</sup>, Emily R. Aurand<sup>1,2</sup>, Manuela Medelin<sup>1,2</sup>, Denis Scaini<sup>1,3</sup>, Maurizio de Crescenzi<sup>4</sup>, Maurizio Prato<sup>5</sup> and Laura Ballerini<sup>1</sup>**

<sup>1</sup>International School for Advanced Studies (SISSA/ISAS), Trieste, 34136 Italy.

<sup>2</sup>Department of Life Sciences, University of Trieste, Trieste, 34127 Italy.

<sup>3</sup>NanoInnovation Laboratory, ELETTRA Synchrotron Light Source, Trieste, 34149 Italy.

<sup>4</sup>Department of Physics, University of Rome Tor Vergata, Rome, 00173 Italy.

<sup>5</sup>Department of Chemical and Pharmaceutical Sciences, University of Trieste, Trieste, Italy.

### **Abstract**

Neural implants in past decades have offered themselves as a promising tool in finding answers for spinal cord injury and yet no practical treatment is available. Glial barrier and functional deficits are major challenges needed to overcome. Here, we have used a unique scaffold fabricated from 3D multiwalled carbon nanotube fibers (CNF) as a neural implant. We investigated long term in vivo effects of this material implanted in L1 hemisection lesion. Functional locomotor recovery measured by BBB rating scale and ladder rung test demonstrated improvement starting from 24 h post-injury over a course of 8 weeks. Footprint analysis revealed early onset of plantar placement in CNF-implanted animals. Tissue reaction to the implant quantified as GFAP and Iba 1-positive area was limited and invasion of neural processes within the implanted scaffold suggests use of carbon nanofibers as a safe and neuron-friendly scaffold.

### **Introduction**

Spinal cord injury (SCI) disrupts the communication between supraspinal centers and spinal segments responsible for limb movement. This disconnection of descending pathways alters motor function, caudal to the site of lesion. Functional deficits result from damage of axons, loss of neurons and glia, and demyelination, followed by secondary consequences occurring from hours to weeks after injury (Zhang et al 2012). After SCI, there is essentially no re-

growth of axons beyond the point of the lesion, leaving intact, although nonfunctional, circuits below the site of injury. Impedance of recovery post SCI is partly due to inhibitory cues and post-lesion glial reaction. However, recent studies indicate that recovery after SCI could be possible if there is reduction in inhibitory environment, by the use of neural substrates to establish spinal circuits and providing support to these circuits to form permanent motor functional connections (Dru and Hoh, 2015 world neurosurgery). More recently, several studies highlighted the potential for functional recovery of SCI by using nanomaterials to restore spinal dysfunctional circuits through a combination of artificial connections and devices to help stimulate motor and sensory recovery. This can be achieved by the use of implantable scaffolds. While most neural scaffolds show promising results in vitro, their effect fails when implanted in vivo due to the mechanical mismatch and glial scar barrier. One of the materials with attractive mechanical, electrical and morphological properties is carbon based nano-structures, such as multi-walled carbon nanotubes (MWCNT) which are particularly inspiring for neurological applications, featuring dimensions and properties reminiscent of specific compartments of the neural machinery (Usmani et al 2016). MWCNTs can possess elastic properties matching those of the central nervous system tissue and have been reported to shape neurite architecture and boost synaptic activity in vitro (Fabbro et al 2012, Cellot et al 2009, Usmani et al 2016). Our preliminary in vivo studies on free standing meshes of carbon nanotubes, implanted in the adult rat cortex, demonstrated a reduced glial reaction in brain (Usmani et al 2016). The tissue physiology and mechanical standard of an implant, however pose different challenges to be used as a spinal implant.

For this study we have investigated potential long term use MWCNTs scaffold as a neural implant. We used a freestanding, three dimensional, mesh-like structure of pure MWCNTs that mimic the shape and mechanical characteristics of the central nervous system (CNS) previously developed (Camili et al 2013, 2014; Usmani et al 2016). We implanted these scaffolds into unilateral lesions performed under controlled surgeries in the lumbar (L1) cords of adult rats. Functional locomotor recovery was investigated by BBB scoring (Basso et al, 1995) and more discrete motor deficits that were not revealed during normal gait were assessed by ladder rung test (Metz et al., 2009) and foot print analysis (Scali et al., 2013). Tissue response to the scaffold and biointegration was quantified by immuno-histochemical analysis using markers for cytoskeletal components specific for astroglia, microglia and mature neurons. We hypothesize that the use of this material could facilitate axonal

regeneration, guide functional repair mechanisms and pose a more physiologically relevant environment for spinal repair post injury.

## **Materials and Methods**

### **Preparation of 3D CNF implants**

Three-dimensional carbon nanotubes (3D CNF) were obtained from Prof. Maurizio De Crescenzi's laboratory. As previously reported, 3D CNF is a free standing three-dimensional framework of self-assembled multi-walled carbon nanotubes. These interconnected fibers or meshes are characterized as good conductors of electricity and stiffness of the order of the human central nervous system tissue (0.1kPa-20kPa) (Tyler 2012). Sharp pointed cylinders (2-3mm length and 1.5mm diameter) were cut-out with a razor from the larger 3D scaffold to give it a shape of an implant. Material stiffness was increased to provide acute structural support to the 3DCNF in order to facilitate insertion of material into the spinal tissue. This was achieved by embedding the material into commonly used water-soluble polymer: PEG-4000 (Poly (ethylene glycol); 81240 from Sigma Aldrich, average MW 4,000 Da) at 65°C and then leaving it to solidify by cooling at room temperature. PEG-alone implants were prepared in the similar fashion without the inclusion of 3DCNF material. Scaffolds to be utilized for lumbar hemisection lesion model were further attached to a glass capillary to allow ease of implantation.

### **Surgical procedures**

All procedures, housing and post-operative care was approved by the Italian Ministry of health; authorization #938/2015-PR and behavior of rats was monitored regularly under the supervision of the institution's authorized veterinarian and the institutional ethical committee.

### ***Lumbar (L1) hemisection lesion***

A total of 12 adult female Wistar rats (2-3 months' age) were recruited for lumbar spinal hemisection model. Six animals were allocated to the control (only lesion) group, and six animals were assigned to the test (3D CNF-implanted) group. An additional set of 5 animals were used to understand correlation between lesion area and BBB locomotor performance and were sacrificed 24 hours after surgery.

A unilateral L1-L2 spinal hemisection model was utilized to produce a partial spinal cord lesion. The unilateral approach to the lesion was intended to spare bladder and bowel function. Briefly, animals were anaesthetized using Ketamine (80 mg/kg) and Xylazine (10

mg/kg) i.p. and spinal cord was exposed by drilling a hole in the lamina of T13 vertebra. A 2-3 mm diameter wide hole/window was drilled into the right lamina to approach the spinal cord and a small incision of the dura was made followed by durotomy. A lateral hemisection (hemikorpectomy) on the right side of the spinal cord was achieved with microscissors making two mediolateral incisions along the midline towards the rostral and caudal end of the hole/window. The intervening tissue of the spinal cord was taken out using sharp forceps. This created a lesion of around 2 mm in length.

3D CNF or PEG-alone scaffolds were customized to fit the lesion site and implanted while taking care of structural integrity of the implant and at the same time not exerting too much pressure to the surrounding host tissue. Homeostasis was achieved by using absorbable haemostatic gelatin sponge (Spongostan-Dental; Ferrosan). The skin was closed using staples surgical (Tweek Vistat 35R).

Throughout the whole procedure, respiration, body temperature, heart rate and oxygen saturation were regularly monitored to assess the depth of anesthesia and animal well-being. Animals were checked at regular intervals for the first 72-hours post-surgery. Both control and test groups were administered prophylactic antibiotic (Baytril–Enrofloxacin; 5 mg/kg, intraperitoneal) and analgesic solution (Rymadyl; 5 mg/kg, intraperitoneal) immediately after the surgery and for 3 consecutive days post-surgery (dps). All animals used in the study showed no sign of pain or distress, following 72-hours period, animals were monitored once per day until sacrifice.

### **Behavioral studies**

Rats were randomly numbered to ensure researchers were blind to the groups. Food and water *ad libitum* was supplied to all animals at all times to avoid fatigue due to physical exercise during behavioral testing. All animals were housed in the SISSA-animal facility in strict accordance with the approved guidelines. Pretesting, each animal was handled for 20-30 min to accustom rats to being picked up and moved. When the rats showed no signs of fear (crouching, vocalizations, no exploration, frequent defecation and urination, and no grooming), behavioral training was initiated. Animals were trained to perform selected behavioral tests for sensory-motor evaluation. BBB locomotor rating (Basso et al., 1995), ladder rung test and footprint analysis were assessed for animals with L1 hemisection lesion. Behavioral data (BBB, ladder and footprint) for this set of animals was recorded at 1, 2, 3, 5, 7, 10 and 15 days' post-surgery, then at weekly time points thereafter. All behavioral experiments were performed in the same order and at the same hour of the day. Baseline score for both sets was taken 24 hours before the surgery.

### ***BBB locomotor rating***

Open field observation of hind limb locomotor recovery was assessed by using the BBB rating scale. BBB scale is a standardized rating scale to evaluate gross motor behavior and hind limb locomotion in rats after SCI. BBB score of zero represents no hind limb movement while the highest score of 21 represents stable walking. This scale takes into consideration behavior from individual joint movements of the hindlimb, to plantar stepping, to coordinated walking and finally the subtler behaviors of locomotion, such as paw position, trunk stability and tail position. Each animal was tested individually in an open field (80 cm x 80 cm) for 3 min. For the first three min duration, rats were not disturbed by any external stimuli and video recordings of the rat behavior were made by cameras mounted on top of the open field and at a fixed angle sufficient to capture hind limb movements like coordination, toe clearance etc. During the course of testing, a numerical score from the scale was awarded by an observer blinded to the animal treatment. Any unusual behaviors like signs of pain or fear were recorded. In some cases, observation periods were extended beyond 3 min for more accurate assessment of coordination, toe clearance, paw position etc. After 3 min duration was over, rats that remained stationary for more than 10 seconds were encouraged to locomote: by enticing them with a pen or by gentle tapping on the walls of the open field. For rats that still remained inactive, they were gently picked and moved to the center of the open field. In case of borderline locomotor performance, a lower score was chosen. No training was essential for BBB locomotor rating. Animals were habituated to their surroundings and the open field at pretesting stage to reduce anxiety levels during rating.

### ***Ladder rung test***

To assess skilled motor behavior ‘Ladder rung test’ was used (Metz GA et al., 2002, 2009). This test known as ‘Foot fault test’ is aimed at revealing deficits which are not apparent during normal locomotion. By assessing stepping, limb placing and motor control, behavior on each rung, a score on a scale of 0-5 was calculated. Scoring was characterized as drag, miss, deep slip, slight slip, partial placement, and a correct placement respectively, where zero represents a drag and a five represents a correct paw placement (Metz GA et al., 2002, 2009). Sum of scores recorded in the same session were further normalized with number of events and the baseline score (recorded prior to the SCI) to ensure accuracy and inter-animal comparison. Hence the formula to calculate for each session was as follows:

$$(\text{sum of scores of all events for that day}) / (\text{all events}) * (\text{baseline score})$$

Rats were made to pass a one-meter-long horizontal ladder with equally spaced rungs; placed 2-3 cm apart to match regular sequences of step length. Two passes across the ladder were videotaped and then offline analyzed. All rats were trained for 7 consecutive days prior to the surgery. Training was achieved in a target-based manner for each rat until they excelled stepping on all the rungs. Target of the training was to train rats to pass the ladder two times with all correct placements, when the rats were able to do so for three consecutive sessions, training was stopped.

### ***Footprint analysis***

Walking stability, onset of plantar placement and inter-limb coordination can be assessed by footprint analysis (Scali et al., 2013). For collection of footprints, forepaws and hind paws were painted with different colors and rats were encouraged to walk in a straight line along a meter-long reward-directed runway over absorbent paper. A series of at least five consecutive steps were used to determine the mean values of each measurement. Since the aim of this task is to assess spontaneous walking pattern, no training was required. Baseline recording was taken 24 hours before surgery. To obtain spontaneous walking pattern of rats, and to avoid confounding effects in performance due to practice, no training was required.

### **Immunohistochemistry, image acquisition, and analysis**

Rats were sacrificed at 8-weeks post implantation. Animals were anesthetized by using Ketamine (80mg/kg) and Xylazine (10mg/kg) i.p. followed by transcardial perfusion with 0.1 M PBS and 4% PFA in PBS, respectively. Spinal cord injured segments were gently retrieved, post fixed for 24 H at 4°C, and cryprotected in 30% sucrose in PBS at 4°C until they sunk in the solution. Cryprotected spinal cords were then quick-frozen in optimal cutting temperature compound (Tissue-Tek), frozen at -20°C, and cryosectioned into 30 µm thick longitudinal sections (Figure 4A) by using a cryostat (Microm HM 550, Thermo Fisher Scientific).

Tissue-Tek was washed by PBS and tissue sections were incubated for 5 min in glycine 0.1 M, blocked in 3% BSA, 3% FBS, 0.3% Triton X-100 in PBS for 45 min at room temperature and then incubated overnight at 4°C with primary antibodies (mouse anti-GFAP, 1:400, Sigma; rabbit anti-Iba1, 1:500, Wako; rabbit anti-β-tubulin III, 1:500) in 5% FBS in PBS. Following washing in PBS, sections were incubated for 2 h at room temperature in secondary antibodies (goat anti-rabbit Alexa 594, 1:400, Invitrogen; goat anti-mouse Alexa 488, 1:400, Invitrogen; DAPI, 1:200, Invitrogen) in 5% FBS in PBS. Tissue sections were then mounted on glass coverslips using Vectashield hard mounting medium (Vector Laboratories).

Lesion area was measured 8 weeks' post-implantation by using FIJI software. Immunolabeled sections that had a clear visualization of the central canal were shortlisted (minimum 5 sections per animal) and the injured area considered as the area where disruption of tissue organization was evident, was calculated.

We examined spinal cord sections by the presence of markers for reactive astrocytes, with glial fibrillary acidic protein (GFAP), for microglia with ionized calcium-binding adaptor protein-1 (Iba1), and for neurons ( $\beta$ -tubulin III; NeuN). Quantification of tissue reaction was achieved by measuring GFAP and Iba1 labelling surrounding the entirety of the lesioned area. Fluorescence images were acquired using a Leica DM6000 upright microscope with a 10x dry objective. Identical binning, gains and exposure times were used for all images of the same marker. Image analysis was performed using the FIJI software. For both GFAP and Iba1 analysis, in each section  $n = 6$  ROIs ( $100 \times 500 \mu\text{m}^2$ ) were selected at different distances from the lesion edge (both rostrally and caudally):  $0 \mu\text{m}$ ,  $100 \mu\text{m}$  and  $500 \mu\text{m}$ . The background intensity threshold was defined for each spinal cord section using the labeling intensity measured in the contralateral spinal cord (left side) at  $500 \mu\text{m}$  rostral and caudal from the lesion edge (Figure 4A). The area within each ROI with intensity above the background threshold was calculated, normalized to the contralateral hemicord and used for statistics. Therefore, for each subject, data are presented as the fold increase of both GFAP and Iba1 over baseline levels estimated in the contralateral uninjured cord.

Values were expressed as mean  $\pm$  SEM. Unpaired-t-test was used to find statistical significance between two groups and two-way ANOVA was used to determine significance between multiple groups. Statistical significance was defined as  $P < 0.05$  in all statistical evaluations.

## **Results and Discussion**

Attracted by the properties of the carbon based materials and promising *in-vitro* and preliminary *in-vivo* results obtained from 3D meshes of MWCNTs, named 3D CNF (Usmani *et al.*, 2016), we were interested in investigating intensive *in-vivo* response of this material. We fabricated a scaffold implant comprised of a three-dimensional free-standing sponge of pure carbon nanofibres soaked in a widely used water-soluble, biocompatible, polymer (polyethylene glycol-PEG). PEG provided structural integrity to the very elastic, ultra-light weight and porous 3D CNF, so as to facilitate ease of implantation (Usmani *et al.*, 2016; Camilli *et al.*, 2013) (Figure 1A). Using PEG as glue, the scaffold was attached to glass capillary to allow grasp and improved precision in implanting procedure (Figure 1A). For this



study, we used lumbar L1-hemisection lesion in rat spinal cords to induce spinal cord injury. Rats previously trained with behavioral tasks to assess locomotor function were induced with spinal cord injury; a lesion in the right hemicord of the L1 spinal segment (lesion-group) (Figure 1B). The CNF scaffold attached to the glass capillary (using PEG as glue) was pushed/implanted into the lesioned spinal cord; within few seconds PEG solubilizes at the animal body temperature detaching the implanted scaffold from the glass capillary (CNF-group). Once implantation was achieved glass capillary was pulled out and discarded away. Both groups of animals were kept under observation and left undisturbed to recover for 24 hours. Behavior changes in locomotor recovery were recorded at defined intervals for 8 weeks.

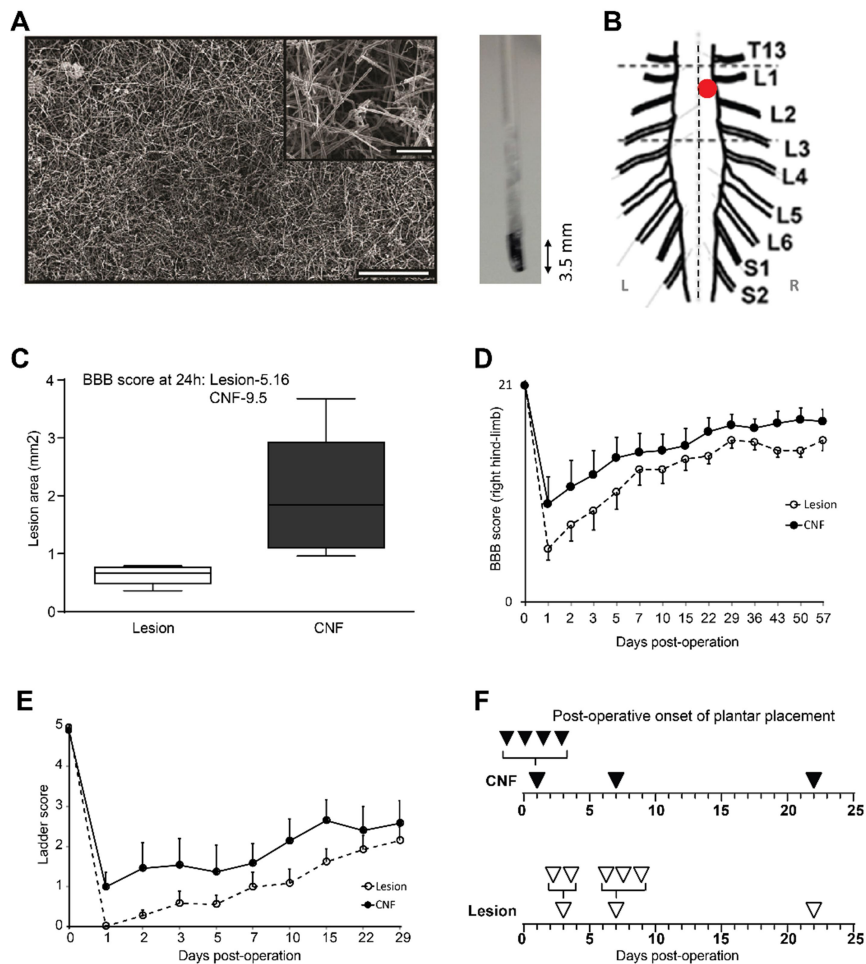


**Figure 1. Functional recovery in locomotor behavior of injured rats implanted with CNF.** (A) Right: SEM image of CNF material demonstrating the morphology of the implant. A random network of interconnected carbon nanotubes can be apparent at higher magnification (inset). Scale bar: 250  $\mu$ m and 25  $\mu$ m (inset) (adapted from Usmani et al 2016,

Sci Adv) Left: Picture of the CNF-implant before implantation. A glass capillary is glued to the material using PEG to provide structural stability and ease of implantation. (B) Diagram of dorsal view of a rat spinal cord the lesion and implant site is marked (red dot); L: left, R: right. (C) Animals implanted with CNF exhibited significantly larger lesion area when measured 8 weeks post-surgery. Average BBB score (at 24 hour post-surgery) for lesion group (no implant) and 3D CNF-implanted group was 5.16 and 9.5 respectively. Locomotor activity despite larger lesion area was improved in CNF-implanted animals. (D) Plot of the time course of locomotor functional recovery of SCI-inflicted hind limb (right) as measured by BBB rating scores for control lesion and CNF-implanted group. Both animal groups persistently improved in locomotor function for 30 days post SCI. CNF-implanted animals showed greater recovery compared to the lesion-group starting from 24-hour post SCI. Improved motor function in CNF implanted animals compared with lesion-group was apparent over 60 days post-surgery. (E) Ladder rung test: plot summarizes the combined ladder performance scores against days post-surgery. The number of foot faults post SCI was increased in all groups. Starting from day 1 post-surgery, CNF-implanted animals showed a better performance than the lesion-group over the course of 15 days post SCI. (F) Post-operation onset of plantar placement assessed by footprint analysis. Greater number of CNF-implanted animals displayed plantar placement 24 hours post-surgery. Arrow heads represent each animal. ( $n_{\text{lesion}}=6$ ;  $n_{\text{CNF}}=6$ ).

Figure 1C shows the average values of the lesion extent. We measured the lesion area by immunofluorescence approach (Figure 4B) 8 weeks after the surgery and we found that lesions were significantly larger in CNF implanted group of animals compared to the lesion-group (Figure 1C;  $0.63 \pm 0.07 \text{ mm}^2$  and  $2.02 \pm 0.17 \text{ mm}^2$  for lesion and CNF-implanted animals, respectively;  $P < 0.01$ ). In C it is also reported the average BBB score at 24 hours in the two groups, notably CNF usually displayed higher scores. When carefully observed under microscopy (40x-data not shown), we did not detect tissue dearrangements or damages in the area surrounding the implant, in fact  $\beta$ -tubulin III or NeuN positive cells were clearly detectable (Figure 3A). Despite the larger area of lesion, motor recovery, measured by BBB scale, was higher at 24-hour post-surgery and 8-weeks post-surgery for 3D CNF-implanted group when compared to the lesion-group. We cannot exclude that the CNF lesion be larger from the beginning (regardless of the BBB score; Figure 4b demonstrates correlation between BBB score and the lesion area 24 hours post-surgery), however it could be possible that the lesion area in control group was reduced as a result of collapsing of tissue over the course of time. This does not happen in the CNF-group probably due to the presence of the implant, mechanically sustaining the damaged spinal cord. The observed improvement in locomotor activity suggests the capacity of this scaffold in promoting functional recovery post SCI, or reducing immediate reactivity to SCI.

### **CNF accelerated functional locomotor recovery**

SCI resulted in loss of locomotor function of the ipsilateral hind limb to the lesioned hemicord. 24 hours post SCI, CNF-implanted animals recovered considerable motor function with a score of  $9.5 \pm 2.7$ , allowing occasional weight supported plantar stepping with no fore limb-hind limb (FL-HL) coordination, as opposed to lesioned animals with a score of  $5.2 \pm 1.2$ , allowing slight movement of two joints and extensive movement of the third with no weight support or plantar placement ( $N_{\text{lesion}}, N_{\text{CNF}} = 6$ , summarized in plot in Figure 1D). One-week post SCI, consistent weight supported plantar stepping and FL-HL coordination was regained in CNF-implanted group. After day 29, both animal groups started to plateau in terms of recovery at a score of  $17.2 \pm 1.2$  and  $15.6 \pm 0.7$  for CNF and lesion-group, respectively. The scores persisted till the day of sacrifice i.e. day 57 with the score value for lesion and CNF group;  $17.5 \pm 1.2$  and  $15.6 \pm 6$ . Post incomplete SCI, most individuals show substantial degrees of spontaneous recovery, majorly as a result of plasticity and compensatory sprouting of surviving neurons. However, the marked improvement of functional recovery starting at 24 h post-SCI indicate involvement of facilitation of tissue response at the early acute phase in CNF-implanted animals. Unique mechanical coupling of the implant and the neural tissue of the CNF might be responsible for management of acute SCI outcomes, like for example edema. Intensive research of spinal cord physiology has also revealed the ability of the embedded circuits in the lumbar segments of mammals in producing coordinated patterns of leg motor activity without supraspinal input (Sherrington et al., 1910, Kiehn O et al., 2017, Capogrosso et al, 2016).

By encouraging rats to walk on ladder, animal behaviors like stepping, limb placing and motor control were recorded and scored. After SCI, both groups with L1-lesion showed a dramatic drop in the score from the maximum value of 5 in both animal groups. 24 hours post SCI, lesioned animals barely moved the inflicted limb with a score of  $0.01 \pm 0.01$  while CNF-implanted animals could make attempts to place paws on the rung, with a score of  $1 \pm 0.37$ . Both groups showed improved performance over the course of 15 days' post-surgery. At 15<sup>th</sup> day, lesioned animals scored  $1.61 \pm 0.34$  allowing the reaching of the rungs (Figure 1E). This was however followed by deep slips due to lack of weight support. CNF-implanted animals, on the other hand, developed greater balance and weight support with a score of  $2.64 \pm 0.54$ . After day 15, ladder scores of both animal groups plateaued and over the course of 8 weeks, lesion-group of animals continued to show slightly larger deficits in motor performance (from 32% recovery at day 15 to 43% at day 29 in lesion group after which no improvement was

observed when compared to CNF which was 52% recovery at day 15 and persisted to be 52 % at day 29).

Onset of plantar placement post SCI showed a marked difference between lesion and CNF-implanted groups. Lesioned animals took minimum 3 days to develop plantar placement, as opposed to CNF implanted animals where four out of six animals displayed plantar placement 24 hours post SCI. Our data suggests that CNF-implanted animals showed quicker and improved locomotor recovery post SCI in comparison to the lesion-group.

The strength of the ladder rung test is that it provides more descriptive accounts on impairment. To perform tasks on the ladder, animals need regular limb coordination and control weight support to correctly place limbs. An in-depth study of locomotion by ladder test was achieved and the results of locomotor rating by BBB were confirmed in a more descriptive manner. Improvement in tasks like placing and stepping, suggest boosting of innervation of the hind limb muscles, perhaps due to plasticity or compensation. To exclude effect of PEG used as a vehicle in improved recovery, a set of animals implanted with only PEG were tested in both lumbar L1 and cervical C6 spinal segments. PEG implanted animals failed to show the progression in recovery as observed in the case of CNF-implanted animals.

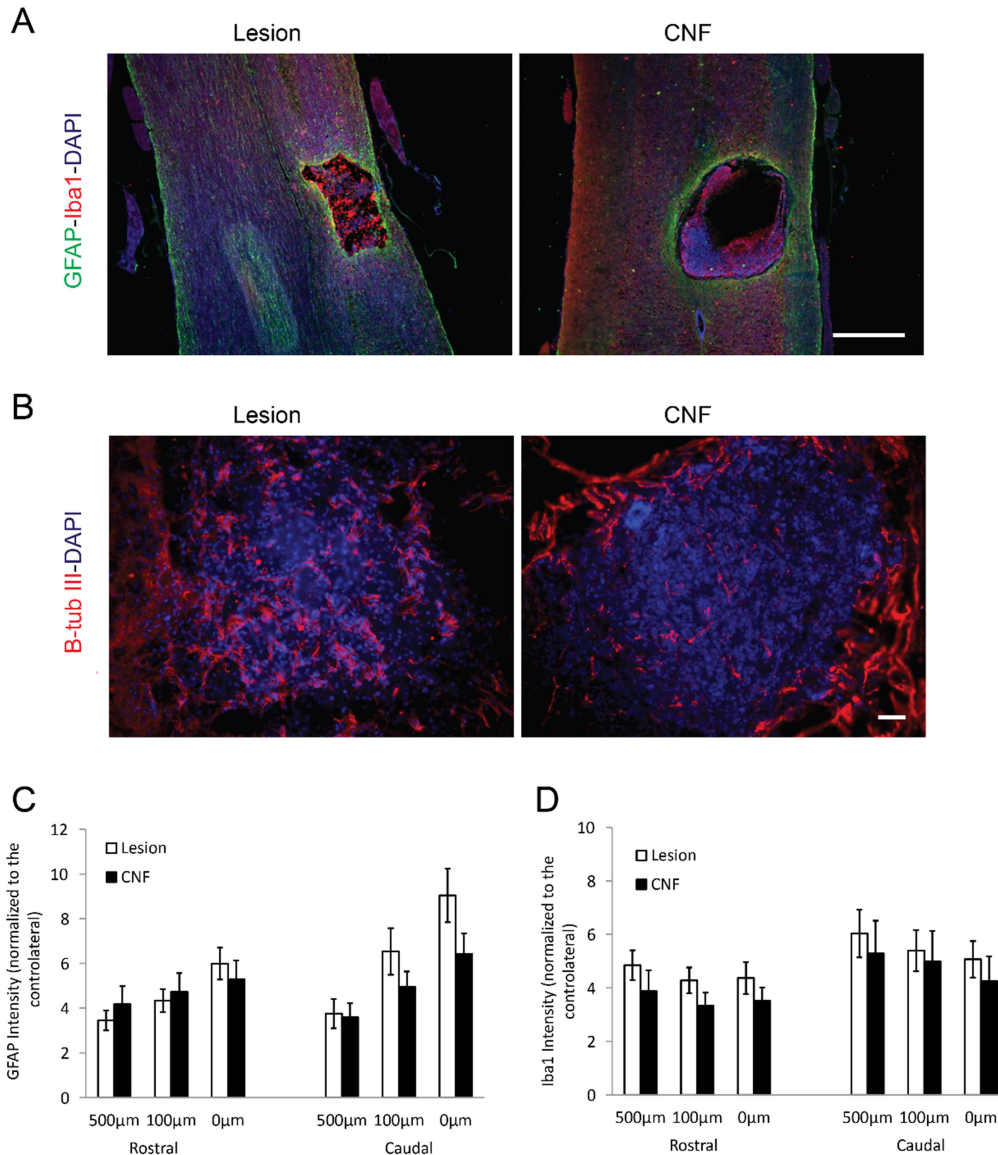


**Figure 3. Tissue response to CNF-scaffold implanted in rat spinal cord (lumbar level L1 hemileSION).** (A) GFAP-positive astrocytes and Iba1-positive microglia were found in the spinal cord surrounding the lesion alone or when filled by the implanted material (CNF). Microglia was also infiltrating the scaffold and the lesion at 8 weeks post-implantation. Scale bar: 1 mm. (B) High magnification of the lesion alone or when filled by CNF. Note that  $\beta$ -tubulin III-positive neurons are invading the lesioned area as well as the scaffold. Scale bar: 100  $\mu$ m. Histograms in (C) and (D) quantify GFAP (left) and Iba1 (right) positive tissue immunoreactivity. Note the increasing GFAP intensity from rostral to caudal end of the lesion. This increment of tissue reaction was spared in animals implanted with CNF. Data are presented as mean $\pm$ SEM.

**Tissue reaction to 3D CNF implanted into L1 hemisection lesion in adult Wistar rats.**

In our previous study (Usmani *et al.*, 2016; Science Advances), we assessed the biocompatibility of 3D CNF when implanted into the brain of adult male Wistar rats. In this study, we tested tissue reactivity after implanting the scaffold at a lesioned site in the spinal cord, and compare this reactivity to that induced by the surgery *per se*.

Tissue reaction to the implanted CNF was measured by quantifying GFAP (reactive astrocytes) and Iba1 (microglia) on spinal sections obtained 8 weeks post implantation. A comparison between SCI-lesion group and CNF-implanted group is shown in Figure 3. 3D CNF demonstrated to be biocompatible when implanted into adult rat spinal cord: the inflammatory response was similar or even lower compared to that induced by the lesion alone. One thing that deserves to be noticed is that Iba1-reactivity was similar in all tested conditions: there is no correlation with the distance neither from the implant nor in the rostral vs. caudal position (Figure 3C). While considering GFAP analysis, it is evident that its reactivity is location-dependent: higher GFAP intensity was present closer to the lesion site, in particular caudal to the lesion (Figure 3D). We noticed an increased GFAP reactivity in the ROIs caudal to the lesion compared with the rostral ROIs. This is not too surprising since a major part of recovery is mediated by the supraspinal centers located above the lesion site. As per previous reports, spontaneous functional recovery might involve sprouting and detouring of existing innervations from spared neurons, mostly located in regions rostral to the injury site (i.e. undisrupted supra-lesion site; Isa T 2017). Interestingly, this increased trend of GFAP reactivity was not as evident in CNF implanted animals. We hypothesize that this effect can be due to an improved propriospinal detouring or crossing (around or through) the 3D CNF implant (Filli et al 2014, Pohland et al 2015). We did not investigate any markers or presence of such innervation in our study yet, but it would be helpful to speculate the origin of these observed differences. These results strongly support 3D CNF as biocompatible and well-integrated within the spinal cord tissue. Moreover, we detected neurons invading the 3D scaffolds indicating that the environment was permissive for neuronal re-growth (Figure 3B). These neuronal processes, could be a result of migrating neuroblasts or newly regenerating cells mediated by injury mechanism. This has been previously reported in Usmani et al 2016 and Aurand et al 2017, where we have implanted this material in cortical areas of the brain. (Usmani et al., 2016, Aurand et al., 2017). We observed that these  $\beta$ -tub-III- positive fibres were present in all labeled sections of the lesion group and a majority of the 3D CNF implanted sections (100% n=26 and 87% n=31 for lesion and 3D CNF implanted groups respectively). As shown in Figure 3B, we observed these processes as fragments or clusters of  $\beta$ -tub-III- positive processes without a structure, maybe due to lack of mechanical support.

We speculated these processes in the 3D CNF implanted regions as well. The neuronal processes growing into the implanted substrate were apparently more structured and arborized. We believe that the 3D CNF was able to direct the growth of the infiltrated neuronal processes in vivo due to its peculiar morphological properties (Usmani et al., 2016). This observation goes hand in hand with our previous in-vitro reports published in Usmani et al., 2016 where the 3DCNF potentially redirected the outgrowing spinal fasciculations into a complex web of mesh-like morphology resulting in an improved functional reconnection of segregated explants. Indeed, a deeper look into this is necessary to investigate the shape and length of these processes for more understanding. This can open doors to gain better insights of the neuronal physiological changes potentiated by the 3D CNF scaffolds and their role in nervous system repair mechanisms.

## **Conclusion**

We have implanted three-dimensional fibre meshes of multiwalled carbon nanotubes into the injured rat spinal cord and explored long term biointegration, functionality and tissue response. Functional behaviour assessment of locomotor activity demonstrated a faster and improved recovery in lumbar hemilesion model. Implant triggered limited foreign-body reaction and integrated well with the surrounding tissue. Neuronal processes migrated within the implant indicating neuro-compatibility. We encourage use of this implant for further studies as a possible neural interface.

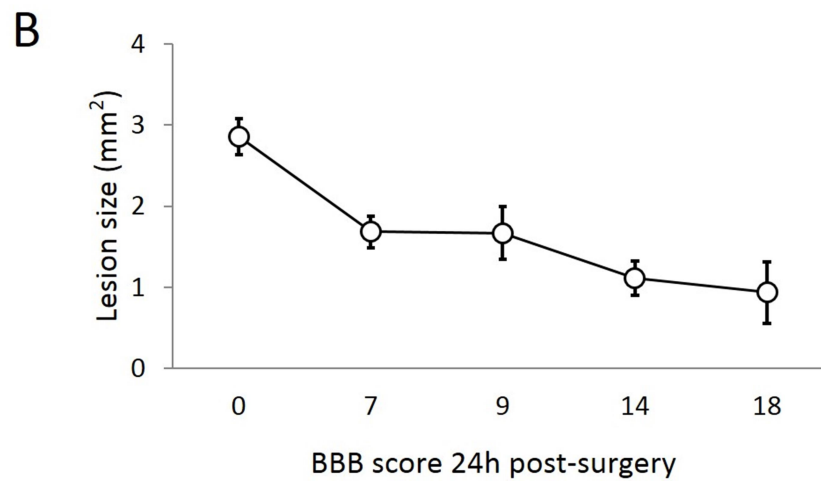
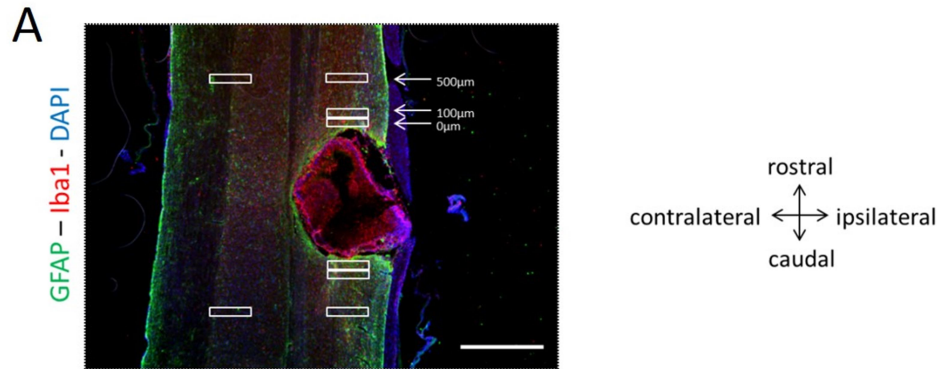


**Figure 4:** (A) Example of a fluorescence image for GFAP-positive astrocytes (green) and Iba1-positive microglia (red) to explain how the analysis has been performed; DAPI (blue). Scale bar: 1 mm (B) Correlation of lesion area with BBB score (one animal each time point).

## References

Basso D.M., Beattie M.S., Bresnahan J.C. A sensitive and reliable locomotor rating scale for open field testing in rats. *J Neurotrauma.* ;12:1–21 (1995)

Camilli L., Pisani C., Gautron E., Scarselli M., Castrucci P., D’Orazio F., Passacantando M., Moscone D., De Crescenzi M., A three-dimensional carbon nanotube network for water treatment. *Nanotechnology*25, 065071 (2014)

Camilli L., Pisani C., Passacantando M., Grossi V., Scarselli M., Castrucci P., De Crescenzi M., Pressure-dependent electrical conductivity of freestanding three-dimensional carbon nanotube network. *Appl. Phys. Lett.* 102, 183117 (2013)



Capogrosso, M., Milekovic, T., Borton, D., Wagner, F., Moraud, E. M., Mignardot, J.-B., ... Courtine, G. A Brain–Spinal Interface Alleviating Gait Deficits after Spinal Cord Injury in Primates. *Nature*, 539(7628), 284–288 (2016)

Cellot G., Toma F. M., Varley Z. K., Laishram J., Villari A., Quintana M., Cipollone S., Prato M., Ballerini L., Carbon nanotube scaffolds tune synaptic strength in cultured neural circuits: Novel frontiers in nanomaterial–tissue interactions. *J. Neurosci.* 31, 12945–12953 (2011)

De Volder M. F. L., Tawfick S. H., Baughman R. H., Hart A. J., Carbon nanotubes: Present and future commercial applications. *Science* 339, 535–539 (2013)

Dru AB, Hoh DJ. Activating spinal interneurons for neural repair after spinal cord injury. *World Neurosurg.* (2015)

Fabbro A., Prato M., Ballerini L., Carbon nanotubes in neuroregeneration and repair. *Adv. Drug Deliv. Rev.* 65, 2034–2044 (2013)

Fabbro A., Villari A., Laishram J., Scaini D., Toma F. M., Turco A., Prato M., Ballerini L., Spinal cord explants use carbon nanotube interfaces to enhance neurite outgrowth and to fortify synaptic inputs. *ACS Nano* 6, 2041–2055 (2012)

Hu H., Ni Y., Montana V., Haddon R. C., Parpura V., Chemically functionalized carbon nanotubes as substrates for neuronal growth. *Nano Lett.* 4, 507–511 (2004)

Kiehn O. Decoding the organization of spinal circuits that control locomotion. *Nat Rev Neurosci*, 17:224–238 (2016)

Kotov N. A., Winter J. O., Clements I. P., Jan E., Timko B. P., Campidelli S., Pathak S., Mazzatenta A., Lieber C. M., Prato M., Bellamkonda R. V., Silva G. A., Kam N. W. S., Patolsky F., Ballerini L., Nanomaterials for neural interfaces. *Adv. Mater.* 21, 3970–4004 (2009)

López-Dolado, E., González-Mayorga, A., Portolés, M. T., Feito, M. J., Ferrer, M. L., del Monte, F., Gutiérrez, M. C. and Serrano, M. C., Subacute Tissue Response to 3D Graphene Oxide Scaffolds Implanted in the Injured Rat Spinal Cord. *Adv. Healthcare Mater.*, 4: 1861–1868 (2015)

Lovat V., Pantarotto D., Lagostena L., Cacciari B., Grandolfo M., Righi M., Spalluto G., Prato M., Ballerini L., Carbon nanotube substrates boost neuronal electrical signaling. *Nano Lett.* 5, 1107–1110 (2005)

Mazzatenta A., Giugliano M., Campidelli S., Gambazzi L., Businaro L., Markram H., Prato M., Ballerini L., Interfacing neurons with carbon nanotubes: Electrical signal transfer and synaptic stimulation in cultured brain circuits. *J. Neurosci.* 27, 6931–6936 (2007)

Metz GA, Whishaw IQ. Drug-induced rotation intensity in unilateral dopamine-depleted rats is not correlated with end point or qualitative measures of forelimb or hindlimb motor performance. *Neuroscience* ; 111:325–336 (2002).

Metz, Gerlinde A., and Ian Q. Whishaw. “The Ladder Rung Walking Task: A Scoring System and Its Practical Application.” *Journal of Visualized Experiments : JoVE* 28: 1204. (2009)

Scali M, Begenisic T, Mainardi M, Milanese M, Bonifacino T, Bonanno G, Sale A, Maffei L., Fluoxetine treatment promotes functional recovery in a rat model of cervical spinal cord injury. *Sci Rep.* 3, 2217 (2013).

Sherrington C. Flexion-reflex of the limb, crossed extension reflex, and reflex stepping and standing. *J Physiol (Lond)*;40, 28–121 (1910)

Tyler W. J., The mechanobiology of brain function. *Nat. Rev. Neurosci.* 13, 867–878 (2012)

Usmani, S., Aurand, E. R., Medelin, M., Fabbro, A., Scaini, D., Laishram, J., ... Ballerini, L. 3D meshes of carbon nanotubes guide functional reconnection of segregated spinal explants. *Science Advances*, 7; 2 (2016)

Zhang, N., Yin, Y., Xu, S.-J., Wu, Y.-P., & Chen, W.-S.. Inflammation & apoptosis in spinal cord injury. *The Indian Journal of Medical Research*, 135, 3, 287–296 (2012)

# Discussion

---

Previous works from our lab have shown that two dimensional CNT substrates interfaced to spinal slices resulted in nerve fibre elongation, increased number of growth cones, and presence of tight contacts between biological membranes and CNT. This adaptation of neural processes and membranes was not just morphological but also electrophysiological. Synaptic performance in both hippocampal cultures as well as spinal slices was improved when cultures were interfacing CNTs (Fabbro et al 2012, Cellot et al 2009). However, in moving to the third dimension, a more realistic material organization and arrangement which mimics the biological microenvironment, has been produced. Three-dimensional substrates have been shown to represent a better geometry, chemistry, and signalling environment of natural extracellular matrix which, when seeded with cells, can result in highly interconnected, densely populated, tissue-like formations (Lee J et al., 2008; Baranes 2007, Kokot G et al. 2015).

In our study we have investigated effects of 3D CNT scaffolds on the development of neural networks from organotypic spinal cord slices. Organotypic spinal slices have proven to be an excellent model for screening of substrates/materials, as it preserves the sensory-motor microenvironment within the slice (Gerardo Nava 2014, Pena F 2010, Gahwiler BH et al 1997). Our results demonstrate that a highly conductive, porous nanostructure 3D substrates comprised of pure MWCNT freestanding structure (3D CNF) (Usmani et al 2016) and a microporous PDMS polymer incorporated with MWCNTs (PDMS+CNT) offer favourable environmental cues for the growth of spinal neuritic networks originating from spinal cord slices *in vitro*. We also show an improved electrophysiological performance which may favour the use of our substrates as scaffolds for tissue regrowth.

By interfacing organotypic spinal slices to 3D meshes of CNT scaffold (3D CNF), 2D CNT carpet, 3D porous polymer structure deprived of CNTs (PDMS-scaffold), and PDMS scaffold enriched with CNTs (PDMS+CNT), we investigated neurite morphology and electrophysiological performance.

We found  $\beta$ -tubulin III-positive neurites exiting from the spinal slices spread over the surface of the substrates in abundance. Similar to previous reports regarding fibre outgrowth

(Fabbro et al, 2012), in controls the neuronal processes were organized into thick bundles of aligned fibres. In contrast, 3D CNF was able to shape the morphology of the outgrowing neurites into a complex web of randomly oriented processes. Morphology of neuronal fibres outgrowing on CNT substrates was paralleled by the MWCNT's mesh. This suggests that the neuronal processes use material as a supportive grid exploiting the elaborate surface area of the scaffold architecture. Neuronal fibres were significantly denser on CNT substrates and were directed to form a uniform continuous layer of mesh-like morphology. Previous reports have demonstrated absence of such continuous fibre outgrowth can lead to necrotic holes during tissue formation (Straley et al., 2010).  $\beta$ -tubulin III-positive neurites were also shown to exploit pores into the third dimension to form complex neural networks. Neuronal processes were found populated within the pores into the third dimension in 3D CNF, PDMS and PDMS+CNT scaffolds. Interestingly, we found that neurites penetrated significantly greater depths into PDMS substrates compared with the PDMS+CNT substrates. We suggest that the presence of CNT may cause neurites to stay in tight association with the substrate, thus remaining closer to the interface surface; whereas in the case of PDMS, neurites tend to drop down into the pores following gravity, without associating with the material. The fact that the neurite-CNT association is the rationale for the neuronal processes remaining at the surface of the scaffold is supported by previous work which suggests that CNTs are highly adhesive and form extremely tight contacts with biological membranes (Fabbro et al 2012, Cellot et al 2009).

Functional changes in the activity of spinal slice cells attributed to substrate conditions were addressed by means of electrophysiology. Spontaneous activity of neuronal populations, recorded as local field potentials (LFP), was disinhibited by the use of the glycine/ $\gamma$ -aminobutyric acid type A receptor antagonists, strychnine and bicuculline, respectively. This gives rise to a slow-pace rhythmic activity, also called disinhibited bursts. Disinhibited burst activity recorded from ventral regions of the slice (within 20-100 $\mu$ m of the ventral fissure) demonstrated excitatory motor output of the spinal slice (Ballerini et al 1998, Furlan F et al 2007,). Our studies demonstrate no change in frequency (calculated in terms of inter-event interval) of spontaneous disinhibited activity between controls and 3D CNF but a significant increase in frequency on PDMS+CNT compared with PDMS alone was observed. This increase in frequency suggests an improved synaptic performance. This improvement

can be due to an increased number of synapses, the potentiation of existing synapses, or both (Lovat., 2005, Fabbro., 2012). This is supported by previous studies on 2D CNT, where spinal slice neurons and hippocampal neurons demonstrated a potentiation in neuronal signaling and increased synaptic activity, respectively (Fabbro et al., 2012, Lovat et al., 2005).

To determine if the substrates are able to promote functional connectivity between spinal slice pairs, a sufficient distance ( $>300\mu\text{m}$ ) between co-cultured spinal slices was established to ensure a disconnected network condition. Spinal slice pairs at this distance in control conditions (i.e. spinal slices on glass embedded in firbin glue) are restricted from reforming functional synaptic connections (Heidemann et al 2014). In these conditions, we measured the cross-correlation activity of our spinal slice pairs which estimates the functional and electrical connectivity between neuronal networks (Ullo et al 2014, Garofalo et al 2009). Our results indicate that spinal slice pairs cultured on 3D CNF scaffolds are more likely to show functional reconnection than slices under control conditions. An increased cross-correlation of synaptic disinhibited bursts between spinal slice pairs cultured on 3D CNF was observed compared to controls. The strength or the success of reconnection formed between the networks was explored by entraining the disinhibited activity via sensory inputs. Dorsal horn stimulation of one slice out of the pair entrains the disinhibited activity of stimulated slice. However, in the presence of effective synaptic connection between the slices, a cross-entrainment of the unstimulated slice occurs. We found that, unstimulated slices cultures on 3D CNF were able to sense the stimulation and get cross-entrained unlike controls. This indicates and confirms the ability of 3D CNF scaffold in establishment of synaptic reconnection in segregated spinal networks that lack successful reconnection otherwise, despite huge outgrowth of fibres.

To understand if this was ascribed to the three-dimensionality of the scaffold or due to the presence of CNTs, a comparison with spinal slices generated in the same manner on 2D CNTs and 'three dimensional' PDMS scaffolds was added to our study.. Interestingly, we observed that 2D CNT and PDMS demonstrated a significantly higher percentage of correlated slice pairs compared to control, but not as high as the 3D CNF. When the PDMS was enriched with CNTs, the number of correlated slices increased significantly. Percentage correlation measured as number of slice pairs that functionally reconnected was similar in 3D

CNF and PDMS+CNT. Thus, indicating the role of CNTs and three-dimensionality of the scaffold in guiding effective reconnection of separated networks. We addressed if this functional coupling between the segregated explants was an outcome of direct electrical transmissions between slices, however this idea was refuted by the entrainment studies, where we found comparable values of latencies in stimulated coupled slices between 3D CNF and Controls. Our latency values were of the order of reported inter-segmental delays in the entire spinal cord (Bracci et al 1997) suggesting involvement of multisynaptic pathways in guiding a functional coupling between spinal slice segments. The inherent electrical properties of the CNTs as well as larger surface areas exposed for new synaptic contacts are crucial role players in explaining the functional coupling (Parak et al., 2001, Schmidt et al., 1997). The improved guidance of neurites towards a functional synaptic connection as a result of interaction with 3D CNT scaffolds can be attributed to physical, chemical and biological alterations leading to axonal regrowth, synapse formation and/or extracellular matrix deposition, (Stevens et al 2005). We have not addressed each of the above mentioned factors discretely in our study, but it would be interesting to speculate more intensively the interactions of 3D CNT scaffolds in restructuring fibre fasciculations.

Although, our studies reveal 3D MWCNT-derived substrates as potential candidates for neural network regrowth *in vitro*, *in vivo* studies on their biointeraction have never been tested. Given the increased activity and correlation of spinal slices on 3D CNF and PDMS+CNT compared with other substrates, we assessed the neuro-immune response of rat cortical tissue to 3D CNF and PDMS+CNT material as a pilot test of *in vivo* biocompatibility. Before proceeding towards any deeper assessments of functional outcomes; e.g. on a spinal cord lesion model, we thought it was relevant to report a preliminary response to our materials *in vivo* which is extremely important for any material to be considered acceptable for further clinical developments. Most neural implanted materials reported in literature illustrate reduced functionality over time due to the neuro-immune response and glial scarring, an indicator of inadequate biocompatibility (McConnell 2009, Winslow 2010, Gutowski 2013, Polikov 2005). The first two-four weeks following material implantation is when typically glial scar generates. It is characterized by a dense reactive astrocyte and microglial response usually extending beyond 100  $\mu\text{m}$  from the implant (Turner 1998, Szarowski 2003, McConnell 2009, Winslow 2010, Polikov 2005). The region

surrounding the implant is also characterized by neuro-degeneration and a decrease in the number of local neurons (McConnell 2009, Winslow 2010). The ultimate potential of any implantable device resides in its integration with biological milieu *in vivo*. Thus, we report the performance of 3D CNF and PDMS+CNT when challenged by a physiological environment focussing mainly at the 2, 4 and 8-weeks post-implantation in order to explore progression of inflammatory states and glial reaction (Biran et al 2003, Seymour et al 2007, Turner et al 1999).

Interestingly, we observed a lack of interaction of the brain tissue with implanted PDMS scaffolds not incorporated with CNT (data not shown). In these tissues, we observed no infiltration of endogenous cells into the material and little glial response in the surrounding tissue, with the defined edges of the implant clearly visible. This is supported by previous reports in literature that state PDMS substrates despite biocompatibility demonstrate poor integration with CNS tissue (Lu et al 2009). In addition to the potential functional benefits of CNTs over other tested substrates and PDMS-alone *in vitro*, we chose to focus our pilot study on the 3D CNF PDMS+CNT material. Provided that CNTs form intimate contact with biological membranes, we sought to impart structural cues to further improve bio-integration of PDMS-derived materials. Similar to other reports regarding the neuro-immune response to cortical implants, we observed an increase in GFAP-positive astrocyte labelling in the tissue surrounding the scaffold from 2 to 4 weeks after implantation in both 3D CNF and 3D PDMS+CNT scaffolds (Szarowski 2003, Winslow 2010, Gutowski 2013, Nguyen 2014). The glial response measured at 4 week was extremely low compared to other artificial implants. At 8 weeks, no further increase was observed, in fact at 8 weeks post-implantation, the response was condensed to the area immediately surrounding the scaffold. There were no indications that this thin astrocyte sheath was inhibitory to cellular infiltration into the implanted scaffolds, as  $\beta$ -Tub-III -positive neurons, GFAP-positive astrocytes, and DAPI-positive cellular nuclei were observed within the material. Indeed, it could be possible that the astrocytes surrounding the material could be “leading the way” for further infiltration by neural cells and creating an environment permissive to tissue re-formation. We observed GFAP-positive cells and  $\beta$ -Tub-III positive neuronal cells and fibres infiltrating the 3D CNF scaffold and in areas coinciding with CNT deposition in PDMS+CNT scaffold, suggesting that the CNT may be the key component, possibly acting as an electrical attractant and

providing the necessary nano-surface features, in the cellular colonization of the implant (Mattson 2000, Cellot 2009, Sorkin 2009, Shein 2009, Huang 2012). This colonization of neural cell bodies, could not be neurons trapped during the implant insertion as the scaffold was pre-embedded with a polymer (See Materials and Methods). It is possible that newly generated neurons could have migrated due to injury-mediated mechanisms. Recent study by Zhou et al, have reported neuroblast migration into implanted graphene scaffolds at distances away from the source (Zhou et al 2016). However, further studies to identify these cells by immunohistochemistry would be helpful in finding origin of these cells. In accordance with the reduction in inflammatory phase of the neuro-immune response, we found a significant decrease in the intensity of Iba1-positive microglia labeling surrounding the implant over time. This is in contrast to the persistent up-regulation of microglia associated with compromised biocompatibility and foreign body rejection often seen with implanted electrodes (Szarowski 2003, Biran 2005, Winslow 2010, McConnell 2009, Gutowski 2013, Nguyen 2014). Overall, the insubstantial glial response and the colonization of the material with native cells suggest that the 3D CNF and PDMS+CNT material are biocompatible with neural tissue.

Our results demonstrating in-vitro and preliminary in-vivo responses suggest 3D CNF as a potential candidate for the regrowth of neural networks. However following spinal cord injury in-vivo, the ability of neural interfaces in reducing inhibitory environment and favouring neural circuit formation are determining factors for the success of an implant. Thus, behavioural and functional investigation of in-vivo responses in an injured CNS environment is an important determining factor for any future neural substrate. In this part of our study, we have investigated the impact of 3D CNF scaffold in functional recovery and the long term tissue reactivity to scaffolds implanted following a SCI. We studied sensory-motor behavioural changes and long term in-vivo responses involved with the use of 3D CNF scaffold when implanted in a lumbar L1-hemisection lesion model. A unilateral hemisection at the lumbar (L1) segment disrupts the communication between supra-spinal centres and descending pathways resulting in compromised limb movements caudal to the hemisection. Sensory-motor deficits associated with L1-spinal injury are noted in the hind-limb ipsilateral to the site of lesion. A unilateral approach spares the function of bladder and bowel that is otherwise compromised with a complete transection. Our results show that 3D CNF used as a



neural implant promote early onset and improved functional recovery following SCI in rats as opposed to untreated lesioned animals. We also show a limited glial reaction following implantation of this material into the injured spinal cord milieu thus favouring the use of our substrate as a successful neural interface.

By performing BBB locomotor rating, hind-limb locomotor recovery, taking into account behavior from individual joint movements, to plantar stepping, coordinated walking and finally the subtler behaviors of locomotion, such as paw position, trunk stability and tail position can be measured (Basso et al 1995). Post incomplete SCI in adult rats, reportedly most individuals show substantial degrees of spontaneous recovery, majorly as a result of plasticity and compensatory sprouting of surrounding neurons, mainly resulting from mechanisms mediated by the injury in the surrounding CNS milieu despite persistence of the injury/lesion. Other reports have suggested role of supraspinal centres in improved function post-injury (Filli et al 2014, Isa T 2017). Our data demonstrate a marked improvement in spontaneous locomotor recovery effective immediately after SCI over the course of 8 weeks in rats implanted with 3D CNF. Since the improved function took effect starting as early at 24 h post-SCI, indicates involvement of our substrate in altering facilitation of tissue response at the early acute phase. Unique mechanical coupling of the implant and the neural tissue of the CNF might be responsible for management of acute SCI outcomes, like for example edema. Intensive research of spinal cord physiology has also revealed the ability of the embedded circuits in the lumbar segments of mammals in producing coordinated patterns of leg motor activity without supraspinal input (Sherrington et al., 1910, Kiehn O et al., 2017, Capogrosso, 2016). To gain more descriptive accounts on impairment, we assessed skilled locomotor behaviour performance on equally spaced rungs of a ladder. An exhaustive assessment of limb placement, stepping and motor control of each paw placement can be illustrated by ladder rung test to reveal deficits which are not apparent during normal locomotion (Metz GA et al., 2002, 2009). Similar to our result obtained from BBB rating, we found greater recovery with an immediate onset based on ladder task performance in rats implanted with our substrate. In addition to management of early phase alterations, this improvement in tasks like placing and stepping, involve boosting of innervation of the hind limb muscles, perhaps due to plasticity or compensation.

In obtaining functional outcomes, area or the size of lesion plays a direct role (data not shown). We measured area of the lesion to address if the behavioural outcomes were a consequence of lesion severity in different groups of animals. Surprisingly, the area of lesion 8 weeks post implantation was significantly lower in the control lesioned animals compared with 3D CNF-implanted animals despite the documented greater deficits in recovery. It could be possible that the lesion area in control group was reduced as a result of collapsing of tissue over the course of implantation; however, this does not happen in the CNF-group despite the presence of implant. Various implants in literature have reported to cause further damage and enlargement of the implantation site, especially in case of spinal implants due to postural reasons. This has been mainly reported due to a mechanical mismatch between tissue and substrate (Minev et al 2013). In contrast to this, our 3D CNF scaffold due to careful mechanical coupling with the surrounding tissue was spared from such consequences; hence, no tissue compression, disintegration or further damage of surrounding tissue was observed. A possible explanation to larger lesion area could be the fact that our surgical model (see Mat and Methods) allowed less control on the size of the lesion due to reduced visibility. Nevertheless, despite increased lesion area, the observed improvement in locomotor activity demonstrates capacity of this scaffold in regaining functional recovery post SCI. Further studies with a more controlled surgical model can be useful to validate our finding. Results obtained from footprint analysis correlated with other behavioural data representing early onset of plantar placement in implanted animals confirm behavioural locomotor improvements ascribed to our scaffold implant.

As an immune-reponse measurement of astrogliosis and microglial reaction in spinal cord injured rats, we assessed GFAP and Iba-1 positive area in regions rostral and caudal to the lesion. 3D CNF demonstrated to be biocompatible when implanted into the spinal cord; the inflammatory responses were similar with a trend towards a reduced reaction in 3D CNF compared to the lesion group. No correlation with the distance neither from the implant nor in the rostral vs. caudal position was observed. We noticed a significantly increasing GFAP reaction from rostral to caudal end of the lesioned animals. This increment of tissue reaction was spared in animals implanted with CNF. As per previous, reports, one way of spontaneous functional recovery mechanism involve sprouting and detouring of existing innervations from spared neurons; mostly located in regions rostral to the injury site (i.e.

undisrupted supra-lesion site). We hypothesize that effect can be due to an improved propriospinal detouring or crossing (around or through) the 3D CNF implant (Filli et al 2014, Pohland et al 2015). We did not investigate any markers or presence of such innervation in our study yet, but it would be interesting to speculate the origin of these observed differences. Similar to our previous results, we detected neurons invading the 3D scaffolds indicating that the environment was permissive for neuronal re-growth. Our results strongly support 3D CNF as biocompatible and a well-integrated substrate within the spinal cord tissue.

Our studies suggest the use of 3D scaffolds of pure or incorporated CNT as a potential candidate for the re-growth of neural networks. Our *in vitro* electrophysiology results demonstrate not only improved synaptic performance but also functional reconnection. Functional behaviour assessment of locomotor activity, demonstrate faster and improved recovery in lumbar and cervical hemilesion models (spinal studies so far done on 3D CNF). Immune reaction associated with CNF and PDMS+CNT implants was limited and both implants integrated well with the surrounding tissue of brain and spinal cord. Neuronal processes migrated within the implant indicating neuro-compatibility. We encourage further advancements towards use of 3D CNT based implants in providing platforms for the creation of multidimensional synthetic scaffolds as neural implantable devices.

# References

---

A. Faden, T. Jacobs, J. Holaday, Opiate antagonist improves neurologic recovery after spinal injury, *Science*, 211 (1981), pp. 493-494

A.M. Parr, I. Kulbatski, T. Zahir, X. Wang, C. Yue, A. Keating, C.H. Tator Transplanted adult spinal cord-derived neural stem/progenitor cells promote early functional recovery after rat spinal cord injury, *Neuroscience*, 155 (2008), pp. 760-770

Alessandra Fabbro, Ambra Villari, Jummi Laishram, Denis Scaini, Francesca M.Toma, Antonio Turco, Maurizio Prato and Laura Ballerini (2012) Spinal cord explants use carbon nanotube interfaces to enhance neurite outgrowth and to fortify synaptic inputs *ACS Nano* 6, 2041–2055

Anthony M. Choo, Secondary pathology following contusion, dislocation, and distraction spinal cord injuries *Experimental Neurology*; 212, 2,(2008), 490-506

Basso D.M., Beattie M.S., Bresnahan J.C. A sensitive and reliable locomotor rating scale for open field testing in rats. *J Neurotrauma.* ;12:1–21 (1995)

Benfey M, Aguayo AJ. Extensive elongation of axons from rat brain into peripheral nerve grafts. *Nature.* 1982;296:150–152

Biran R., Noble M. D., Tresco P. A., Directed nerve outgrowth is enhanced by engineered glial substrates. *Exp. Neurol.* 184, 141–152 (2003).

Bomze HM, Bulsara KR, Iskandar BJ, Caroni P, Pate Skene JH. Spinal axon regeneration evoked by replacing two growth cone proteins in adult neurons. *Nat Neurosci.* 2001;4:38–43

Bonilla IE, Tanabe K, Strittmatter SM. Small proline-rich repeat protein 1A is expressed by axotomized neurons and promotes axonal outgrowth. *J Neurosci.* 2002 Feb 15; 22(4):1303-1

Bosi S., Rauti R., Laishram J., Turco A., Lonardoni D., Nieuws T., Prato M., Scaini D., Ballerini L., From 2D to 3D: Novel nanostructured scaffolds to investigate signaling in reconstructed neuronal networks. *Sci. Rep.* 5, 9562 (2015)

Bracci E., Beato M., Nistri A., Afferent inputs modulate the activity of a rhythmic burst generator in the rat disinhibited spinal cord in vitro. *J. Neurophysiol.* 77, 3157.– (1997)

C.P. Hofstetter, N.A.V. Holmstrom, J.A. Lilja, P. Schweinhardt, J. Hao, C. Spenger, Z. Wiesenfeld-Hallin, S.N. Kurpad, J. Frisen, L. Olson Allodynia limits the usefulness of intraspinal neural stem cell grafts; directed differentiation improves outcome, *Nat. Neurosci.*, 8 (2005), pp. 346-353

Camilli L., Pisani C., Gautron E., Scarselli M., Castrucci P., D'Orazio F., Passacantando M., Moscone D., De Crescenzi M., A three-dimensional carbon nanotube network for water treatment. *Nanotechnology* 25, 065071 (2014)

Camilli L., Pisani C., Passacantando M., Grossi V., Scarselli M., Castrucci P., De Crescenzi M., Pressure-dependent electrical conductivity of freestanding three-dimensional carbon nanotube network. *Appl. Phys. Lett.* 102, 183117 (2013).

Capogrosso, M., Milekovic, T., Borton, D., Wagner, F., Moraud, E. M., Mignardot, J.-B., ... Courtine, G. A Brain–Spinal Interface Alleviating Gait Deficits after Spinal Cord Injury in Primates. *Nature*, 539(7628), 284–288 (2016)

Cellot G., Toma F. M., Varley Z. K., Laishram J., Villari A., Quintana M., Cipollone S., Prato M., Ballerini L., Carbon nanotube scaffolds tune synaptic strength in cultured neural circuits: Novel frontiers in nanomaterial–tissue interactions. *J. Neurosci.* 31, 12945–12953 (2011).

D. Bottai, L. Madaschi, A.M. Di Giulio, A. Gorio Viability-dependent promoting action of adult neural precursors in spinal cord injury, *Mol. Med.* (Cambridge, MA), 14 (2008), pp. 634-644

David S, Aguayo AJ. Axonal elongation into peripheral nervous system "bridges" after central nervous system injury in adult rats, *Science*. 1981 Nov 20;214(4523):931-3.

De Volder M. F. L., Tawfick S. H., Baughman R. H., Hart A. J., Carbon nanotubes: Present and future commercial applications. *Science* 339, 535–539 (2013)

Dru AB, Hoh DJ. Activating spinal interneurons for neural repair after spinal cord injury. *World Neurosurg*. 2015

Dvir T, Timko BP, Kohane DS, Langer R. Nanotechnological strategies for engineering complex tissues. *Nature nanotechnology* 6, 1:13-22 (2011)

E. R. Aurand, S. Usmani, M. Medelin, D. Scaini, S. Bosi, F. B. Rosselli, S. Donato, G. Tromba, M. Prato, L. Ballerini, *Adv. Funct. Mater.* (2017), 1700550

F.D. Gregorio, G. Ferrari, P. Marini, R. Siliprandi, A. Gorio, The influence of gangliosides on neurite growth and regeneration, *Neuropediatrics*, 15 (2008), pp. 93-96

Fabbro A., Prato M., Ballerini L., Carbon nanotubes in neuroregeneration and repair. *Adv. Drug Deliv. Rev.* 65, 2034–2044 (2013).

Fabbro A., Villari A., Laishram J., Scaini D., Toma F. M., Turco A., Prato M., Ballerini L., Spinal cord explants use carbon nanotube interfaces to enhance neurite outgrowth and to fortify synaptic inputs. *ACS Nano* 6, 2041–2055 (2012).

Faith H Brennan, Aileen J Anderson, Stephen M Taylor, Trent M Woodruff and Marc J Ruitenberg, Complement activation in the injured central nervous system: another dual-edged sword? *Journal of Neuroinflammation* 2012, 9 :137

Filli L, Engmann AK, Zörner B, Weinmann O, Moraitis T, Gullo M, Kasper H, Schneider R, Schwab ME. Bridging the gap: a reticulo-propriospinal detour bypassing an incomplete spinal cord injury. *J Neurosci.* 34, 40 (2014)13399-410

Furlan, F., Taccola, G., Grandolfo, M., Guasti, L., Arcangeli, A., Nistri, A. and Ballerini, L., 2007. ERG conductance expression modulates the excitability of ventral horn GABAergic interneurons that control rhythmic oscillations in the developing mouse spinal cord. *Journal of Neuroscience*, 27(4), pp.919-928.

G.W.J. Hawryluk, J. Rowland, B.K. Kwon, M.G. Fehlings, Protection and repair of the injured spinal cord: a review of completed, ongoing, and planned clinical trials for acute spinal cord injury, *Neurosurg. Focus*, 25 (2008), p. E14

Gerardo-Nava J., Hodde D., Katona I., Bozkurt A., Grehl T., Steinbusch H. W. M., Weis J., Brook G. A., Spinal cord organotypic slice cultures for the study of regenerating motor axon interactions with 3D scaffolds. *Biomaterials* 35, 4288–4296 (2014)

Heidemann M., Streit J., Tschertter A., Functional regeneration of intraspinal connections in a new in vitro model. *Neuroscience* 262, 40–52 (2014)

Hu H., Ni Y., Montana V., Haddon R. C., Parpura V., Chemically functionalized carbon nanotubes as substrates for neuronal growth. *Nano Lett.* 4, 507–511 (2004).

Isa T., The Brain Is Needed to Cure Spinal Cord Injury. *Trends Neurosci.* 40 (10), 625-636 (2017)

Khan, F.; Tanaka, M.; Ahmad, S.R. Fabrication of polymeric biomaterials: A strategy for tissue engineering and medical devices. *J. Mater. Chem. B* 2015, 3, 8224–8249

Kiehn O. Decoding the organization of spinal circuits that control locomotion. *Nat Rev Neurosci*, 17:224–238 (2016)

Kotov N. A., Winter J. O., Clements I. P., Jan E., Timko B. P., Campidelli S., Pathak S., Mazzatenta A., Lieber C. M., Prato M., Bellamkonda R. V., Silva G. A., Kam N. W. S., Patolsky F., Ballerini L., Nanomaterials for neural interfaces. *Adv. Mater.* 21, 3970–4004 (2009).

Langer, R., Vacanti, J.P Tissue engineering, 1993, Science Volume 260, Issue 5110, 1993, Pages 920-926

Laube T, Schanze T, Brockmann C, Bolle I, Stieglitz T, Bornfeld N. Chronically implanted epidural electrodes in Göttinger minipigs allow function tests of epiretinal implants., Graefes Arch Clin Exp Ophthalmol. 2003 Dec;241(12):1013-9

Lingling Tian, Molamma P. Prabhakaran, and Seeram Ramakrishna, Strategies for regeneration of components of nervous system: scaffolds, cells and biomolecules. Regen Biomater. 2015 Mar; 2(1): 31–45

López-Dolado, E., González-Mayorga, A., Portolés, M. T., Feito, M. J., Ferrer, M. L., del Monte, F., Gutiérrez, M. C. and Serrano, M. C., Subacute Tissue Response to 3D Graphene Oxide Scaffolds Implanted in the Injured Rat Spinal Cord. Adv. Healthcare Mater., 4: 1861–1868 (2015)

Lovat V., Pantarotto D., Lagostena L., Cacciari B., Grandolfo M., Righi M., Spalluto G., Prato M., Ballerini L., Carbon nanotube substrates boost neuronal electrical signaling. Nano Lett. 5, 1107–1110 (2005).

Martin Pohland and Jana Glumm, M.D., Propriospinal interneurons in the spotlight for anatomical and functional recovery after spinal cord injury, Neural Regen Res. (2015) Nov; 10(11): 1737–1738

Mazzatenta A., Giugliano M., Campidelli S., Gambazzi L., Businaro L., Markram H., Prato M., Ballerini L., Interfacing neurons with carbon nanotubes: Electrical signal transfer and synaptic stimulation in cultured brain circuits. J. Neurosci. 27, 6931–6936 (2007).

Metz GA, Whishaw IQ. Drug-induced rotation intensity in unilateral dopamine-depleted rats is not correlated with end point or qualitative measures of forelimb or hindlimb motor performance. Neuroscience ; 111:325–336 (2002).



Metz, Gerlinde A., and Ian Q. Whishaw. “The Ladder Rung Walking Task: A Scoring System and Its Practical Application.” *Journal of Visualized Experiments* : JoVE 28: 1204. (2009)

Mindan Wang, Peng Zhai, Xiongbiao Chen, David J. Schreyer, Xiaodan Sun, Ph.D., and Fuzhai Cui, Ph.D Bioengineered Scaffolds for Spinal Cord Repair, *Tissue Engineering: Part B* Volume 17, Number 3, 2011

Minev I. R., Musienko P., Hirsch A., Barraud Q., Wenger N., Moraud E. M., Gandar J., Capogrosso M., Milekovic T., Asboth L., Torres R. F., Vachicouras N., Liu Q., Pavlova N., Duis S., Larmagnac A., Vörös J., Micera S., Suo Z., Courtine G., Lacour S. P., *Biomaterials*. Electronic dura mater for long-term multimodal neural interfaces. *Science* 347, 159.– (2015)

Molly S. Shoichet, Ciara C. Tate, M. Douglas Baumann, and Michelle C. LaPlaca. Chapter 8 Strategies for Regeneration and Repair in the Injured Central Nervous System

Raivich G, Bohatschek M, Da Costa C, Iwata O, Galiano M, Hristova M, Nateri AS, Makwana M, Riera-Sans L, Wolfer DP, Lipp HP, Aguzzi A, Wagner EF, Behrens A, The AP-1 transcription factor c-Jun is required for efficient axonal regeneration. *Neuron*. 2004 Jul 8; 43(1):57-67

Richardson PM, McGuinness UM, Aguayo AJ. Axons from CNS neurons regenerate into PNS grafts. *Nature*. 1980;284:264–265

S. Okada, K. Ishii, J. Yamane, A. Iwanami, T. Ikegami, H. Katoh, Y. Iwamoto, M. Nakamura, H. Miyoshi, H.J. Okano, C.H. Contag, Y. Toyama, H. Okano In vivo imaging of engrafted neural stem cells: its application in evaluating the optimal timing of transplantation for spinal cord injury, *FASEB J.*, 19 (2005), pp. 1839-1841

Seiffers R, Allchorne AJ, Woolf CJ., The transcription factor ATF-3 promotes neurite outgrowth. *Mol Cell Neurosci*. 2006 May-Jun; 32(1-2):143-54.

Seymour J. P., Kipke D. R., Neural probe design for reduced tissue encapsulation in CNS. *Biomaterials* 28, 3594–3607 (2007).

Sherrington C. Flexion-reflex of the limb, crossed extension reflex, and reflex stepping and standing. *J Physiol (Lond)*;40:28–121 (1910)

Shirian, S., Ebrahimi-Barough, S., Saberi, H. et al. Comparison of Capability of Human Bone Marrow Mesenchymal Stem Cells and Endometrial Stem Cells to Differentiate into Motor Neurons on Electrospun Poly( $\epsilon$ -caprolactone) Scaffold, *Mol Neurobiol* (2016) 53: 5278

Silva NA, Sousa N, Reis RL, Salgado AJ, From basics to clinical: a comprehensive review on spinal cord injury. *Prog Neurobiol.* (2014) Mar;114:25-57

Stevens M. M., George J. H., Exploring and engineering the cell surface interface. *Science* 310, 1135–1138 (2005)

Streit J., Regular oscillations of synaptic activity in spinal networks in vitro. *J. Neurophysiol.* 70, 871–878 (1993)

T. Hashimoto, N. Fukuda, Effect of thyrotropin-releasing hormone on the neurologic impairment in rats with spinal cord injury: treatment starting 24 h and 7 days after injury, *Eur. J. Pharmacol.*, 203 (1991), pp. 25-32

Tello, JF la influencia del neurotropismo en la regeneracion de los centros nervios, 1911, *Trab. Lab. Invest Biolg*, 9:123-159,

Turner J. N., Shain W., Szarowski D. H., Andersen M., Martins S., Isaacson M., Craighead H., Cerebral astrocyte response to micromachined silicon implants. *Exp. Neurol.* 156, 33–49 (1999)

Tyler W. J., The mechanobiology of brain function. *Nat. Rev. Neurosci.* 13, 867–878 (2012)

Usmani, S., Aurand, E. R., Medelin, M., Fabbro, A., Scaini, D., Laishram, J., ... Ballerini, L. 3D meshes of carbon nanotubes guide functional reconnection of segregated spinal explants. *Science Advances*, 7; 2 (2016)

W. Young, E.S. Flamm, H.B. Demopoulos, J.J. Tomasula, V. DeCrescito, Effect of naloxone on posttraumatic ischemia in experimental spinal contusion, *J. Neurosurg.*, 55 (1981), pp. 209-219

Y. Lu, D. Wang, T. Li, X. Zhao, Y. Cao, H. Yang, Y. Y. Duan, *Biomaterials* (2009), 25, 4143.

Yamane, Y., Shiga, H., Haga, H., Kawabata, K., Abe, K., Ito, E., 2000. Quantitative analyses of topography and elasticity of living and fixed astrocytes. *J. Electron Microsc.* (Tokyo) 49 (3), 463–471.

Zhou K., Motamed S., Thouas G. A., Bernard C. C., Li D., Parkington H. C., Coleman H. A., Finkelstein D. I., Forsythe J. S., Graphene functionalized scaffolds reduce the inflammatory response and supports endogenous neuroblast migration when implanted in the adult brain. *PLOS One* 11, e0151589 (2016)